

# Investigations of Time Dependent Flow Phenomena in a Turbine and a Pump-Turbine of Francis Type: Rotor-Stator Interactions and Precessing Vortex Rope

THÈSE N° 4272 (2009)

PRÉSENTÉE LE 12 FÉVRIER 2009

À LA FACULTÉ SCIENCES ET TECHNIQUES DE L'INGÉNIEUR

Laboratoire de machines hydrauliques

SECTION DE GÉNIE MÉCANIQUE

ÉCOLE POLYTECHNIQUE FÉDÉRALE DE LAUSANNE

POUR L'OBTENTION DU GRADE DE DOCTEUR ÈS SCIENCES

PAR

**Alireza ZOBELRI**

acceptée sur proposition du jury:

Prof. M. Deville, président du jury

Prof. F. Avellan, directeur de thèse

Dr J.-B. Houdeline, rapporteur

Prof. C. Kato, rapporteur

Prof. L. Villard, rapporteur



ÉCOLE POLYTECHNIQUE  
FÉDÉRALE DE LAUSANNE

Lausanne, EPFL

2009





*To my lovely wife, Faezeh*

*To my dear parents, Farid and Mahmoud*



# Remerciements

Je tiens à adresser mes plus sincères remerciements à toutes les personnes qui ont été impliquées de près ou de loin dans ce travail effectué au sein du Laboratoire de Machines Hydrauliques (LMH) à l'EPFL.

Ce travail n'aurait pas été possible sans l'appui scientifique et financier de la CTI, de VOITH-SIEMENS, de ANDRITZ, de ALSTOM et de EDF. Je les remercie pour leur engagement, qui a contribué à la réussite du projet.

Que tous les membres du jury soient remerciés pour leur intérêt, leurs critiques enrichissantes et l'attention qu'ils ont porté à ce travail: Prof. Michael Deville, Dr. Jean-Bernard Houdeline, Prof. Chisachi Kato et Prof. Laurent Villard.

Tous mes remerciements vont au Prof. François Avellan, directeur du LMH, et directeur de thèse qui m'a octroyé sa confiance en me permettant d'effectuer ce travail au sein de son Laboratoire. Son soutien, son implication personnelle ainsi que ses conseils ont été un gage de réussite.

Je remercie du fond du coeur le Prof. Jean-Louis Kueny pour son enthousiasme et ses conseils.

Je remercie infiniment le Dr. Johann Gulich pour ses conseils et son aide lors de ma première année de travail.

Mes remerciements vont à l'ensemble des membres du LMH, pour leur sympathie et leur soutien. Je remercie Isabelle, Shadje, Louis et toute l'équipe des mécaniciens, Philippe et le bureau d'études ainsi que Henri-Pascal et le groupe GEM. Je remercie également les anciens doctorants et assistants pour l'ambiance qu'ils ont su instaurer au sein du laboratoire: Faïçal, Lluís, Alex, Sebastiano, Jorge, Tino, Azzdin, Silvia et tous les oubliés.

Une attention particulière à Sonia et Youcef, qui depuis le premier jour m'ont toujours aidé et soutenu.

Durant ces années, j'ai eu l'occasion de rencontrer des personnes aussi exceptionnelles les unes que les autres, qui m'ont toujours aidé. Je remercie Mohammed et Pierre, Christophe, Olivier et Philippe pour leurs conseils, Cécile, Vlad et Bernd qui ont mis une ambiance sympathique au bureau et pour leur disponibilité, ainsi que Stefan, Nicolas, Sébastien, Francisco, Stiven, Ambrosio et Marco pour leur bonne humeur et pour leur aide et leur soutien.

Une attention particulière à Alexandre Perrig, dont le souvenir reste à jamais gravé dans ma mémoire.

Je tiens à exprimer ma profonde gratitude à ma famille. Je vous serai éternellement reconnaissant; ma mère, Farid pour ses encouragements, ses attentions et son dévouement,

et mon père, Mahmoud, pour m'avoir toujours soutenu et encouragé. Un grand merci à Amir et Atefeh pour leur aide et leur disponibilité, Elnaz et Omid pour leur gentillesse et leur attention, ainsi que pour tout ce qu'ils m'apportent dans la vie.

Enfin, je remercie du fond du coeur ma très chère femme, Faezeh, qui sans son soutien, ses encouragements et sa patience, je n'aurais jamais réussi à aller jusqu'au bout.

Alireza Zobeiri

A handwritten signature in blue ink that reads "A. Zobeiri". The signature is written in a cursive style and is positioned above a horizontal line that extends across the width of the signature.

# Résumé

Ce présent travail traite des phénomènes instationnaires d'écoulement dans les turbines Francis et les pompes-turbines. Ceux-ci peuvent causer de graves dommages aux centrales hydrauliques et, par conséquent, limiter leur plage d'exploitation.

L'objectif principal de cette étude est d'obtenir une meilleure compréhension des phénomènes instationnaires par des simulations numériques d'écoulement et des mesures. En particulier, le phénomène d'interaction rotor-stator (RSI) entre les directrices et les aubes de la roue dans une pompe-turbine, et le phénomène de la torche (PVR), qui apparaît dans l'aspirateur d'une turbine Francis au point de charge partielle, sont modélisés.

La simulation numérique a été réalisée à l'aide du logiciel ANSYS-CFX, qui se base sur la méthode des volumes finis. Pour les deux cas étudiés, l'hypothèse de l'écoulement incompressible est considérée, et les effets hydroacoustiques sont négligés.

Avant d'exploiter les résultats obtenus par simulation numérique, une étude de qualité est effectuée afin de maîtriser l'influence de la résolution du maillage, les effets du pas de temps, les critères de convergence et le modèle de turbulence.

Concernant l'interaction rotor-stator, plusieurs points d'exploitation allant de la charge partielle à la forte charge, sont étudiés. Une analyse est effectuée pour le point à forte charge où apparaissent généralement de fortes fluctuations de pression dues à l'interaction rotor-stator.

Les résultats numériques des fluctuations de pressions statiques générées par l'interaction rotor-stator (RSI) dans la bêche spirale et les canaux de distribution sont validés par les résultats expérimentaux. Les résultats de la simulation de la torche (PVR) sont, quant à eux, validés expérimentalement à la paroi de l'aspirateur uniquement.

La comparaison entre les résultats numériques et expérimentaux pour les fluctuations de pression générées par RSI et PVR sont excellentes en termes d'amplitude et de fréquence, à l'exception de quelques points sur la bêche spirale. Ces résultats confirment qu'à l'exception de vibrations, cavitation ou de condition d'interaction de fluide-structure, l'hypothèse d'incompressibilité est correcte.

De plus, les résultats numériques de l'interaction rotor-stator ont clairement permis d'identifier le mode diamétral du champ de pression.

En outre, un nombre sans dimension est introduit reliant la fréquence de passage des aubes de la roue, le débit et le jeu entre le bord de fuite des directrices et le bord d'attaque de l'aube de la roue. Il a ensuite été mis en évidence dans la thèse que les fluctuations de pression sont directement fonction de ce nombre sans dimension.

## **Mots clef**

Turbine hydraulique, Pompe-Turbine, Interaction rotor-stator, Simulation numérique, Fluctuation de pression.

# Abstract

The present work deals with time dependent phenomena, which develop in turbines and pump turbines of Francis type. These phenomena may cause serious damages to hydropower plant. The overall objective of this study is to bring a better understanding of two kinds of time dependent phenomena such as rotor-stator interaction (RSI) and precessing vortex rope (PVR) by numerical simulations of fluid flows and measurements.

Two case-studies appropriate to the investigated unsteady phenomena are selected. The analysis of RSI is performed on the results of a pump-turbine scaled model. A Francis turbine model is selected to investigate PVR in the draft tube.

For the flow numerical simulations, CFD package, ANSYS-CFX, is used, which is a finite-volume based flow solver. For the both case studies, the fluid is assumed to be incompressible, and hence the effects of the hydro-acoustic waves are neglected. Prior to performing the numerical simulations, the effects of grid resolutions, time increments, configurations of the computational domains and turbulence model are studied, and thereby, the optimum parameter sets for each of the test cases are found.

With respect to rotor-stator interaction, several operating points from part load to full load conditions are investigated. At full load operating point corresponding to a strong rotor-stator interaction, the pressure fluctuations resulting from numerical simulations and measurements are analyzed.

The computed results of static pressure fluctuations are validated with the measurements on the casing wall of the spiral casing, the bottom wall of a stay-vane and guide-vane channels for the RSI case and on the wall of the draft tube cone for the PVR case.

The predicted fluctuations in the static pressure fit well with the measured counterparts in terms of both magnitude and frequency for RSI and PVR cases, except for several points such as on the wall in the spiral casing. These results confirm that with the exception of vibration condition, cavitation or fluid-structure interaction, the incompressible flow hypothesis is valid.

For the RSI simulations, the diametrical mode of the pressure fluctuation is clearly identified by decomposing the results obtained from the numerical simulations. The hydro dynamical reason why two peaks in the pressure fluctuation appear during one passage of the blade pitch is also described.

Moreover, a non-dimensional number based on discharge, the period of runner revolution and the time during which, flow passes through the vaneless gap between the guide vanes and the runner blades is proposed. Accordingly, it is found that the magnitudes of the pressure fluctuations well correlate with the proposed function for the three operating conditions investigated from the part load through the full load conditions.

**Keywords**

Hydraulic turbine, Pump-turbine, Rotor-stator interaction, Precessing vortex rope, Numerical simulation, Pressure fluctuation,



# Contents

<b>INTRODUCTION</b>	<b>3</b>
<b>1 Introduction</b>	<b>3</b>
1.1 Hydropower . . . . .	3
1.2 Francis Turbine . . . . .	4
1.3 Hydro-Storage Pump-Turbine . . . . .	6
1.4 Time Dependent Phenomena in Francis Turbines . . . . .	8
1.5 Rotor-Stator Interaction (RSI) . . . . .	8
1.6 Precessing Vortex Rope (PVR) . . . . .	12
1.7 The Present Work . . . . .	16
1.7.1 Problematic and Objective . . . . .	16
1.7.2 Structure of the Document . . . . .	16
<b>I INVESTIGATION METHODOLOGY</b>	<b>19</b>
<b>2 Experimental Methodology</b>	<b>21</b>
2.1 Experimental Facilities . . . . .	21
2.2 Case Study . . . . .	22
2.3 Wall Pressure Measurement . . . . .	23
<b>3 Computational Methodology</b>	<b>27</b>
3.1 Computational Hypothesis . . . . .	27
3.2 Incompressible Viscous Flow . . . . .	27
3.2.1 Fundamental Equations of Fluid Mechanics . . . . .	28
3.2.2 Navier-Stokes Equations . . . . .	29
3.2.3 Turbulence Modeling . . . . .	29
3.3 The Solver . . . . .	35
3.3.1 Advection Scheme . . . . .	35
3.3.2 Boundary Conditions . . . . .	35
3.3.3 Rotor-Stator Interfaces . . . . .	36
3.4 Computing Resources . . . . .	37
<b>II ROTOR-STATOR INTERACTION</b>	<b>39</b>
<b>4 Numerical Simulation of RSI</b>	<b>41</b>
4.1 Numerical Configurations . . . . .	41

4.1.1	Investigated Operating Points . . . . .	41
4.1.2	Computational Domain . . . . .	42
4.2	Quality Checks . . . . .	43
4.2.1	Purpose of Quality Checks . . . . .	43
4.2.2	Spatial Discretization . . . . .	43
4.2.3	Time Discretization . . . . .	44
4.2.4	Convergence . . . . .	46
4.2.5	Turbulence Models . . . . .	46
4.2.6	Reduced Computational Domains . . . . .	48
4.2.7	Selected Configuration . . . . .	50
4.2.8	Meshing . . . . .	50
4.3	Results Comparison of RSI . . . . .	51
4.3.1	Pressure Fluctuations in the Spiral Casing . . . . .	51
4.3.2	Pressure Fluctuations in the Stator . . . . .	54
4.3.3	Pressure Fluctuations in the Impeller . . . . .	58
<b>5</b>	<b>RSI Physical Analysis</b>	<b>65</b>
5.1	Pressure Propagation in the Stationary Domain . . . . .	65
5.1.1	Angular Pressure Advection . . . . .	65
5.1.2	Radial Advection of Pressure . . . . .	76
5.2	Pressure Fluctuations in the Impeller . . . . .	81
5.3	Resulting Modes of RSI . . . . .	90
5.4	Influence of operating points on RSI . . . . .	94
<b>III</b>	<b>PRECESSING VORTEX ROPE</b>	<b>101</b>
<b>6</b>	<b>Numerical Simulation of Vortex Rope</b>	<b>103</b>
6.1	Numerical Configuration . . . . .	103
6.1.1	Investigated Operating Point . . . . .	103
6.1.2	Computational Domain . . . . .	104
6.2	Quality Checks . . . . .	104
6.2.1	Purpose of the Quality Checks . . . . .	104
6.2.2	Spatial Discretization . . . . .	105
6.2.3	Turbulence Models . . . . .	106
6.2.4	Time Discretization . . . . .	107
6.2.5	Boundary Conditions . . . . .	108
6.3	Pressure Fluctuations in the Draft Tube . . . . .	111
<b>IV</b>	<b>CONCLUSIONS</b>	<b>117</b>
<b>7</b>	<b>Conclusions and Perspectives</b>	<b>119</b>
7.1	Conclusions . . . . .	119
7.2	Perspectives . . . . .	120

---

<b>Appendix</b>	<b>125</b>
<b>A Signal Processing</b>	<b>125</b>
A.1 Pressure Fluctuations . . . . .	125
A.1.1 Average Pressure . . . . .	126
A.1.2 Phase Average (Pressure Fluctuation) . . . . .	126
A.2 Spectral Analysis . . . . .	126
A.2.1 Fourier Series . . . . .	126
A.2.2 Fourier Transform . . . . .	127
A.2.3 2D Fourier Transform . . . . .	128



# Notations

## Latin Characters

$a$	Wave speed	[m/s]
$a_s$	Speed of sound	[m/s]
$f$	Frequency $f = 1/T$	[Hz]
$f_n$	Frequency of runner revolution	[Hz]
$g$	Terrestrial Acceleration $g \simeq 9.81$ [m/s <sup>2</sup> ]	[m/s <sup>2</sup> ]
$k$	Diametrical Mode, Integer number	[-]
$l$	Length	[m]
$m$	Harmonic order, Integer number	[-]
$n$	Harmonic order, Integer number	[-]
$p$	Unsteady static pressure: $p = \bar{p} + \tilde{p}$	[Pa]
$\bar{p}$	Mean static pressure	[Pa]
$\tilde{p}$	Pressure fluctuation	[Pa]
$p_r$	Pressure in the rotating domain	[Pa]
$p_{rot}$	Rotating component of vortex rope induced pressure fluctuation	[Pa]
$p_s$	Pressure in the stationary domain	[Pa]
$p_{syn}$	Synchronous component of vortex rope induced pressure fluctuation	[Pa]
$p_{inlet}$	Static pressure at the spiral casing inlet	[Pa]
$p_v$	Water vapor pressure	[Pa]
$\tilde{p}_{inlet}$	Pressure fluctuation at spiral casing inlet	[Pa]
$r$	Radius	[m]
$r_{gap}$	Vaneless gap	[m]
$r_1$	Radius at impeller inlet	[m]
$t$	Time	[s]
$z_b$	Impeller blade number	[-]
$z_o$	Guide vane number	[-]
$A$	Cross section area	[m <sup>2</sup> ]
$C$	Absolute flow velocity	[m/s]
$C_m$	Meridional component of the flow velocity	[m/s]

$C_u$	peripheral component of the flow velocity	[m/s]
$E$	Massic hydraulic energy: $E = gH = \frac{p}{\rho} + gz + \frac{C^2}{2}$	[J/kg]
$N$	Rotational speed	[rpm]
$P$	Power	[W]
$Q$	Flow discharge	[m <sup>3</sup> /s]
$T_n$	Period of runner revolution	[s]
$T$	Torque	[Nm]
$U$	Runner/impeller peripheral velocity: $U = \omega R$	[m/s]
$W$	Relative flow velocity	[m/s]

### Greek Symbols

$\theta$	Angle	[rad]
$\theta_s$	Angular position in stationary system	[rad]
$\theta_r$	Angle position in rotating system	[rad]
$\rho$	Density	[kg /m <sup>3</sup> ]
$\omega$	Angular velocity: $\omega = 2\pi f$	[rad/s]
$\omega_b$	Angular velocity in the rotating frame: $\omega_b = z_o\omega$	[rad/s]
$\Delta\varphi$	Phase shift	[rad]
$\Delta\varphi_b$	Phase shift in the rotating frame: $\Delta\varphi_b = z_o\Delta\varphi$	[rad]
$\tau$	Shear stress	[Pa]
$\lambda$	Friction coefficient	[-]

### Non-dimensional Values

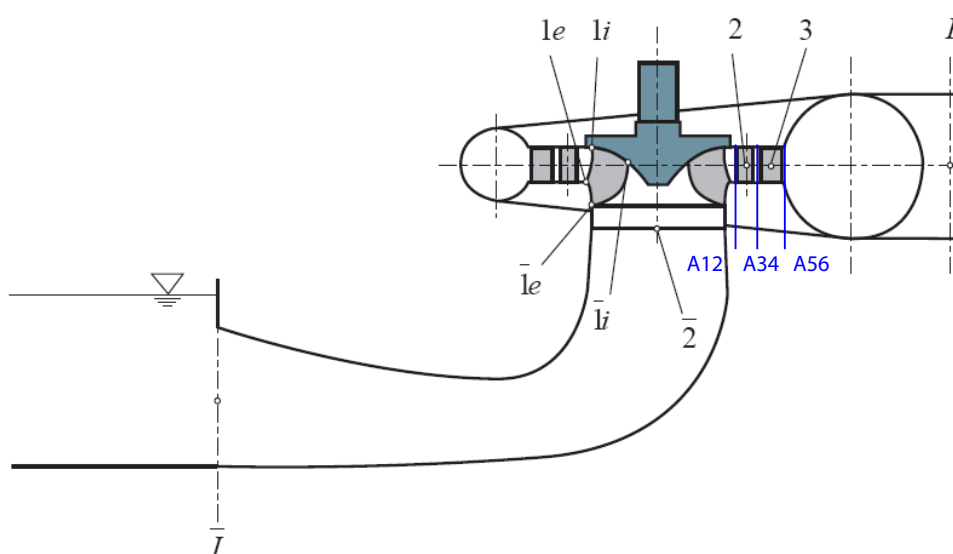
$\tilde{C}p$	Pressure coefficient: $\tilde{C}p = \tilde{p}/\frac{1}{2}\rho U_1^2$	[-]
$Cp$	Pressure coefficient: $Cp = (\tilde{p} - \tilde{p}_{inlet})/\frac{1}{2}\rho U_1^2$	[-]
$Cp_{min}$	Pressure coefficient: $Cp_{min} = (p - p_{min})/\frac{1}{2}\rho U_1^2$	[-]
$M$	Mach number: $M = C/a_s$	[-]
$Re$	Reynolds number	[-]
$\eta$	Efficiency: $\eta = T\omega/(\rho Q E)$	[-]
$\eta_{Max}$	Maximum Efficiency	[-]
$\nu$	Specific speed $\nu = \varphi^{1/2}/\psi^{3/4}$	[-]
$\sigma$	Cavitation number: $\sigma = (p_\infty - p_v)/\frac{1}{2}\rho C_\infty^2$	[-]
$\varphi$	Flow coefficient: $\varphi = Q/(\pi\omega r^3)$	[-]
$\psi$	Energy coefficient $\psi = 2E/(\omega^2 r^2)$	[-]
$\zeta$	Rotor-Stator coefficient: $\zeta = T_n/t_m = C_m/\omega r_{gap}$	[-]

## Abbreviation

BEP	Best efficiency point
EXP	Experimental result
CFD	Numerical result
OP	Operating point
RSI	Rotor-Stator Interaction
PVR	Precessing Vortex Rope

## Turbine Sections

$I$	Reference section high pressure side, spiral casing inlet
3	Stay vane
2	Guide vane
1	Runner inlet, high pressure side
$i$	Shroud, runner interior streamline
$e$	Hub, runner exterior streamline
$\bar{1}$	Runner outlet, low pressure side
$\bar{2}$	Draft tube inlet
$\bar{1}$	Reference section low pressure side, draft tube outlet
A12	Interface between runner and guide vane
A34	Interface between guide vane and stay vane
A56	Interface between spiral casing and stay vane







# INTRODUCTION



# Chapter 1

## Introduction

### 1.1 Hydropower

Hydropower plants are the key components for the development of new renewable  $CO_2$ -free primary energies and the security enhancement of the country wide electricity supply. Several options of renewable primary energies exist with different size and prospective market shares. However, as far as electricity is concerned, hydropower is the most important renewable contribution to the primary energy supply mix. It represents more than 92% of all worldwide renewable energy generated, and it continues to stand as the most important renewable energy source [51].



Figure 1.1: Francis hydropower plant Karun III, 2'000MW, South of Iran

The world's total technical feasible hydro potential is estimated at 3'870 GW. However, about 56% of it is economically feasible for development [9]. About 760 GW of the mentioned hydropower is already in operation, with a further of 126 GW under construction in 103 countries. At present hydropower supplies about 20% of the world's electricity. It provides more than 50% of national electricity in about 60 countries and about 90% in 25 countries. A number of countries, such as China, India, Iran and Turkey are undertaking large-scale hydro development programmes. There are also several projects

under construction in about 80 countries [9]. Table 1.1 indicates the remaining potential hydropower in the world.

Table 1.1: The potential hydropower sources in the world [51]

Content	Technical potential	Economical potential
Africa	1'750 TWh/year	1'000 TWh/year
Asia	6'800 TWh/year	3'600 TWh/year
North+Central America	1'660 TWh/year	1'000 TWh/year
South America	2'665 TWh/year	1'600 TWh/year

## 1.2 Francis Turbine

In 1848 James Francis developed the concept of a high performance radial hydro turbine with high efficiency. Later, this turbine was called Francis turbine. A Francis turbine is composed of five main components. Spiral casing, stay vanes, guide vanes, runner and draft tube, see Figure 1.2. The stored water behind a dam reaches the spiral casing through the penstocks, see Figure 1.3. The spiral shape of the casing permits to convert the axial flow to radial flow and have balanced flow distribution in the stay vane channels. The guide vanes distribute and control the incoming flow angular momentum to the runner. This distributor mechanism consists of a large number of guide vanes around the circumference, which are simultaneously adjustable. The opening angle of the guide vanes controls the flow rate and runner rotational velocity. The runner is made up of several fixed curved blades. The oriented flow spins the runner, which is connected to the generator by the shaft axis, see Figure 1.4. The last component, draft tube, provides for recovering a part of the kinetic energy and piezometric head between runner outlet and the free surface.

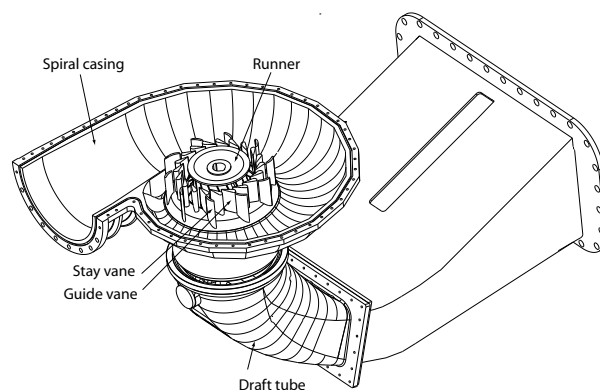


Figure 1.2: Francis turbine

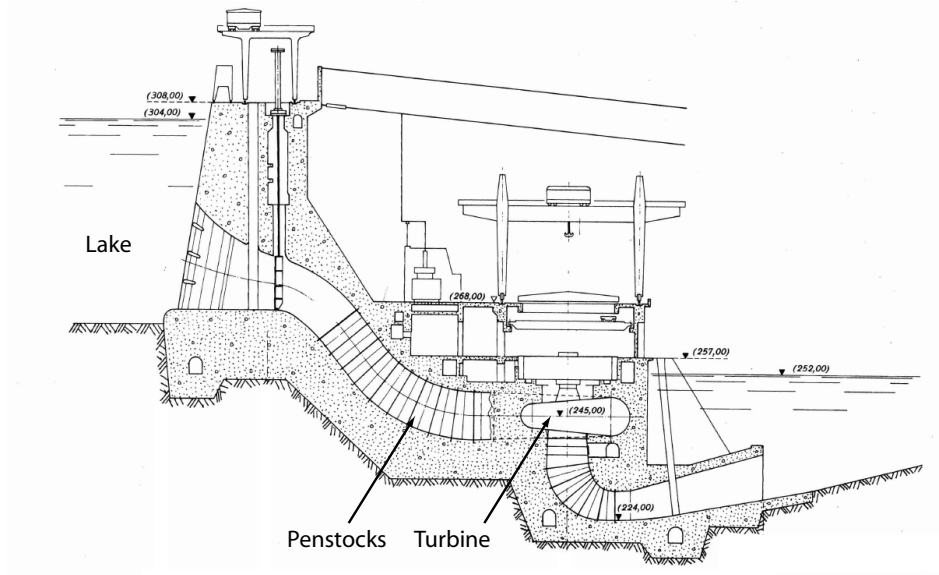


Figure 1.3: Vertical cross section of a hydropower plant [46]

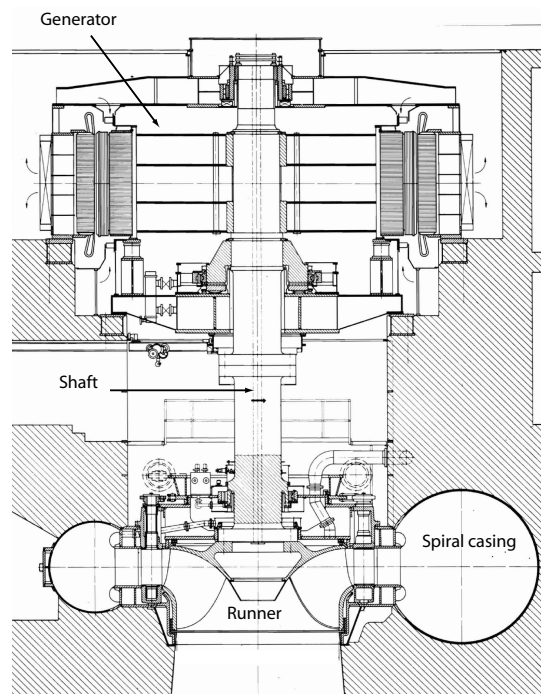


Figure 1.4: Vertical cross section of a Francis turbine and generator with specific speed  $\nu = 0.3$ , blades number  $z_b = 13$  and guide vanes number  $z_o = 24$  [46]

Figure 1.5 illustrates the application domains of different type of hydraulic turbines as a function of the nominal net head  $H_n$  and the nominal discharge  $Q$  of the machine. As it is shown the Francis turbines and pump-turbines cover a wide range of operating conditions. It arises that currently 56% of the turbines in operation are of this type of turbine with an additional 5% of pump-turbines [75].

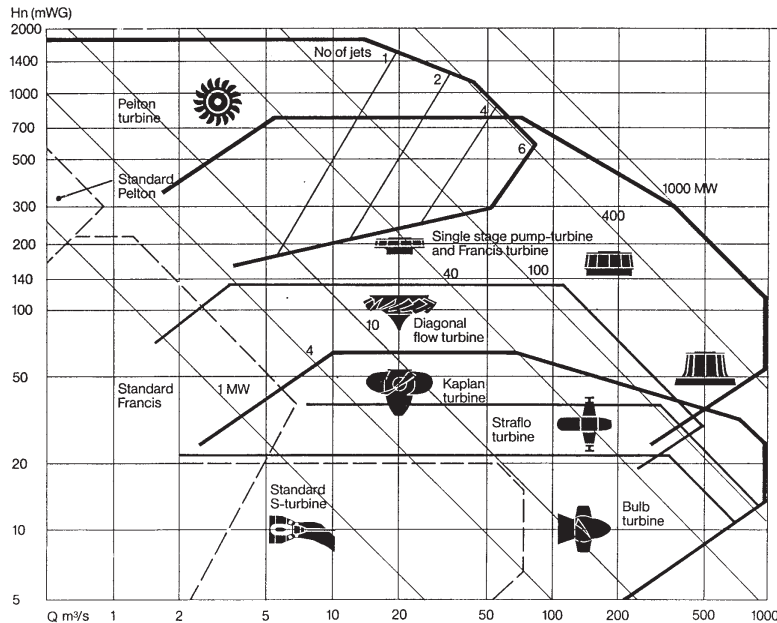


Figure 1.5: Turbine application range [35]

### 1.3 Hydro-Storage Pump-Turbine

A storage pump-turbine power plant is built over two upper and lower reservoirs. During peak hours, usually daytime, the pump-turbine works in the generating mode and converts the hydraulic energy of upper reservoir to electricity, while during the night-time or weekend off-hours, it takes advantage of low electricity price to pumps the water from the lower reservoir to the upper one. The pumped storage units normally use reversible-pump turbines that can be run in both pumping and generating modes. Actually, within an open electrical market, pumped storage stations enable the electrical utilities to trade when power demand is high and to store excess electrical generation from either nuclear or coal power plants or from new renewable energy sources. Therefore, it is not surprising that many projects involving either modernization or development of pumped-storage power plants are planned in many areas in the world. Within the context of modernization existing pumped storage plants, it is important to assess the life span potential of the powerplant by changing from a seasonal to a daily mode of operation to take full benefit of the high demand of peak energy. For the last decade, new important pumped storage plants have been commissioned to face the needs of large storage capacity particularly in Japan, see Table 1.2.

Table 1.2: The new important storage pump-turbine plants in the world

Project	Capacity MW	Units	Unit Power MW	Country	Year
Kannagawa	2'820	6	470	Japan	2005
Goldisthal	1'060	4	265	Germany	2002
Kazunogawa	1'648	4	412	Japan	2001
Tianhuangping	1'800			China	2001
Guangzhou	2'400	8	300	China	2000
Matanoagawa	1'200			Japan	1999
PAVEC Chaira	864	4	216	Bulgaria	1998
Okutataragi	1'932	6	322	Japan	1998

In Switzerland alone, at least four major pumped storage power plant projects are considered for the close future, see Table 1.3, which considering the size of Switzerland, shows clearly that the suggested research project is really brought by market needs.

Table 1.3: The new important storage pump-turbine in Switzerland

Project	Capacity MW	Units	Unit Power MW	Owner	Year
Grimsel 3	350	2	175	KWO	2013
Linthal-Limmern	1'000	4	250	NOK	2015
Nant de Drance	600	4	150	SBB/CFF	2015
FMHL Plus	240	2	120	FMHL	2014

Improving the availability and reliability of the hydro turbines is a challenge from a scientific and a technical point of view, which strongly depends on the gathered knowledge of how the complex phenomena in fluid hydrodynamic behavior develop during off design conditions.

## 1.4 Time Dependent Phenomena in Francis Turbines

Time dependent phenomena in a Francis turbine could be at the origin of vibrations, pressure fluctuations, and even failure of the machine. These unsteady sources have external and internal roots. The external sources could be due to the misalignment of rotating shaft or generator poles (mechanic or electromagnetic source) or flow rate variation (hydraulic source). The internal sources are classified as either periodic or transient phenomena. The concept of periodic phenomena associated with the flow perturbation with a constant frequency due to either flow instability such as, Von-Karman Vortices or Precessing Vortex Rope or blade passage, Rotor-Stator Interaction. Cavitation and flow separation could have a periodic or transient behavior, depending to the operating conditions. Transient phenomenon might be introduced as a flow perturbation with varying frequency and pressure amplitude. Figure 1.6 represents the classification of the time dependent phenomena in a Francis turbine.

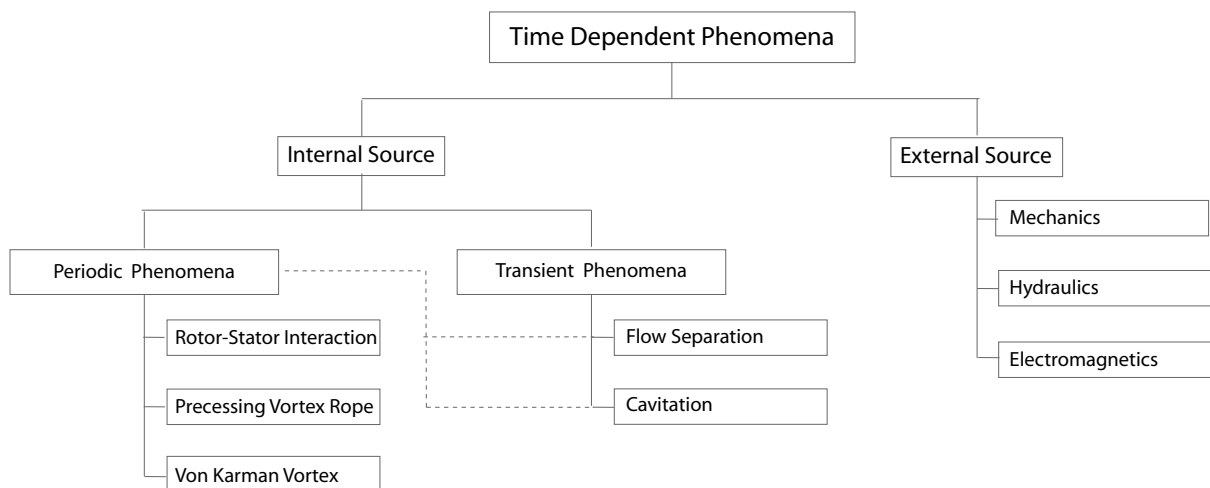


Figure 1.6: Classification of time dependent phenomena in a Francis turbine

## 1.5 Rotor-Stator Interaction (RSI)

For any operating conditions, relative motion between the impeller blades and the guide vanes generates pressure fluctuations that propagate through the entire machine, see Figure 1.7. For the weak interactions, time averaged characteristics of machine are not modified and it works in quasi static operating conditions. However, for strong interactions, vibrations, hydraulic noises and even blade cracks [39] [62] [96] can be introduced. In such a case, the potential vibration frequency is determined by the rate of the blades passing in front of the guide vanes, which is called blade passing frequency, BPF. The BPF and its harmonics are detectable in the stator as well as guide vane passing frequency and related harmonic modes in the impeller. If the frequency of the vibration excites the natural frequency of structure, resonance occurs and might produce the blade cracks, see Figure 1.8. It should be mentioned that the natural frequency of the impeller installed in



water decreases to less than 50% of that in air due to the added mass effect of the flow [96].

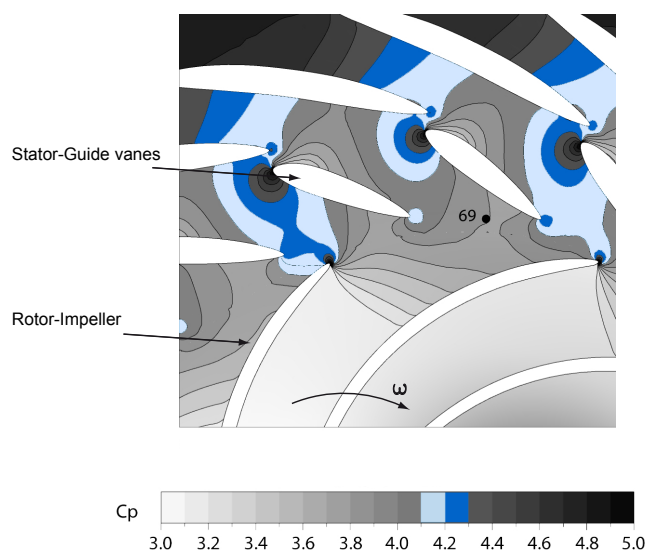


Figure 1.7: Pressure field on the mid plane of a pump-turbine due to the rotor-stator interaction

The RSI phenomenon can be characterized by the effects of the compressibility and incompressibility of water flow. The compressibility effect outstands in the case of resonance and vibration. With respect to the incompressible flow characteristics, flow in the distributor channels is perturbed periodically by the rotating impeller blades. On the other side, the non-uniform flow coming from the guide vane channels generates pressure fluctuations in the rotating domain. The potential effect [11] [37], flow separation [85], wake [59] and blade loading play important roles to increase the pressure fluctuations. In the

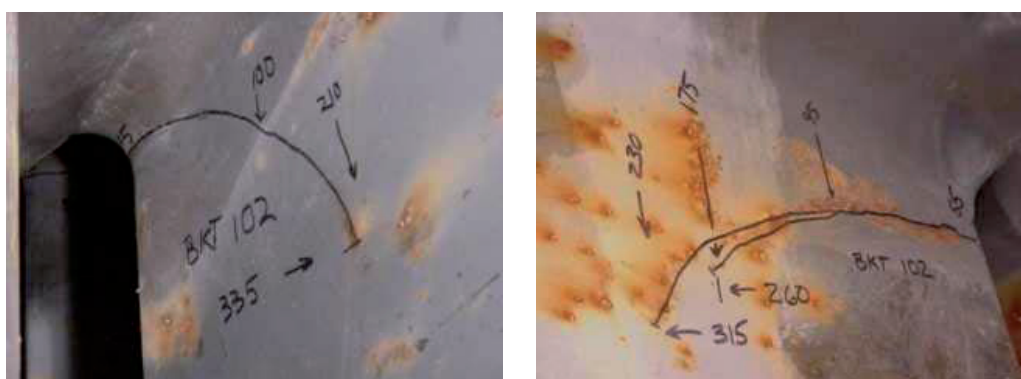


Figure 1.8: Runner blade cracks in a Francis turbine [33]

development of hydroturbines, it is crucial to limit the negative effects of RSI. In the face of this problem, the key issue is to understand the mechanism of the RSI and identify the effective parameters that may increase the pressure fluctuations.

## RSI Literature Review

### Experimental and Analytical Studies

Few experimental investigations of unsteady flow in Francis turbines are presented in the literature and RSI is the issue that covers an important part of these attempts. The results of velocity and pressure measurements are helpful to clarify the mechanism and effects of the mentioned phenomenon. The Velocimetry techniques have been widely applied to turbomachinery domain with the aim of unsteady flow description [26] [17]. Pederson et al. [80] visualized the unsteady flow pattern by PIV and LDV measurements inside the impeller of a centrifugal pump. They focused on the instability problem at off-design operating condition. Shina et al. [91], who took advantage of PIV measurements to analyze the effects of the blades orientations, wakes and the level of the turbulence energy in a centrifugal pump with diffuser vanes.

Investigation of the unsteady pressure measurements and fluid force induced by RSI has been a key research topic for a long time [20] [56] [48] [50]. One of the key operating parameters for potential interaction is the gap between guide vanes and impeller blades, which influences the intensity of the rotor-stator interaction. Dring [30] investigated the RSI in an axial machine and studied the influence of the potential effects and wake for a small vaneless gap. Later, Arndt et al. [5] measured unsteady pressure fluctuations and forces in a centrifugal pump. They investigated the influence of radial gap between rotor and on the pressure fluctuation amplitude. They found out, by increasing the radial gap for 1.5 to 4.5 percent of the impeller discharge radius, that the amplitude of pressure fluctuations decreases by 50%. Guo et al. [40] performed pressure measurements in the volute and impeller. They investigated the analysis of the traveling directions of the rotating pressure waves and the most predominant frequency of both pressure and force fluctuations. They also noted that large alternating fluid forces are not necessarily associated with large pressure fluctuations.

Kubota [57] and Tanaka [96], by taking advantage of experimental results, have developed a theoretical model to determine the diametrical vibration modes in the machine. This model is based on the excitation of the hydroacoustic sources, which are considered all around of the stationary part instead of the guide vanes to model non-uniform pressure fields. These sources are excited periodically by the rotating blades and in any triggered forward and backward hydroacoustic waves are propagated in the domain. The superposition of all these waves by considering the phase shift, determine the dominant frequencies and diametrical modes in the stationary part. Kubota applied this model to explain the effect of the number of the guide vanes and rotating blades on the vibration and determine the diametrical mode in the stationary part. Tanaka applied this model to analyze vibration in a pump-turbine. Bolleter [13] expects the pattern of rotor-stator interactions by following another approach. He considered that the pressure fluctuations due to the RSI are the resulting of the interaction between two non-uniform velocity-pressure fields: One coming from the guide vanes and the other is the non-uniform pressure field at the runner inlet. Franke et al. [36] made a further development of the previous RSI models.

### Numerical Studies

In parallel to experimental investigations, considerable efforts have been made to develop rotor-stator simulation methods. The simplest model is a 1D numerical simulation based on the continuity and momentum equations. This method was applied by Doeffler [25]. Based on it, the turbomachine is modeled by a network of 1D tube. Each individual stator channel is represented by an inertial element. The above mentioned model developed further by Haban et al. [42]. Nicolet et al. [76] coupled the hydroacoustic and momentum equations. These models are applied to simulate RSI in a pump-turbine.

With respect to the more complicated rotor-stator models, Adamczyk [1] [3] [2] developed a procedure to take into account the presence of the neighboring blades by grouping the unsteady terms. This model is based on the time-averaged equations. Following this work, many efforts have been made to develop time-dependent models and compute the unsteady flow induced by RSI [31] [84] [38]. The initial models focused on finding a solution for unsteady simulation including one blade to blade passage. In such a case, different methods based on the phase shift periodicity assumption are developed [44]. Flow simulation of a single blade to blade flow passages could be correct if discharge and flow pattern in different flow passages are fully consistent, which does not the case in reality. To avoid this error, time dependent methods are used to multiple flow passages. The results of recent mentioned simulations have provided very useful research tools. Later, He et. al. [45] have developed unsteady time dependent methods to simulate the unsteady viscous flow through the rotating blades. The simulation of the incompressible 3D unsteady flow of a vaneless centrifugal pump is performed by Gonzalez et al. [39] using a commercial CFD tool. They showed the capability of CFD to predict the unsteady convective field related to the RSI at the blade passing frequency. In order to study the effect of circuit on the pressure fluctuations in pump Longatte and Kueny [60] have carried out a numerical computation. Nowadays, the available computing resources enable to resolve full 3D URANS incompressible equations with transient rotor-stator model. Recently, several numerical researches are investigated by the help of CFD packages to develop a numerical procedure or to explain unsteady physical phenomena [67] [74] [73] [93] [101] [14].

## 1.6 Precessing Vortex Rope (PVR)

Precessing vortex rope is the result of a swirling flow instability in the draft tube at a given part load operating points. It could be at the origin of the pressure oscillation in the draft tube or even vibration in the whole installation [12]. The pressure fluctuation due to PVR becomes more dangerous, if the corresponding frequency approaches the natural frequency of the structure[55]. Figure 1.9 represents a precessing vortex rope, resulting from numerical simulation.

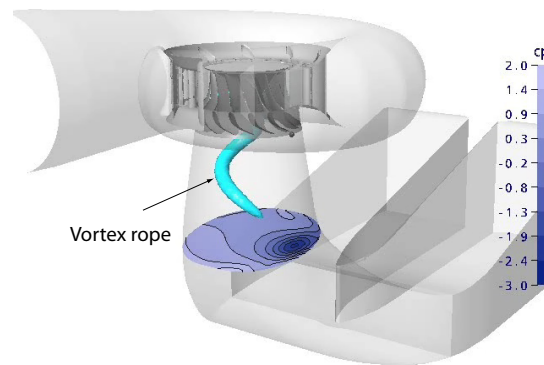


Figure 1.9: Precessing vortex rope resulting from numerical simulation

Under part load operating points, two conditions caused flow instability in the cone of a draft tube. At first, a high ratio of angular to axial momentum that produces a strong swirling flow. As the second condition, an adverse pressure gradient in the axial direction is necessary (second condition). This adverse pressure gradient is highly correlated with the velocity profile at the runner outlet and divergent shape of the cone. Figure 1.10 represents the averaged axial component of flow velocity at the inlet section of the cone. As it is shown, the axial flow at the center is very weak, which increases with a sharp slope from center to outside. Figure 1.11 represents the average of circumferential component of flow velocity, resulting from measurement at the cone inlet.

The physical mechanisms for vortex rope rely on the production of negative axial flow at the cone center that generates the flow stalling zone. This axial reverse flow is called "Vortex Breakdown". The term of vortex breakdown refers to the flow perturbation by forming a recirculation zone at the swirl axis [61]. Figure 1.12 illustrates schematically the mechanism of creation of bubble-like vortex breakdown. The circular vortex breakdown in a geometry, which is composed by a cone and straight tube is represented in Figure 1.13. This bubble-like vortex breakdown deforms to a rolling-up shape of a vortex sheet due to secondary flow in the bend of the draft tube, non-uniform flow coming from the runner outlet [16] [77]. This rolling-up shape is called precessing vortex rope.

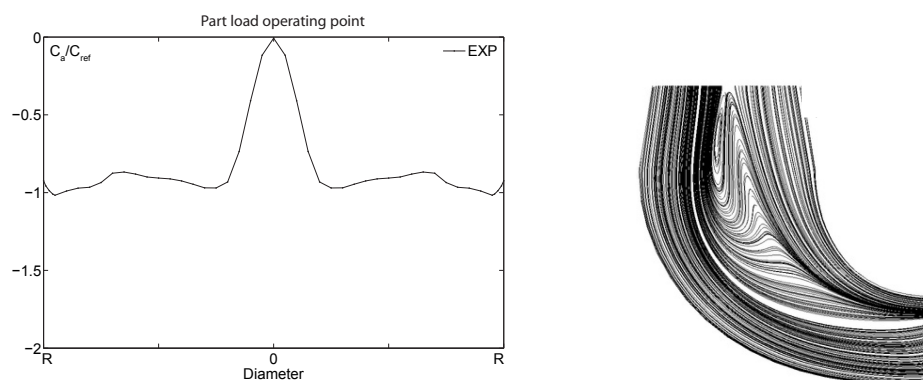


Figure 1.10: Left) Measurements: averaged axial velocity profile at the runner outlet for part load right) Numerical simulation: Corresponding streamlines at the symmetry mid-plane [63]

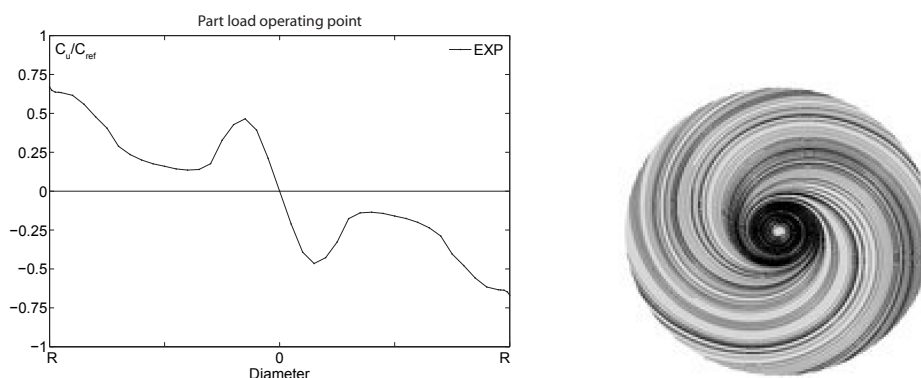


Figure 1.11: Left) Measurements: averaged circumferential velocity profile at the runner outlet for part load (right) Numerical simulation: Corresponding streamlines at the cone inlet [63]

## Part Load Vortex Rope Literature Review

### Experimental and Analytical Studies

Vortex rope and vortex breakdown in swirling flows have been the issue of many investigations since they were recognized. Several researchers as far back as the middle years of the 20<sup>th</sup> century investigated on understanding, modeling and simulating of this issue. Analysis of the swirling flow began with the identification of the flow patterns in a cylindrical tube. A large number of experimental investigations were undertaken. Squares [92] introduced the vortex breakdown theory. Accordingly, the vortex breakdown depends on the maximum angle between axial and circumferential velocity components, which is called swirl angle. Benjamin [10] predicted the occurrence of the vortex breakdown. Such a phenomenon was soon confirmed experimentally by Harvey [43]. As he reported, by increasing the inlet swirl intensity, the vortex breakdown appears as a matter that at the downstream of it, a helical vortex precedes. Cassidy et al. [18] has defined a dimensionless

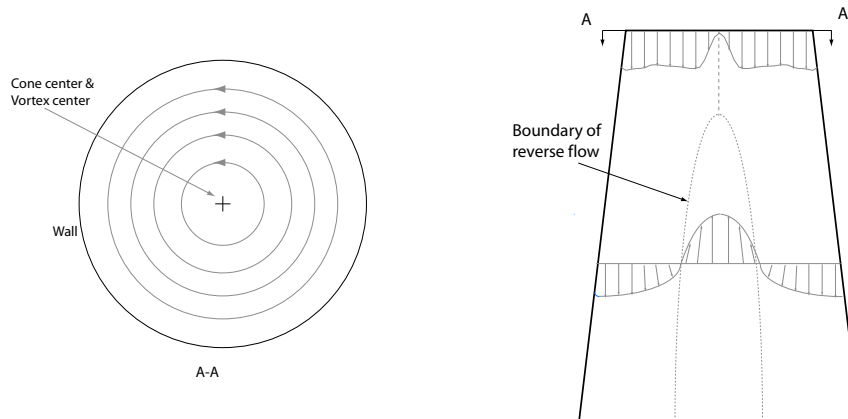


Figure 1.12: Sketch of flow in a conical geometry: left) swirling flow pattern at the cone inlet, right) reverse flow due to vortex breakdown at the cone center

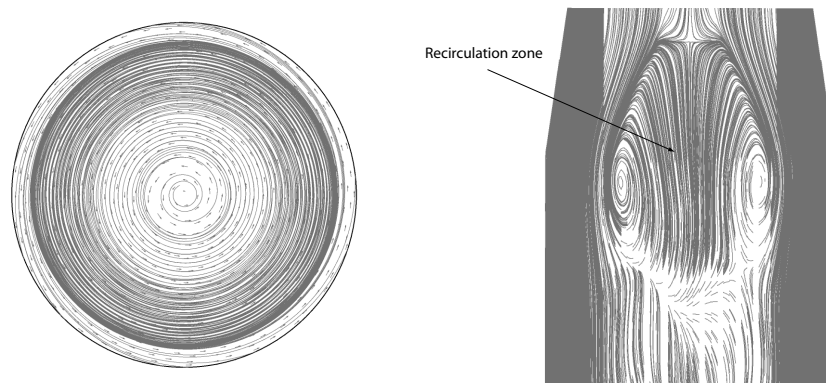


Figure 1.13: Numerical simulation: Stream lines at a horizontal and vertical section represents the circular vortex breakdown.

form of axial and swirling momentum, which is called swirl rate. As they reported the last mentioned parameter can be correlated with frequency of the helical vortex. Later, the previous knowledge has been applied in the elbow draft tube of a Francis turbine [53] [52] [27] [29].

The practical importance of vortex rope in a Francis turbine and its potential harmful effects leads to the FLINDT research project [8]. The main objective of this project was flow investigation in the elbow draft tube of a Francis turbine. Accordingly an extensive experimental data base was built up. In this frame work, Arpe et al. [7], analyzed the steady and unsteady pressure fields at the wall of the draft tube through pressure measurements. The visibility of the vortex rope depends on the pressure level in the cone. Where the minimum pressure level is higher than vapor pressure,  $p_v$ , the helical vortex rope is made of single-phase and invisible, however for lower values, cavitation appears and thus the spiral vortex core is visible. Subsequently, depending on the cavitation number,  $\sigma$ ,

the frequency and pressure amplitude of the vortex revolution are modified. As  $\sigma$  increases the frequency increases, however the pressure amplitude decreases. The variation of the pulsation amplitude with the cavitation number might be dangerous, where the frequency of the vortex rope approaches the natural frequency of the installation [6]. Normally, the frequency of the vortex rope revolution is about 20% to 40% of the runner frequency [86]. The low frequency of pressure fluctuations measured due to part load vortex rope at the draft tube wall could be decomposed into two components: a rotating part due to the vortex rope revolution with the constant pressure field at the horizontal section in the cone of draft tube and a synchronous pressure fluctuations that involve whole draft tube [52] [79] [78] [78]. Out of resonance conditions the rotating part is more important than the synchronous component. In both cases, the fundamental frequency of pressure fluctuations is equal to the vortex core frequency. Dörfler [28] showed such decomposition in the draft tube of a Francis turbine. Angelico [4] demonstrated that using three pressure transducers located in a cross section of the draft tube makes it possible to determine both the rotating and the synchronous parts of the pressure fluctuations.

The availability of advanced flow observation system, such as LDV [21] [22] and PIV, gives the opportunity to survey the steady and time dependent flow pattern in the draft tube. Iliescu et al. [49] performed PIV measurements at the part load operating conditions with a part load cavitation rope. They subsided to reconstruct the vapor volume of the vortex rope and correlate it with the corresponding velocity field.

Consider to the importance of the vortex rope prediction, several theoretical works are investigated. Coustou et al. [23] [24] proposed a new model based on analytical expression of the vortex rope diameter and length descended from experimental observations. Koutnik [58] introduced a mathematical model that considers the time dependent change of system parameters, such as cavitation volume. A similar approach of cavitation parameter mapping was applied for the explanation of inducer instabilities by Tsujimoto [100] and of propeller instabilities in cavitation tunnels by Brennen [15]. Resiga et al. [94] pointed out analytically the unstable nature of the flow for low discharge in a conical draft tube. It is shown that the swirling flow at the outlet of the runner can be accurately decomposed in a sum of three distinct vortices.

## Numerical Studies

In parallel to the experimental and analytical works, a considerable number of numerical investigations were developed and compared with experimental results. The progress of the numerical techniques in the prediction of the turbine characteristics for the operating ranges in the vicinity of the best efficiency point (BEP) ensures a good accuracy. One of the new challenges for the numerical simulation is to predict the partial load operating regimes with or without cavitation. In the frame work of FLINDT project Mauri et al. [64] [66] [65], performed the steady numerical simulation to obtain the averaged flow pattern in part load conditions. Later, Vu et al. [97], investigated in the CFD methodology of predicting the part load vortex rope. They performed a transient flow simulation for single phase using a standard  $k - \varepsilon$  turbulence model. Sick et al. [89] [90] performed an Unsteady Reynolds Averaged Navier-Stokes, URANS, simulation, applying Reynolds Stress turbulence model. For this simulation the computational domain includes the runner and the draft tube. Stein et al. [93] also showed the influence of the upstream

components of draft tube to the pressure amplitude and frequency of vortex rope. Wang et al. [98] simulate numerically the vortex rope by applying the Unsteady Reynolds-Averaged Navier-Stokes equations, RANS, with the RNG turbulence model. Ruprecht [88] [87] focused on the influence of the turbulence models on the accuracy of the frequency of vortex rope. Guo et al. [41] calculated the flow pattern in the draft tube of a pump-turbine by using Large Eddy Simulation method (LES). They performed the mentioned computation for both non-cavitating and cavitating flow. They also studied the effect of computational domain of the flow simulation.

## 1.7 The Present Work

### 1.7.1 Problematic and Objective

High pressure fluctuations due to time dependent phenomena could be at the origin of the turbine damages. Rotor-stator interaction (RSI) and precessing vortex rope (PVR) in the generating mode are two kinds of periodic phenomena that play a major role on the vibration, even resonance. The physical mechanisms of RSI and PVR are associated with both viscous flow perturbation (incompressible flow) and hydroacoustic effects (compressible flow).

Development of incompressible computational flow procedures to provide detailed description of rotor-stator interaction and part load vortex rope phenomena is investigated. The goal of developing these CFD procedures is to find out the optimum configuration of numerical simulation in terms of computing resources and correct prediction of RSI and PVR.

The ability of correct prediction and analyzing of pressure perturbation are the key points to bring further knowledge on the time dependent phenomena and extend the availability of Francis turbines at off-design operating conditions.

In the present work the importance of the hydroacoustic effects are investigated by comparing the experimental results, which include both compressible and incompressible flow characteristics with the numerical results that based on the incompressible flow hypothesis.

### 1.7.2 Structure of the Document

The presented document is divided into four parts. In Part I, the methodology and facilities and fundamental equations are explained. Part II deals with simulation and analysis of rotor-stator interaction and at last, Part III, presents the numerical simulation of part load vortex rope and finally, Part IV that conclude the present work.

#### Part I: Investigation Methodology

**Chapter 2** is a description of the experimental validation platform, wall pressure measurements systems and the choice of case studies.



**Chapter 3** is a review of the computational hypothesis, the fundamental equations of 3D Unsteady Navier-Stokes and turbulence modeling. The solver, the boundary conditions and the rotor-stator interface models are also described.

### **Part II: Rotor-Stator Interaction**

**Chapter 4** is focused on the effects of the numerical configuration on the simulation of rotor-stator interaction. The quality checks such as, time and spatial discretization dependency, convergence criteria and turbulence models as well as the influence of computational domain are performed to optimize the RSI numerical simulations. At the end of chapter 4 the numerical results are validated with the measurements

**Chapter 5** deals with the physical analysis of the pressure fluctuations due to RSI in both stationary and rotating components. Pressure propagation in the distributor and the spiral casing is characterized and explained. In continue, the pressure fluctuations in the impeller are analyzed. The influence of the operating points on the RSI helps to define a non dimensional number that involves the parameters, which are correlated with the pressure fluctuations due to RSI, such as vaneless gap and discharge.

### **Part III: Part Load Vortex Rope**

**Chapter 6** is an investigation to simulate numerically the part load vortex rope in a Francis turbine. The results are validated with the measurements in terms of pressure amplitudes and frequency. Moreover, the synchronous and rotating pressure fluctuations in the cone of draft tube are decomposed and analyzed.

### **Part IV: Conclusion**

**Chapter 7** concludes with the summery of the targets in the numerical simulation and analysis of rotor-stator interaction and vortex rope. Finally, the future line of works to be undertaken to widen the obtained experiences and results are suggested.



# Part I

## INVESTIGATION METHODOLOGY



# Chapter 2

## Experimental Methodology

### 2.1 Experimental Facilities

The measurements are carried out on the EPFL experimental facilities. Figure 2.1 illustrates the platform PF3 of laboratory for hydraulic machines of the EPFL.

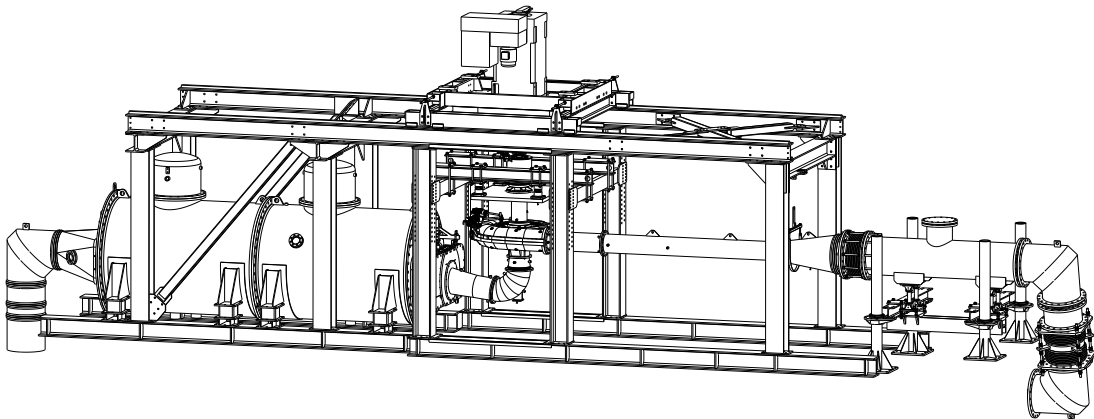


Figure 2.1: View of EPFL experimental facility, *PF3*

This closed-loop facility allows discharges up to  $Q = 1.5m^3/s$  with a maximum specific hydraulic energy of  $E = 600J/kg$ . It is used to carry out experimental research on turbine and pump-turbine model tests up to  $P = 300kW$  power and maximum rotational velocity up to  $2500rpm$ . The measurements of discharge,  $Q$ , specific hydraulic energy,  $E = gH$  and efficiency,  $\eta$ , are performed in compliance with the requirements of the IEC 60193 standards [47]. The EPFL recommends performing the efficiency tests at constant model specific energy,  $E = gH$ , and with the suction tank at atmospheric pressure for the search of the peak efficiency. The method for efficiency value calculation is based on measuring of flow rate, specific energy and main torque,  $\eta = \frac{T\omega}{\rho QE}$ .

## 2.2 Case Study

Two case studies appropriate to the investigated unsteady phenomena are selected. Rotor-stator interaction analysis is performed on the results of the pump-turbine. The model of Francis turbine is also selected to study part load draft tube.

### Pump-Turbine Model

The pump-turbine model is a  $\nu = 0.19$  specific speed pump-turbine, featuring  $z_v = 20$  stay vanes,  $z_o = 20$  guide vanes and  $z_b = 9$  impeller blades, see Figure 2.2. This study is carried out in the frame work of the HYDRODYNA project. In the mentioned case the gap clearance between guide vane trailing edge and impeller leading edge is small, which amplifies the rotor-stator interactions.

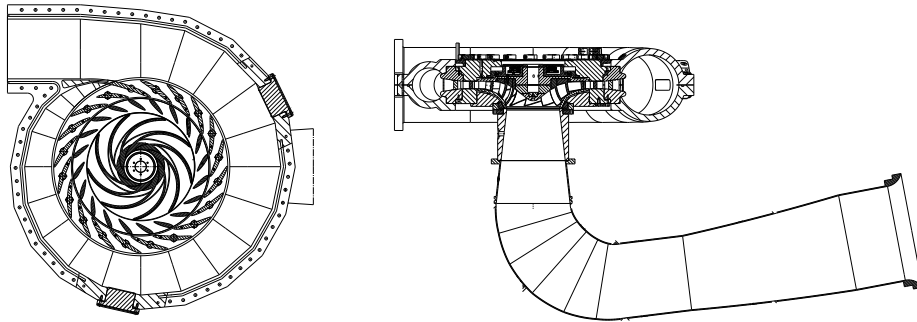


Figure 2.2: Top view (Left) and Vertical cross section (right) of HDYDRODYNA pump-turbine case study,  $\nu = 0.19$  specific speed,  $z_o = 20$  guide vanes and  $z_b = 9$  impeller blades.

### Francis Turbine Model

A high specific speed Francis turbine  $\nu = 0.56$  with 10 stay vanes, 20 guide vanes and 17 runner blades and a single pier draft tube is investigated, see Figure 2.3. This study is accomplished in the scope of the FLINDT project.

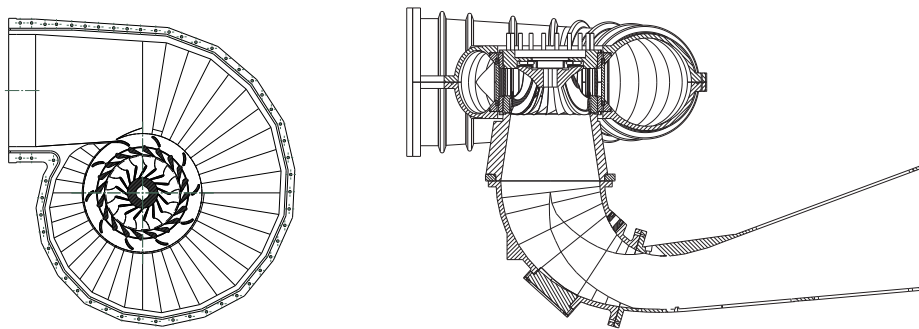


Figure 2.3: Top view (Left) and Vertical cross section (right) of FLINDT Francis turbine case study,  $\nu = 0.56$  specific speed,  $z_o = 20$  guide vanes and  $z_b = 17$  runner blades.

## 2.3 Wall Pressure Measurement

Dynamic pressure measurements are carried out at the walls of both stationary and rotating components. In the pump-turbine case study, 48 dynamic miniature pressure sensors are installed on the upper and lower walls of the guide vanes and stay vane channels.

Figure 2.5 illustrates the measurement system, which is composed by piezoresistive pressure sensors, an amplifier, an acquisition system and a PC.

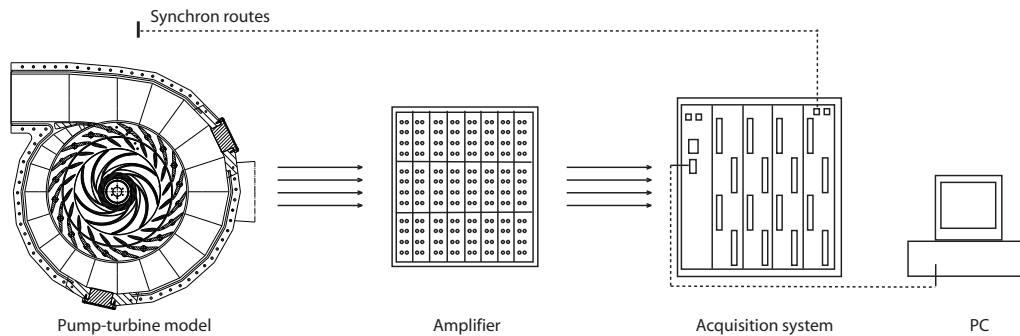


Figure 2.4: Instrumentation chain of wall pressure measurements

To measure unsteady pressure in the impeller, the EPFL developed an instrumented shaft composed of 32 preamplifiers and anti-aliasing filters [32] [83]. The conditioning electronics are connected to 8 acquisition boards located in the turbine shaft with a maximum sampling frequency of  $20kHz$ , see Figure 2.5. Power supply as well as data transmission are made by a 4-channels slip ring installed at the top of the turbine shaft. The transfer rate of digitized data is  $1.5Mbits/sec$ . The synchronization of the data sampling of active boards is performed through a master-slave scheme. First, the slave boards in rotating and static parts of the turbine are armed. The master board, located in the rotating part, is then armed in its turn. Once the master is triggered by the onboard tachometer signal, it outputs a TTL signal to trigger onboard slave modules. This trigger signal is itself simultaneously output from rotating to static part through a wireless photodiodes. Hence, all active modules are synchronously triggered within  $5\mu s$  in time frame [82].

The piezo-resistive sensors are developed for hydro and aerodynamic pressure measurements. The pressure sensitive elements are piezo-resistive chips made of silicon, mounted in a Wheatstone bridge. The active face of the sensor is made of a waterproof membrane of high stiffness. Piezo-resistive gauges are placed on the periphery of the membrane in traction and compression zone. When a pressure is applied on the membrane, the deformation of the latter is transmitted to the gauges, including disequilibrium in the Wheatstone bridge, and thus a variation of the sensor output voltage. A small hole connects the transducer to the fluid passage. The pressure taps, having  $5mm$  diameter and  $15mm$  height, are filled with a plastic compound whose density is similar to water density. This ensures good transmission of the pressure and prevents air from being captured in the transducer chambers. Figure 2.6 illustrates the mentioned pressure sensor.

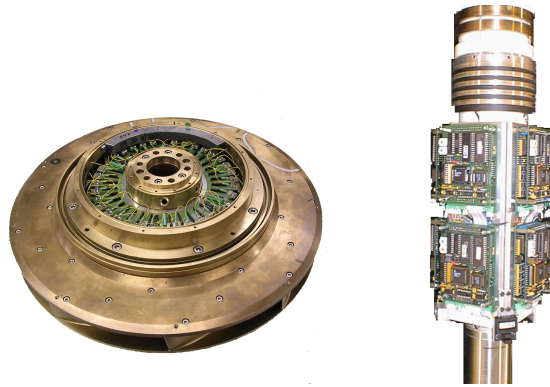


Figure 2.5: Onboard pressure measurement system with outer radius of  $R_1 = 261.75mm$

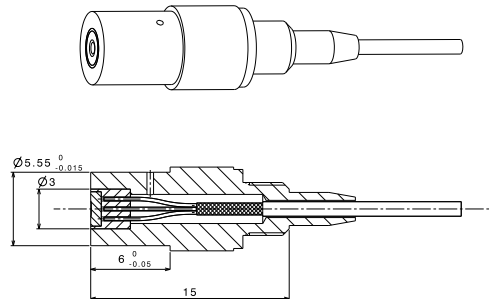


Figure 2.6: Piezo-resistive pressure sensor

## Calibration

Static as well as dynamic calibrations of the pressure sensors are carried out. The static calibration of the pressure transducers performed in a pressurized tank. The voltage outputs are averaged and compared to the readings of a high precision pressure transducer used as a reference. The measurement error is less than 0.5% of the measurement range. To resolve the problem of zero drift, the test rig is systematically shut down every 30 minutes to reset the transducers offsets. Figure 2.7 represents the static calibration for pressure sensors, installed in a guide vane channel and at the impeller. A least square method is used to determine the slope of the regression line, which is in fact the inverse of the sensor instability.

The dynamic calibration of the pressure transducers is carried out in a large vessel with the help of the EPFL bubble spark generator [81]. This generator allows discharging up to  $E = 50J$  electric energy between two immersed electrodes within few microseconds. An explosive growth of a vapor bubble takes place followed by the bubble collapse. Shock waves are thus generated during both the growth and the collapse of the bubble. The resulting pressure pulse excites the pressure transducer in a large frequency band. Arpe described in details, the results of dynamic calibration of the pressure sensors for low and high frequencies [6].



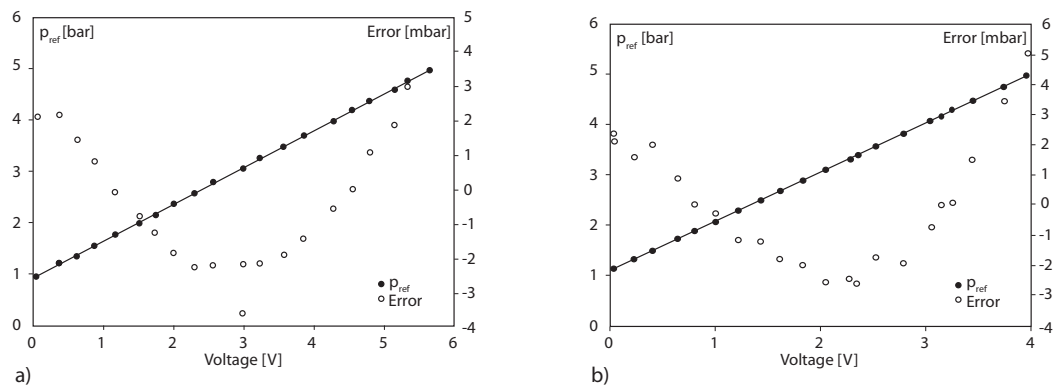


Figure 2.7: Static calibration for a pressure sensor located in a guide vane channel (a) and in the impeller (b)

## Data Reduction

4'200 data samples per impeller rotation during 750 impeller revolutions are measured. The phase averages of pressure fluctuation are compared to the numerical simulations.



# Chapter 3

## Computational Methodology

### 3.1 Computational Hypothesis

To Simulate time dependent phenomena numerically, some computational hypothesis are considered. Incompressible flow is computed numerically by unsteady RANS equations and hydroacoustic effect is ignored.

### 3.2 Incompressible Viscous Flow

The disadvantage of incompressible flow assumption is the missing hydroacoustic effects. For the case of strong pressure fluctuations, the pressure field may interact with the surrounding structure and generates a hydroacoustic pressure field in the whole of the machine and piping system. This mentioned phenomenon plays an important role on the dynamics of the installation for the case of resonance. These waves propagate at sound speed in the installation and may excite the eigenfrequency of the structure [25] [54].

To identify the hydroacoustic effects, the following values should be determined: The length of the channels,  $l$ , the cross section area,  $A$ , the friction coefficient,  $\lambda$ , and the wave speed,  $a$ . The wave speed in a turbine is given by[75]:

$$a^2 = \frac{1}{\rho \left( \frac{1}{E_{fluid}} + \frac{\Delta A}{A \Delta p} \right)} \quad (3.1)$$

where  $E_{fluid}$  is the bulk modulus of the water and  $\frac{\Delta A}{A \Delta p}$  is the rated area increase due to pressure increase. The flow compressibility is characterized by the Mach number, which is the ratio of flow velocity to speed of sound:

$$M = \frac{C}{a_s} \quad (3.2)$$

If the very small Mach number,  $M \ll 1$ , the hypothesis of incompressible flow might be considered. In the incompressible numerical simulation, the parameters,  $A$ ,  $\rho$ , are fixed and the value of wave speed,  $a$ , is infinite, thereby, hydroacoustic effects are ignored.

### 3.2.1 Fundamental Equations of Fluid Mechanics

#### Mass Conservation

According to the law of mass conservation, mass could neither be created nor destroyed. Thereby, if the rate of incoming mass into a control volume exceeds the rate of outgoing, this difference will accumulate within the control volume.

$$\frac{d}{dt} \int_V \rho dv = \int_V \left[ \frac{\partial \rho}{\partial t} + \vec{\nabla} \cdot (\rho \vec{C}) \right] dv = 0 \quad (3.3)$$

where  $\rho$  is density and  $V$  is control volume. In the case of an incompressible flow, mass conservation equation is expressed in a cartesian coordinates system as follows [34]:

$$\frac{\partial C_i}{\partial x_i} + \frac{\partial C_j}{\partial x_j} + \frac{\partial C_k}{\partial x_k} = 0 \quad (3.4)$$

#### Momentum Equation

The momentum equation is derived from Newton's second law and describes fluid motion. It is expressed as below:

$$\frac{\partial}{\partial t} \int_V \vec{C} \rho dv + \int_{\partial V} \rho \vec{C} \vec{C} d\vec{a} = \vec{f} \quad (3.5)$$

where  $\rho$  is density,  $\vec{C}$  is velocity,  $V$  is control volume and  $\partial V$  is the area enclosing. Considering the force acting on the incompressible fluid, the last equation, Equation 3.5, is expressed as below:

$$\frac{\partial C_i}{\partial t} + C_i \frac{\partial C_i}{\partial x_i} + C_j \frac{\partial C_i}{\partial x_j} + C_k \frac{\partial C_i}{\partial x_k} = g_i + \frac{\partial \sigma_{ii}}{\partial x_i} + \frac{\partial \tau_{ij}}{\partial x_j} + \frac{\partial \tau_{ik}}{\partial x_k} \quad (3.6)$$

Equation 3.6 is the differential equation of motion for any fluid satisfying the continuum assumption. To be able to solve Equation 3.6 the stress tensors should be obtained in terms of the velocity and Pressure fields.

#### Viscous Flow

For a Newtonian fluid, the viscous stress is proportional to the rate of shearing strain. The stress tensors may be expressed in terms of velocity gradients and fluid properties as follows, where  $\nu = \frac{\rho}{\mu}$  is the dynamic viscosity :

$$\tau_{ij} = \nu \left[ \frac{\partial C_j}{\partial x_i} + \frac{\partial C_i}{\partial x_j} \right] \quad (3.7)$$

$$\sigma_{ii} = -\frac{p}{\rho} - \nu \left[ \frac{2}{3} \nabla \cdot \vec{C} + 2 \frac{\partial C_i}{\partial x_i} \right] \quad (3.8)$$

### 3.2.2 Navier-Stokes Equations

Momentum conservation equation of a Newtonian, incompressible flow is known as Navier-Stokes equations are expressed by:

$$\frac{\partial C_i}{\partial t} + C_i \frac{\partial C_i}{\partial x_i} + C_j \frac{\partial C_i}{\partial x_j} + C_k \frac{\partial C_i}{\partial x_k} = g_i - \frac{1}{\rho} \frac{\partial p}{\partial x_i} + \nu \left[ \frac{\partial^2 C_i}{\partial x_i^2} + \frac{\partial^2 C_i}{\partial x_j^2} + \frac{\partial^2 C_i}{\partial x_k^2} \right] \quad (3.9)$$

### Reynolds Averaged Navier-Stokes Equations (RANS)

The exact flow motion with all turbulent details are included in Equations 3.9. Limitation of the computing resource capacities is the difficulty to use exact equations. According to the statistical approach that is suggested by Osborne Reynolds, the instantaneous velocity  $C_i$  and instantaneous pressure  $p$  might be separated into averaged and fluctuating quantities:

$$C_i = \overline{C_i} + C'_i \quad , \quad p = \overline{p} + p' \quad (3.10)$$

where the mean quantities are defined as:

$$\overline{C_i} = \frac{1}{t_2 - t_1} \int_{t_1}^{t_2} C_i dt \quad , \quad \overline{p} = \frac{1}{t_2 - t_1} \int_{t_1}^{t_2} p dt \quad (3.11)$$

Introducing Equation 3.10 into momentum equation and applying white noise fluctuation assumption  $\overline{C'} = 0$ , yields Reynolds Averaged Navier-Stokes equations (RANS), written as:

$$\frac{\partial \overline{C_i}}{\partial t} + \overline{C_i} \frac{\partial \overline{C_i}}{\partial x_i} + \overline{C_j} \frac{\partial \overline{C_i}}{\partial x_j} + \overline{C_k} \frac{\partial \overline{C_i}}{\partial x_k} = g_i - \frac{1}{\rho} \frac{\partial \overline{p}}{\partial x_i} + \nu \nabla^2 \overline{C_i} - \frac{\partial \overline{C'_i C'_i}}{\partial x_i} - \frac{\partial \overline{C'_i C'_j}}{\partial x_j} - \frac{\partial \overline{C'_i C'_k}}{\partial x_k} \quad (3.12)$$

### 3.2.3 Turbulence Modeling

Turbulence regime is characterized by three-dimensional eddying random motions in addition to the mean main flow velocity. In a turbulent flow a wide spectrum of eddy sizes and corresponding fluctuation frequencies are generated and diffused. Figure 3.1 represents the spectra of turbulence energy and dissipation in function of wave number [72]. The mechanism of turbulence flow can be explained by the Kolmogorov theory. Accordingly, energy from the main flow is injected into the large scale eddies, then dissipated and transported into the small eddies. This process is illustrated schematically in Figure 3.2. The small eddies with the high fluctuation frequencies are too small to influence the mean main flow velocity. The largest eddies, which are associated with low frequency fluctuations, interact with the mean main flow while, they have similar scales. It is mainly the large-scale turbulent motion that transports momentum and contributes to the turbulence correlation  $\overline{C'_i C'_j}$  that is called Reynolds stress term. Due to the complexity of the exact turbulence motion, the goal of turbulence models is to derive simple formulations for the Reynolds stress term. The complexity of the turbulence models from the modeling to the full simulation, large eddy simulation, is presented in the Figure 3.3.

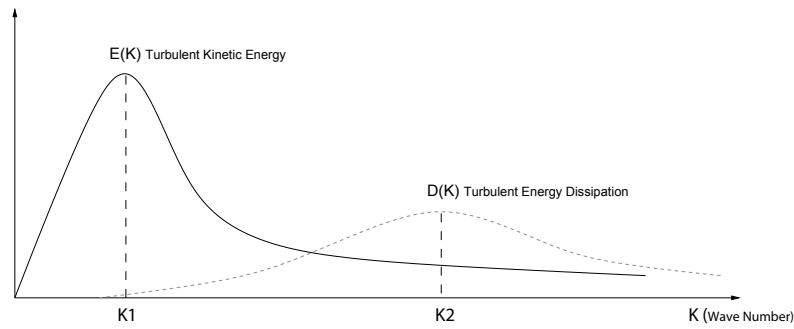


Figure 3.1: Sketch of turbulence energy and dissipation rate in function of wave number

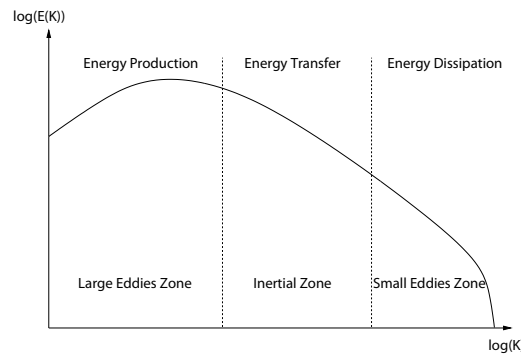


Figure 3.2: The cycle of turbulence energy production and dissipation

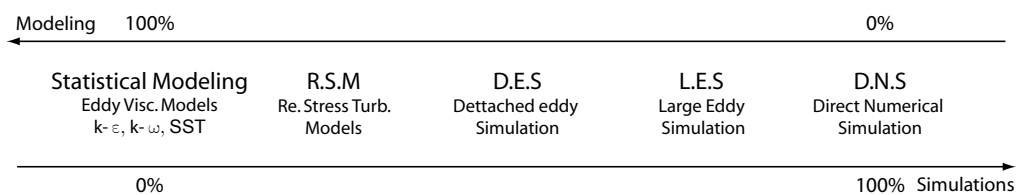


Figure 3.3: The complexity of the turbulent models to the direct numerical simulations

### Eddy Viscosity Turbulence Models

The concept of eddy viscosity turbulence models characterizes the large-eddy motions with an artificial viscosity that is called eddy viscosity. In these models, the small eddies in the motion are ignored. This concept enables to model the transport and dissipation of turbulence energy,  $k$ .

$$k = \frac{1}{2} \overline{C_i' C_j'} = \frac{1}{2} \left( \overline{C_i'^2} + \overline{C_j'^2} + \overline{C_k'^2} \right) \tag{3.13}$$

The transport equation of turbulent energy is defined as:

$$\frac{\partial k}{\partial t} + C_j \frac{\partial k}{\partial x_j} = \tau_{ij} \frac{\partial C_i}{\partial x_j} - \varepsilon + \frac{\partial}{\partial x_j} \left[ \nu \frac{\partial k}{\partial x_j} - \frac{1}{2} \overline{C'_i C'_j C'_k} - \frac{1}{\rho} \overline{p' C'_j} \right] \quad (3.14)$$

The left hand side of Equation 3.14 corresponds to the unsteady and convection terms of turbulence energy. The first term on the right hand side is called production and indicates the rate of kinetic energy of turbulence, fed by main flow. The second term, dissipation  $\varepsilon$ , is the rate of conversion of kinetic energy to thermal energy, which is defined by the following correlation.

$$\varepsilon = \nu \frac{\partial \overline{C'_i C'_i}}{\partial x_j \partial x_j} \quad (3.15)$$

The term  $\nu \frac{\partial k}{\partial x_j}$  represents the kinetic energy diffusion due to molecular diffusion. The term  $\frac{1}{2} \overline{C'_i C'_j C'_k}$  is the rate of transportation of turbulence energy by the velocity fluctuations. The last term,  $\frac{1}{\rho} \overline{p' C'_j}$ , corresponds to the last mentioned physical characteristics, resulting from correlation of pressure and velocity fluctuations. According to the first 'Eddy Viscosity Model' proposed by Boussinesq, the Reynolds stress terms are proportional to mean velocity gradients as:

$$\tau_{ij} = \nu_t \left( \frac{\partial C_i}{\partial x_j} + \frac{\partial C_j}{\partial x_i} \right) - \frac{2}{3} k \delta_{ij} \quad (3.16)$$

where  $\nu_t$  is the eddy (turbulent) viscosity and  $\delta_{ij}$  is the Kronecker symbol.

To estimate the turbulent transport and pressure diffusion there is no experimental data. It is the reason that generally they are grouped with turbulent transport term. Thus this terms could defined as:

$$\frac{\nu_T}{\sigma_k} \frac{\partial k}{\partial x_j} = - \frac{1}{2} \overline{C'_i C'_j C'_k} - \frac{1}{\rho} \overline{p' C'_j} \quad (3.17)$$

The manner, in which the term of diffusion is determined, varies with the turbulence models. Two-equation turbulence models are very widely used, as they offer a good compromise between numerical effort and computational accuracy. In these models, the turbulent length scale and turbulence velocity scale are estimated from the turbulent kinetic energy and its dissipation rate. The  $k$ - $\varepsilon$ ,  $k$ - $\omega$ , SST turbulence models are based on this concept [19] [70]. The accurate prediction of flow separation from a smooth surface represents one of the main problems in turbulence modeling. Standard two-equation turbulence models often fail to predict the onset and the amount of flow separation under adverse pressure gradient conditions. The models developed to solve this problem have shown a significantly more accurate prediction of separation in a number of test cases and in industrial applications.

### $k$ - $\varepsilon$ Turbulence Models

The  $k$ - $\varepsilon$  model is one of the most prominent turbulence models. It has been implemented in most general purpose CFD codes and it is considered as the industrial standard model [99]. It has proven to be stable and numerically robust and has a well established regime of predictive capability. For general purpose simulations, the  $k$ - $\varepsilon$  model offers a good compromise in terms of simulation time, accuracy and robustness. Turbulent kinetic energy,  $k$  and dissipation,  $\varepsilon$ , transport equations are resolved in this model. With the Prandtl-Kolmogorov analogy, the eddy viscosity is specified as:

$$\nu_t = C_\mu \frac{k^2}{\varepsilon} \quad (3.18)$$

By considering, Equation 3.17 and Equation 3.14, the model uses the following transport equation for turbulence Kinetic Energy:

$$\frac{\partial k}{\partial t} + C_j \frac{\partial k}{\partial x_j} = \frac{\partial}{\partial x_j} \left[ \left( \nu + \frac{\nu_t}{\sigma_k} \right) \frac{\partial k}{\partial x_j} \right] + \tau_{ij} \frac{\partial C_i}{\partial x_j} - \varepsilon \quad (3.19)$$

Dissipation rate transport equation:

$$\frac{\partial \varepsilon}{\partial t} + C_j \frac{\partial \varepsilon}{\partial x_j} = \frac{\partial}{\partial x_j} \left[ \left( \nu + \frac{\nu_t}{\sigma_\varepsilon} \right) \frac{\partial \varepsilon}{\partial x_j} \right] + \frac{\varepsilon}{k} (C_{1\varepsilon} \tau_{ij} \frac{\partial C_i}{\partial x_j} - C_{2\varepsilon} \varepsilon) \quad (3.20)$$

The model contains five adjustable constants derived from experiments:

$$C_\mu = 0.09; \quad \sigma_k = 1.00; \quad \sigma_\varepsilon = 1.30; \quad C_{1\varepsilon} = 1.44; \quad C_{2\varepsilon} = 1.92.$$

### $k$ - $\omega$ Turbulence Models

The  $k$ - $\omega$  model [99] is also a two equation turbulence model. It is based on transport equations for the turbulent kinetic energy,  $k$ , and for the specific dissipation rate  $\omega$  (rate of dissipation per unit of turbulence kinetic energy, often called turbulent frequency). The advantage of  $k$ - $\omega$  over  $k$ - $\varepsilon$  is to perform better in flows with adverse pressure gradients and to give a better prediction of flow separation. In this model the eddy viscosity is expressed by:

$$\nu_t = \frac{k}{\omega} \quad (3.21)$$

Turbulence Kinetic Energy :

$$\frac{\partial k}{\partial t} + C_j \frac{\partial k}{\partial x_j} = \frac{\partial}{\partial x_j} \left[ \left( \nu + \sigma^* \nu_t \right) \frac{\partial k}{\partial x_j} \right] + \tau_{ij} \frac{\partial C_i}{\partial x_j} - \beta^* k \omega \quad (3.22)$$

Specific Dissipation Rate :

$$\frac{\partial \omega}{\partial t} + C_j \frac{\partial \omega}{\partial x_j} = \frac{\partial}{\partial x_j} \left[ \left( \nu + \sigma \nu_t \right) \frac{\partial \omega}{\partial x_j} \right] + \frac{\omega}{k} \left[ \alpha \tau_{ij} \frac{\partial C_i}{\partial x_j} - \beta k \omega \right] \quad (3.23)$$



Closure Coefficients :

$$\alpha = 5/9; \quad \beta = 3/40; \quad \beta^* = 9/100; \quad \sigma = 1/2; \quad \sigma^* = 1/2.$$

Auxiliary Relations :

$$\varepsilon = \beta^* \omega k \quad L_t = \frac{k^{1/2}}{\omega} \quad (3.24)$$

### Shear Stress Transport Model (SST)

Shear stress transport model is a blending between the  $k$ - $\omega$  model near the surface and the  $k$ - $\varepsilon$  model in the outer region, which is developed by Menter [68]. The based Shear-Stress-Transport (SST) model was designed to give a highly accurate prediction of the onset and the amount of flow separation under adverse pressure gradients by the inclusion of transport effects into the formulation of the eddy-viscosity. The SST model is recommended for the boundary layer simulations. To benefit from this model, a resolution of the boundary layer of more than 10 mesh layers is required. By multiplying the Wilcox  $k$ - $\omega$  equations by function  $F_1$ , and the transformed Launder-Spalding  $k$ - $\varepsilon$  equations by  $(1 - F_1)$ , such as below, blending factor performs.

Turbulence Kinetic Energy :

$$\frac{\partial k}{\partial t} + C_j \frac{\partial k}{\partial x_j} = \frac{\partial}{\partial x_j} \left[ \left( \nu + \frac{\nu_t}{\sigma_{k3}} \right) \frac{\partial k}{\partial x_j} \right] + \tau_{ij} \frac{\partial C_i}{\partial x_j} - \beta^* k \omega \quad (3.25)$$

Specific Dissipation Rate :

$$\begin{aligned} \frac{\partial \omega}{\partial t} + C_j \frac{\partial \omega}{\partial x_j} = & \frac{\partial}{\partial x_j} \left[ \left( \nu + \frac{\nu_t}{\sigma_{\omega 3}} \right) \frac{\partial \omega}{\partial x_j} \right] + \frac{\omega}{k} \left[ \alpha_3 \tau_{ij} \frac{\partial C_i}{\partial x_j} - \beta_3 k \omega \right] \\ & + (1 - F_1) 2 \frac{1}{\omega \sigma_{\omega 2}} \frac{\partial k}{\partial x_j} \frac{\partial \omega}{\partial x_j} \end{aligned} \quad (3.26)$$

where the coefficients of the model are a linear combination of the corresponding coefficients of the  $k$ - $\omega$  and modified  $k$ - $\varepsilon$  models ( $\Phi = F_1 \Phi_{k\omega} + (1 - F_1) \Phi_{k\varepsilon}$ ).

Closure coefficients :

$$\begin{aligned} k\text{-}\omega: & \quad \alpha_1 = 5/9; \quad \beta_1 = 3/40; \quad \sigma_{k1} = 2; \quad \sigma_{\omega 1} = 2; \quad \beta^* = 9/100; \\ k\text{-}\varepsilon: & \quad \alpha_2 = 0.44; \quad \beta_2 = 0.0828; \quad \sigma_{k2} = 1; \quad \sigma_{\omega 2} = 1/0.856; \quad C_\mu = 0.09; \end{aligned}$$

The model combines the advantages of the Wilcox  $k$ - $\omega$  and the Launder-Spalding  $k$ - $\varepsilon$  model, but still fails to properly predict the onset and amount of flow separation from smooth surfaces due to the over-estimation of the eddy-viscosity (the transport of the turbulent shear stress not properly taken into account). The proper transport behavior can be obtained by a limiter added to the formulation of the eddy-viscosity:

$$\nu_t = \frac{k}{\max(\omega, SF_2)} \quad (3.27)$$

$F_2$  is a blending function, which restricts the limiter to the wall boundary layer, as the underlying assumptions are not correct for free shear flows.  $S$  is an invariant measure of the strain rate. The SST model gives more accurate predictions of the onset and the amount of flow separation under adverse pressure gradients.

## Space-Filtered Equations Based Models

### Large Eddy Simulations

Turbulent flow contains a wide range of length and time scales. Large Eddy Simulation, LES, focuses on resolving the time-dependent equations for turbulent motion. The main advantage of LES over the statistical models is the high order of turbulence flow details. The Eddy viscosity models provide averaged results, however the LES simulation is able to predict instantaneous flow characteristics and resolve turbulent flow structures. In this method the large eddies, which are proportional to the mean main flow are considered and the effects of the small eddies (small scale) are simulated. There are four conceptual steps in LES; three modeling issues, and one numerical simulation issue.

At first, as the large scale eddies are resolved and the small scale are modeled, a filtering process separates the small scale from the large scale motion. The velocity variable  $C$  represents the sum of mean main flow motion in addition to the large eddy scales,  $\bar{C}$  and small scale of eddies,  $C'$ , can be written such as:

$$C = \bar{C} + C' \quad (3.28)$$

Accordingly, the large scale part, is defined through volume averaging as:

$$\bar{C}(x, t) = \int G(x - x')C(x', t)dx' \quad (3.29)$$

where  $G$  is a filter function.

Secondly, the filtered velocity field is derived from Navier-Stokes equations. The filtered Navier-Stokes equations show a non-linear transport term which can be developed as:

$$\overline{C_i C_j} = \overline{(\bar{C}_i + C'_i) \cdot (\bar{C}_j + C'_j)} = \overline{\bar{C}_i \bar{C}_j} + \overline{\bar{C}_i C'_j} + \overline{C'_i \bar{C}_j} + \overline{C'_i C'_j} \quad (3.30)$$

Then the model introduces the sub-grid scale (SGS) stresses,  $\tau_{ij}$ , as:

$$\begin{aligned} \tau_{ij} &= \overline{C_i C_j} - \bar{C}_i \bar{C}_j \\ &= \overline{\bar{C}_i \bar{C}_j} + \overline{\bar{C}_i C'_j} + \overline{C'_i \bar{C}_j} + \overline{C'_i C'_j} - \bar{C}_i \bar{C}_j \end{aligned} \quad (3.31)$$

In the next step, the closure is obtained by modeling the residual-stress tensor most simply by an eddy-viscosity model and finally, the filtered equations are solved numerically for  $\bar{C}$ , which provides an approximation to the large-scale motions. The different LES variants are based on the filtering techniques and the modeling of the sub-grid scale  $\tau_{ij}$ .

### Scale-Adaptive Simulation (SAS)

Scale-Adaptive Simulation (SAS) is an improved turbulence model, which contains both RANS and LES in a single model formulation. The SAS concept is based on providing two independent scales to the source terms of two-equation models. In addition to the velocity gradient tensor,  $\frac{\partial C_i}{\partial x_j}$ , the second derivative of the velocity field is computed, which is associated with von Karman length-scale,  $L_{vK} = \kappa \left| \frac{\partial C / \partial y}{\partial^2 C / \partial y^2} \right|$ . The information provided

by the von Karman length-scale allows SAS models to dynamically adjust to resolved structures in a Unsteady Reynolds-Averaged Navier-Stokes, URANS, simulation. As a result, the SAS model offers a single framework, which covers both steady state flow, RANS, as well as unsteady regions of the flow field [69] [71]. The derivation of the model is based on the Rotta's  $k - \Phi$  ( $\Phi = \sqrt{k}L$ ) model:

$$\nu_t = c_\mu^{0.25} \Phi \quad (3.32)$$

$$\frac{\partial k}{\partial t} + C_j \frac{\partial k}{\partial x_j} = \frac{\partial}{\partial x_j} \left[ \frac{\nu_t}{\sigma_k} \frac{\partial k}{\partial x_j} \right] + \tau_{ij} \frac{\partial C_i}{\partial x_j} - C_\mu^{0.75} \frac{k^2}{\Phi} \quad (3.33)$$

$$\frac{\partial \Phi}{\partial t} + C_j \frac{\partial \Phi}{\partial x_j} = \frac{\partial}{\partial x_j} \left[ \frac{\nu_t}{\sigma_\Phi} \frac{\partial \Phi}{\partial x_j} \right] + \frac{\Phi}{k} \tau_{ij} \frac{\partial C_i}{\partial x_j} \left[ \zeta_1 - \zeta_2 \kappa \frac{L}{L_{vK}} \right] - \zeta_3 k \quad (3.34)$$

### 3.3 The Solver

ANSYS-CFX commercial code, which served as a platform for the present work is a three-dimensional fully implicit code that solves the RANS and URANS equations with finite volume method. The solver is able to solve the hydrodynamic equations ( $C_i, C_j, C_k, p$ ) in a single system. For steady state problems, the time-step behaves like an "under-relaxation parameter", to guide the approximate solutions in a physically based manner to a steady-state solution. For time dependent problems, like transient rotor-stator simulation, at each time step several predefined iterations are performed. By achieving the target, either residual tolerance or specified maximum iteration number, it passes to the next time step. In the unsteady simulation, the solver allows taking into account the unsteady effects of dynamic flow field for each time step [19].

#### 3.3.1 Advection Scheme

The implemented advection scheme in ANSYS-CFX varies from the upwind 1<sup>st</sup> order to the high accuracy of 2<sup>nd</sup> order. The defined advection terms permit to find the optimum accuracy and robustness. This term is defined as follow:

$$\phi = \phi_{up} + \beta \nabla \phi \cdot \Delta \vec{r}$$

where  $\phi_{up}$  is the value at the upwind node,  $\vec{r}$  is the vector from the upwind node to the computed node, and  $\beta \nabla \phi \cdot \Delta \vec{r}$  is called numerical advection correction. It is an anti-diffusive flux added to the upwind scheme.  $\beta=0$  leads to the first order upwind difference scheme, and  $\beta=1$  is formally second order accurate.

#### 3.3.2 Boundary Conditions

##### Inflow Boundary Condition

The inlet boundary conditions are set either in terms of velocity profile, mass influx or combination of them. The boundary velocity components are specified, with a non-zero

results into the domain as:  $\vec{C} = C_i\vec{e}_i + C_j\vec{e}_j + C_k\vec{e}_k$ . The mass influx is specified along with a direction component. It is calculated using:  $\rho C = \dot{m} / \int_{\partial V} ds$  where  $\int_{\partial V} ds$ , is the integrated boundary surface area at a given mesh resolution.

The inlet turbulence quantities  $k$  and  $\varepsilon$ , are either specified directly or calculated using expressions which scale the distribution at the inlet according to the turbulence intensity  $I = \frac{\tilde{C}}{C}$  and the eddy length scale  $L_t$ . The turbulence kinetic energy and dissipation are calculated using:

$$k_{inlet} = \frac{3}{2} I^2 C^2 \quad \varepsilon_{inlet} = \frac{k^{\frac{3}{2}}}{L_t}$$

### Pressure Boundary Condition

The relative static pressure over the boundary is specified generally for outlet regions.

$$\bar{p}_{spec} = \frac{1}{A} \int_{\partial V} p_n ds$$

where the integral is applied over the entire outlet boundary surface. This condition permits the pressure profile at the outlet section to float, however the average value is constrained to the specified value.

### Solid Boundary Condition

Near the wall region the flow can be subdivided into two layers. In viscous sublayer flow is almost laminar-like. Further away from the wall, the logarithmic law is applied, where turbulence dominates the mixing process. The velocity of the fluid at the wall boundary is set to zero, so the boundary condition for the velocity becomes:  $C_{wall} = 0$ . A rotating wall can be specified in both stationary and rotating frames in hydraulic machines as:  $C_{wall} = \omega R$ . To model flow field at the walls, Scalable Wall Functions are used for all turbulence models based on the  $\varepsilon$ -equation. For  $k - \omega$  based models including the SST model, an Automatic near-wall treatment method is applied.

## 3.3.3 Rotor-Stator Interfaces

To derive numerical simulations in the turbo machines, it is essential to introduce numerical models able to transmit energy fluxes from reference frame, stator, to the relative frame, rotor. The current rotor-stator models are divided into two groups, quasi-steady and transient models. Frozen rotor and stage are two models in quasi-steady category. The advantage of these models are short computing time and using small computational domain reduced to periodic channels. However, transient effects at the frame change interface are neglected. A fully transient model takes into account all unsteady effects.

### Mixing Plane Interface

Rotor-stator mixing plane model is based on the circumferentially averaging flux that crosses the interface into the downstream frame. This model is proposed to predict hydro turbine efficiency value close to the best efficiency operating point.

### **Frozen Rotor Interface**

In the frozen rotor model the rotating domain is frozen at the initial position. All the same, transformation of the flow direction is taken into account appropriate to the rotating frame. In a frozen-rotor simulation no transient effects are included and such rotating phenomena as rotating wakes or leading edge pressure increases will always stay in exactly the same positions. This model is mainly applied to initialize a transient sliding-mesh simulation.

### **Fully Transient Interface**

Time dependent simulation is feasible by using the fully transient model. This model allows taking into account the unsteady effects of dynamic flow field for each time step. The interface position is updated each time step, as the relative position of the grids on each side of interface changes. The governing equation for fluxes, mass and momentum, are conserved on both sides of the interface. The disadvantage of this model is large computing time requirements.

## **3.4 Computing Resources**

The calculations were done by using the EPFL computing resources. The computations are made in parallel environment using PVM and MPI mode in platform based on Unix IBM-AIX 5 architecture. The unsteady computations are done using IBM Blade Server JS20 having 20 x 2proc. PowerPC 970 (64-bit) with 4 G Bytes of RAM each.



## Part II

# ROTOR-STATOR INTERACTION





# Chapter 4

## Numerical Simulation of RSI

### 4.1 Numerical Configurations

#### 4.1.1 Investigated Operating Points

Figure 4.1 indicates the hillchart of the pump-turbine case study as a function of energy coefficient,  $\psi = 2E/(\omega^2 r_1^2)$  and discharge coefficient,  $\varphi = Q/(\pi\omega r_1^3)$ . The set of investigated operating points referred as OP I to OP III. They are selected on a line with constant energy coefficient,  $\psi$ . These investigation operating points permits to study the RSI at a part load, OP I, best efficiency, OP II, and full load, OP III, operating points. The wall pressure measurements are performed for all three mentioned operating points. Table 4.1 indicates the characteristics of the investigated operating points, Energy coefficient, discharge coefficient, discharge and vaneless gap over impeller diameter.

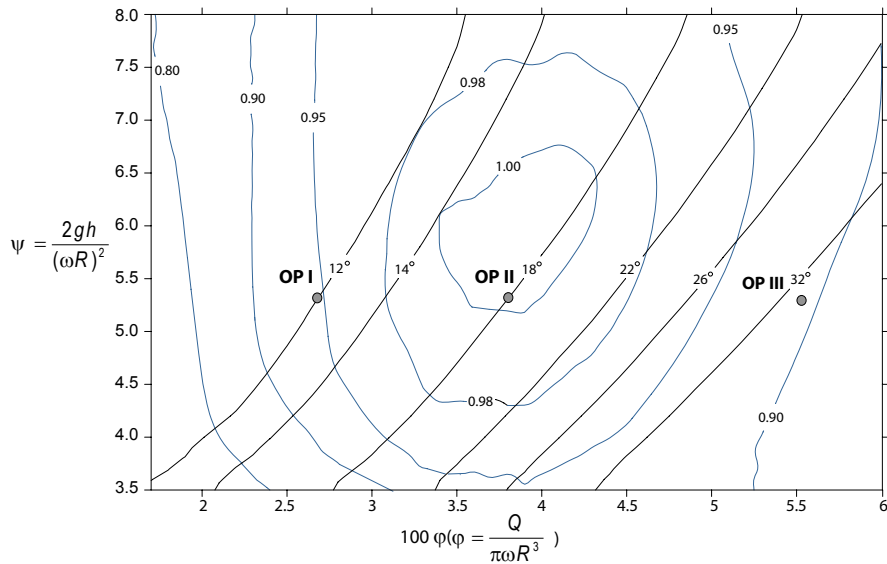


Figure 4.1: Relative efficiency,  $\frac{\eta}{\eta_{max}}$  hillchart of pump-turbine case study and investigated operating points

Table 4.1: The investigated operating points from part load, OP I, to full load, OP III, operating points

Operating point	$\varphi$	$\psi$	$Q/Q_{BEP}$	$r_{gap}/r_1$
OP I	0.258	5.456	0.71	0.12
OP II	0.362	5.275	1	0.10
OP III	0.519	5.254	1.43	0.06

### 4.1.2 Computational Domain

To study the effect of the computational domains on the simulation of RSI, four case studies are defined. The first one, *A*, corresponds to the full pump-turbine water passage, from the spiral casing down to the draft tube. The second case, *B*, involved whole geometry without the spiral casing. Case, *C* is reduced to the guide vane channels, impeller and draft tube and finally, domain *D*, is composed by two periodic channels of stay and guide vanes, one impeller blade and corresponding slice of cone, see Figure 4.2.

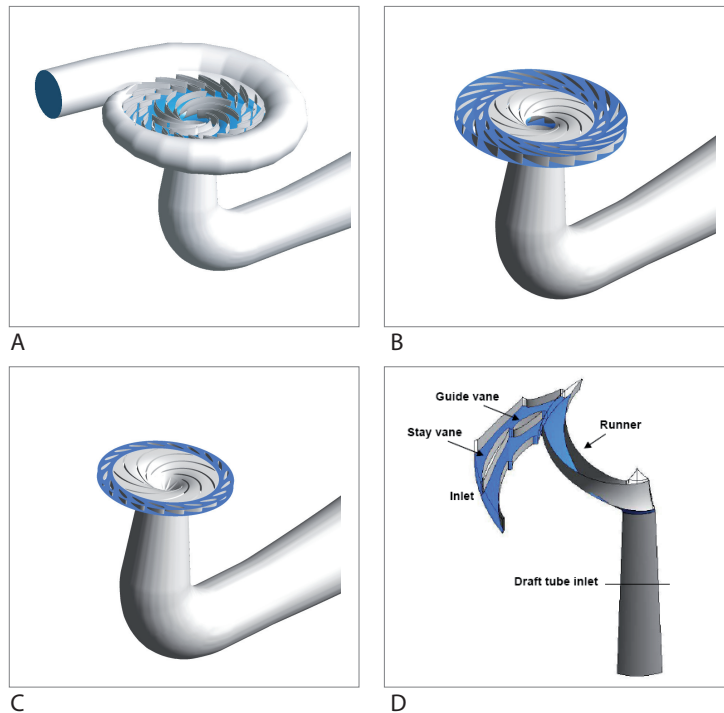


Figure 4.2: Investigated computational domains: *A*) Full geometry, *B*) Radial reduced domain, pump-turbine without spiral casing and *C*) Radial reduced domain, pump-turbine without spiral casing and stay vanes, *D*) Radial and angular reduced domain.

## 4.2 Quality Checks

### 4.2.1 Purpose of Quality Checks

Quality checks are performed to optimize rotor-stator numerical simulation. The reduced computational domain, Case *D*, is applied to find the optimum criteria, such as mesh size, time step value, turbulence model and convergence residual. This domain is composed by two stay vane and guide vane periodic channels, one impeller blade and appropriate slice of the cone. This kind of reduced domain permits to test different mesh refinements, without worrying about capacity of computing resources. Three components of the velocity profile are imposed as the inlet boundary condition. The average static pressure is imposed as the outlet boundary condition and fully transient rotor-stator interface is applied between stator and rotor domains. The numerical and experimental results are compared in one distributor channel as well as in the impeller, see Figure 4.3. Two monitoring points are placed in a guide vane, point 69 and 58, and two others in a stay vane channel, point 34 and 40. These points permit to measure and analyze the pressure fluctuation behavior in a distributor channel. In the impeller, 11 monitoring points are considered on a rotating blade to compare the pressure fluctuations between numerical and experimental results.

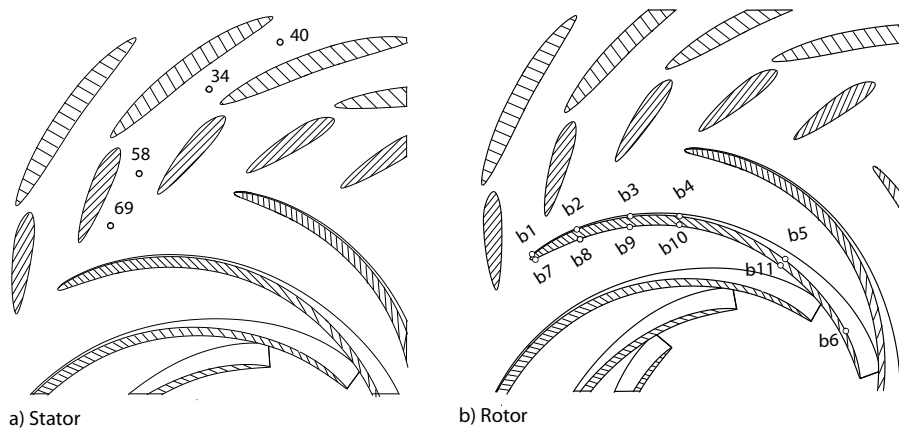


Figure 4.3: Monitoring points used for the results comparison in a guide vane channel (left) and in the impeller (right)

### 4.2.2 Spatial Discretization

Three refinements of spatial discretization (mesh) are generated using the same topology; see Figure 4.4. The influence of the mesh size is studied by analyzing the pressure coefficient in the rotor and stator components; see Table 4.2. Figure 4.5 represents the pressure coefficient amplitude corresponding to the blade passing frequency at the outlet of a guide vane channel, point 69, as well as monitoring point *b1* located at the leading edge of an impeller blade. The amplitude of the pressure fluctuation corresponding to the frequency  $f = z_o \cdot f_n$  is presented as well. Regard to the discrepancy between results of pressure fluctuations for medium and fine meshes and limitation of computing resources, medium mesh is chosen.

Table 4.2: Different mesh sizes used to check mesh sensitivity.

Mesh	Stator channel	Impeller channel
Coarse	30'000	70'000
Medium	60'000	170'000
Fine	130'000	400'000

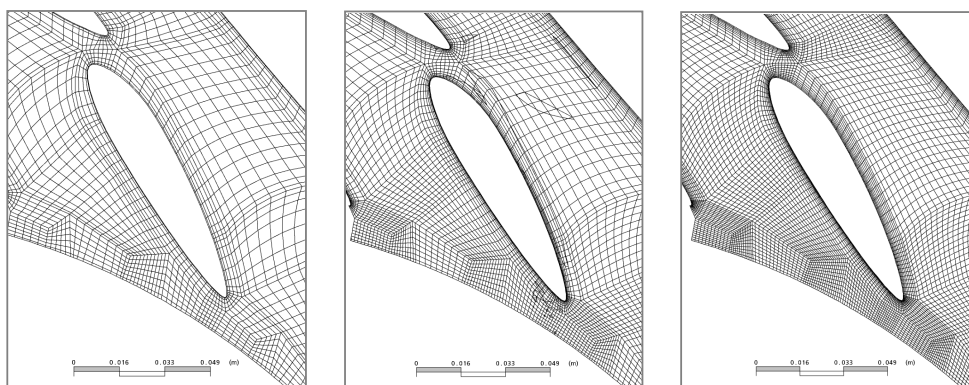
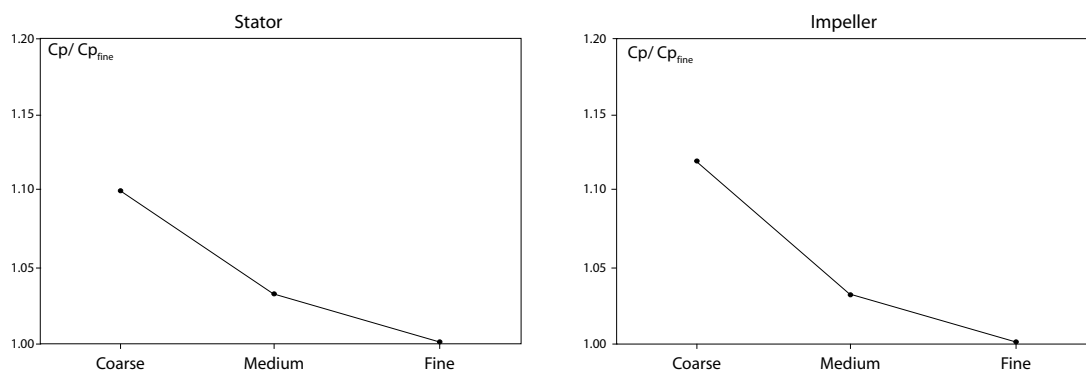


Figure 4.4: Mesh sizes: left) Coarse mesh, middle) Medium mesh, right) Fine mesh

Figure 4.5: Sensitivity of spatial discretization: normalized pressure amplitude at BPF in the vaneless gap (left) and at frequency  $f = 20f_n$  in the impeller (right)

### 4.2.3 Time Discretization

The influence of the time discretization (time step) on the pressure fluctuations in the stator components is investigated. Three time steps corresponding to  $0.5^\circ$ ,  $1^\circ$  and  $2^\circ$  of impeller angular steps are compared. The medium mesh is used for this study.

Figure 4.6 shows pressure fluctuations at the guide vane outlet, monitoring point 69. There is no significant difference among the results at this point. However, this comparison at monitoring point 58 in a guide vane channel shows a non-negligible influence of the time step. Accordingly, a time step corresponding to  $0.5^\circ$  of impeller angular steps is selected.

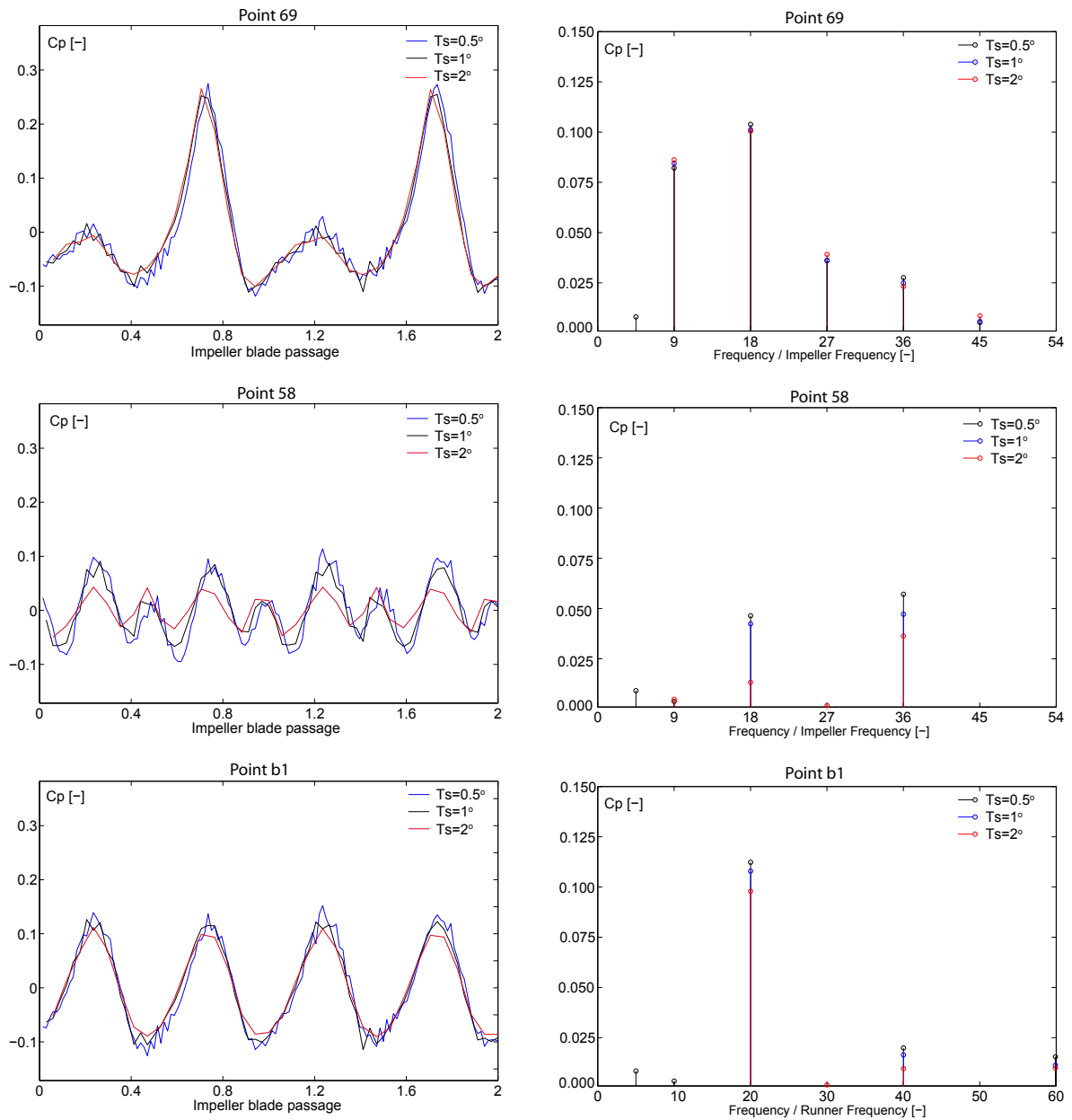


Figure 4.6: Sensitivity of time discretization for pressure fluctuations for the time steps corresponding to  $0.5^\circ$ ,  $1^\circ$  and  $2^\circ$  of impeller angular steps at a monitoring point located in the vaneless gap, point 69 (top), in the guide vane channel, point 58, (middle) and on the leading edge of the impeller blade, point b1, (bottom)

### 4.2.4 Convergence

The numerical convergence in term of maximum residual value in the domain is set to  $10^{-2}$ ,  $10^{-3}$  and  $10^{-4}$ . Medium mesh with a time step corresponding to  $0.5^\circ$  of impeller angular steps is used for this simulation. Figure 4.7 shows the pressure coefficient for one monitoring point at the outlet of the guide vane channel, point 69, and at the leading edge of a rotating blade, point *b1*. The results indicate no significant discrepancy among the three convergence criteria. Thereby, maximum residual value  $10^{-2}$  is applied for the rotor-stator simulation.

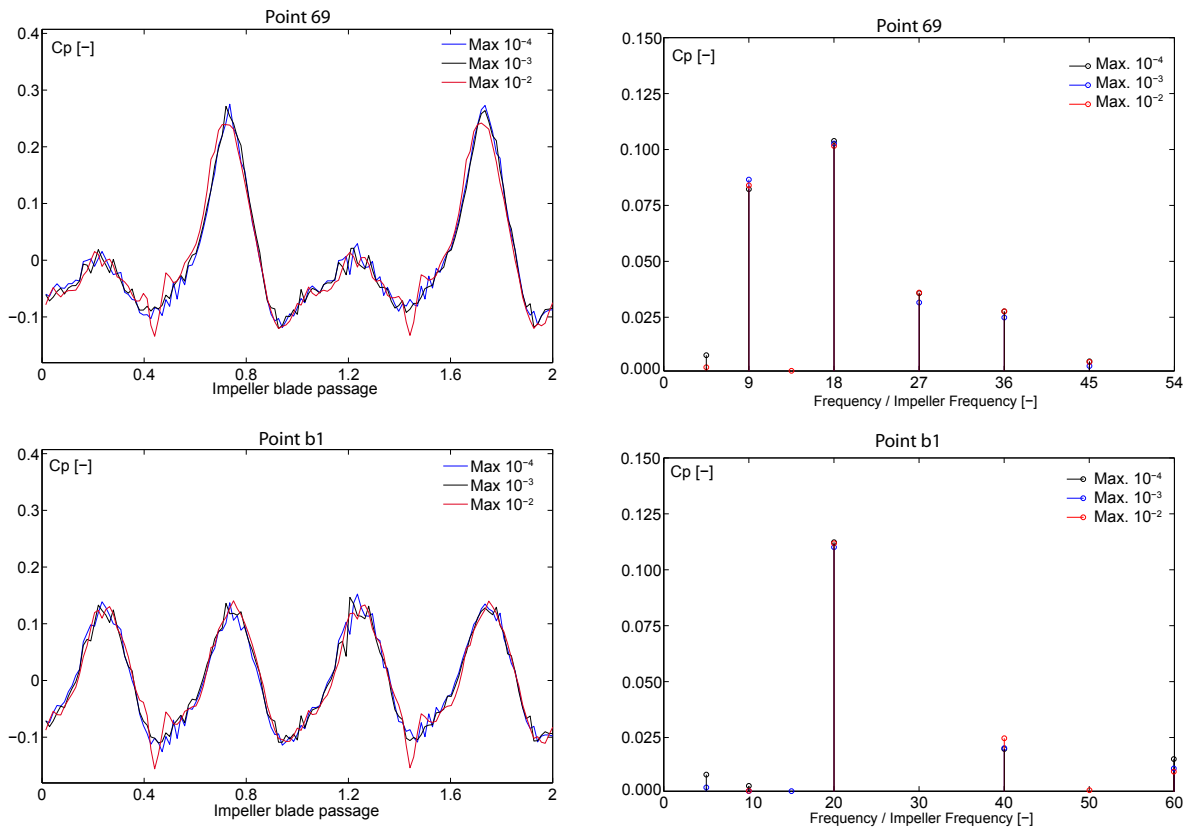


Figure 4.7: Convergence sensitivity for pressure fluctuations, set to values  $10^{-2}$ ,  $10^{-3}$  and  $10^{-4}$  at a monitoring point located in the vaneless gap, point 69, (top) and on the leading edge of the impeller blade, point *b1* (bottom)

### 4.2.5 Turbulence Models

Three turbulence models,  $k-\varepsilon$ , SST and SAS, are applied. This procedure helps to put in evidence the turbulence model influence onto the predicting pressure fluctuations due to the RSI. Figure 4.8 represents the pressure fluctuations and spectral analysis of pressure fluctuations modeling by the different turbulence models in the stator and impeller. Accordingly, the effect of tested turbulence models on the pressure fluctuations is negligible. Thereby,  $k-\varepsilon$  turbulence model, which needs less computational time, is selected.

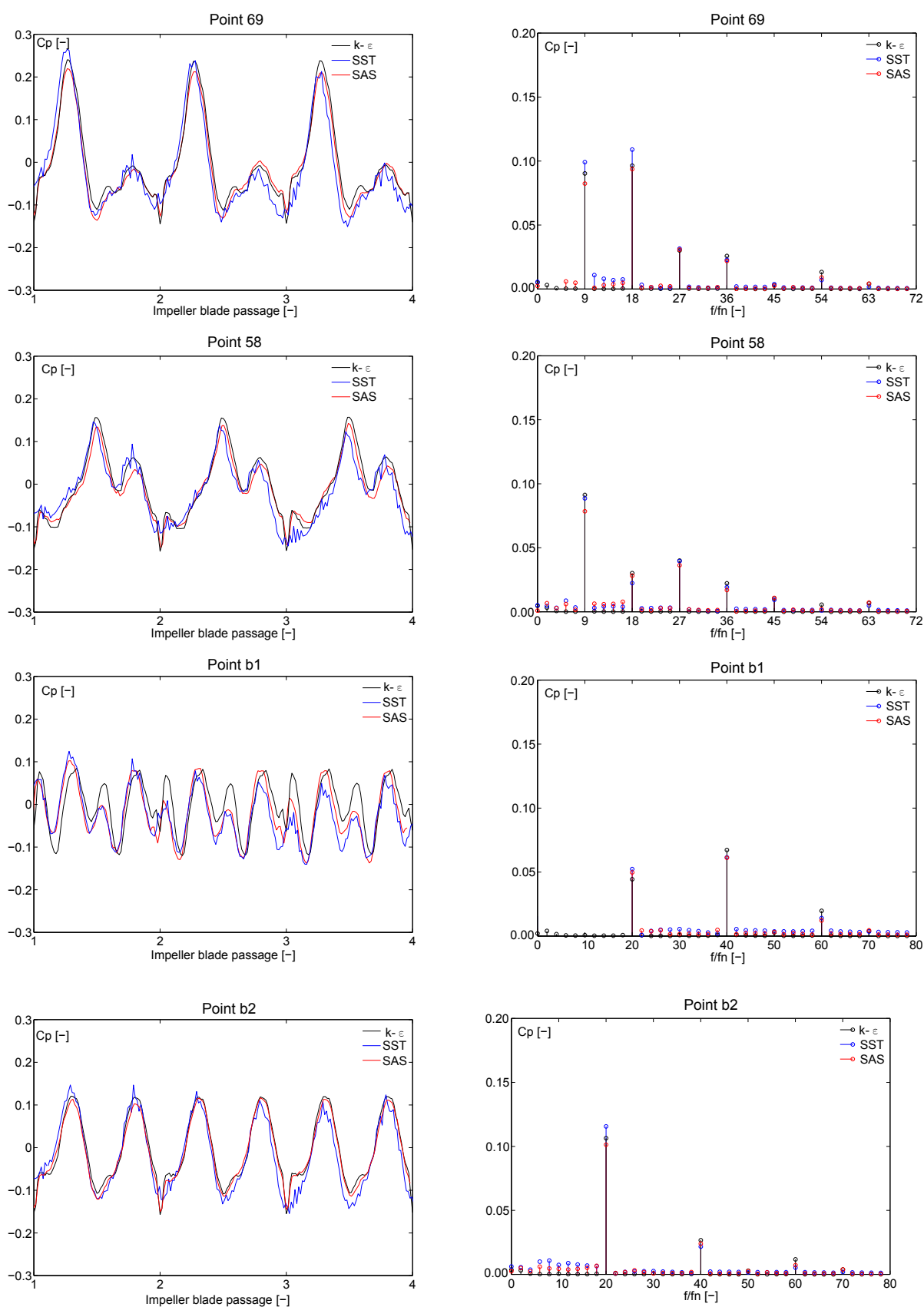


Figure 4.8: Effect of turbulence models in the stator (point 69 and point 58) and on the impeller blades (point *b1* and point *b2*)

## 4.2.6 Reduced Computational Domains

Figure 4.9 represents three computational domains, which are used to investigate the effects of reduced domains on RSI. These simulations are evaluated in a guide vane and an impeller blade channel. Figure 4.10 shows the time history and spectral analysis of pressure fluctuation at two points in guide vane channel. Point 69, close to the rotor-stator vaneless gap and point 58, which is located in the guide vane channel.

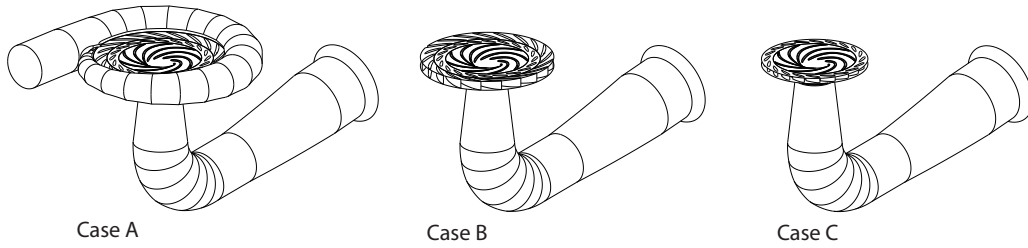


Figure 4.9: Three investigated computational domains: *A)* Full geometry, *B)* Reduced domain, pump-turbine without spiral casing and *C)* Reduced domain, pump-turbine without spiral casing and stay vanes

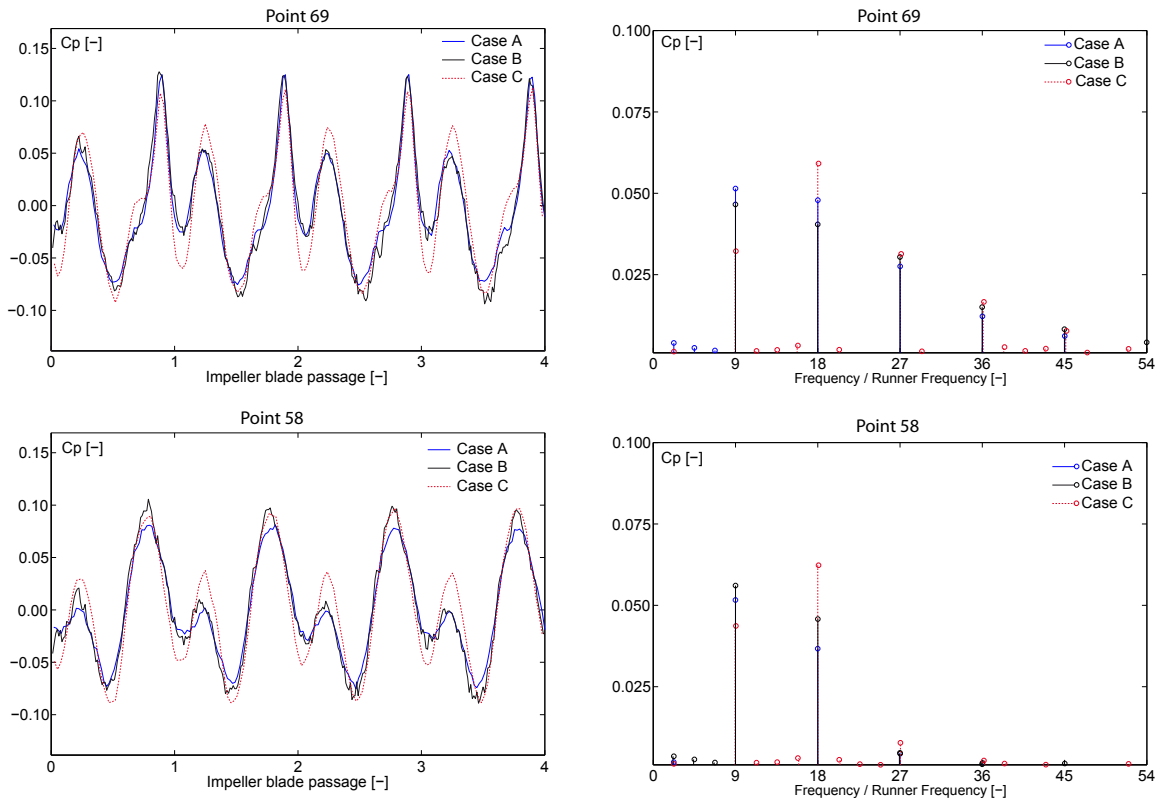


Figure 4.10: BEP operating point, OP II: Time history oscillations and spectral analysis of pressure coefficient, comparison between three computational domains in the vaneless gap, point 69, and guide vane channel, point 58.



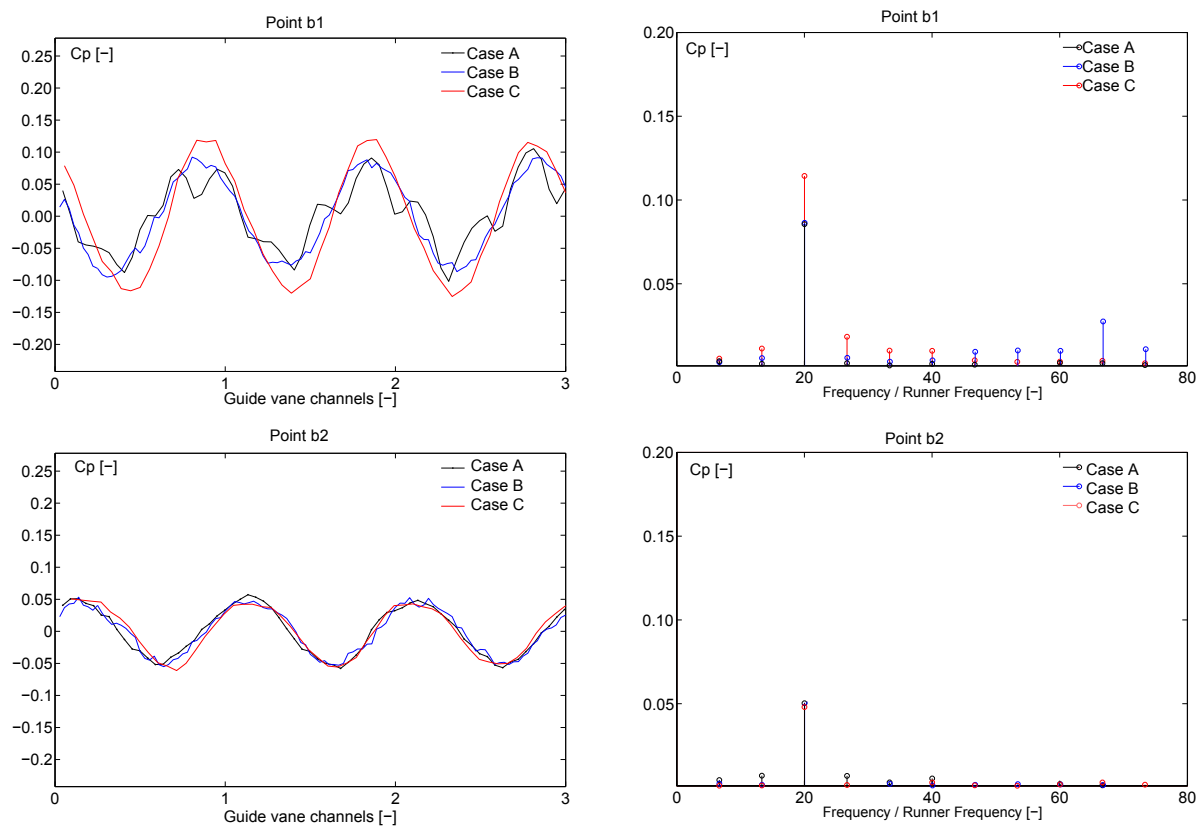


Figure 4.11: Best efficiency point, OP II: Time history oscillations and spectral analysis of pressure coefficient, comparison between three computational domains at the pressure side of an impeller blade

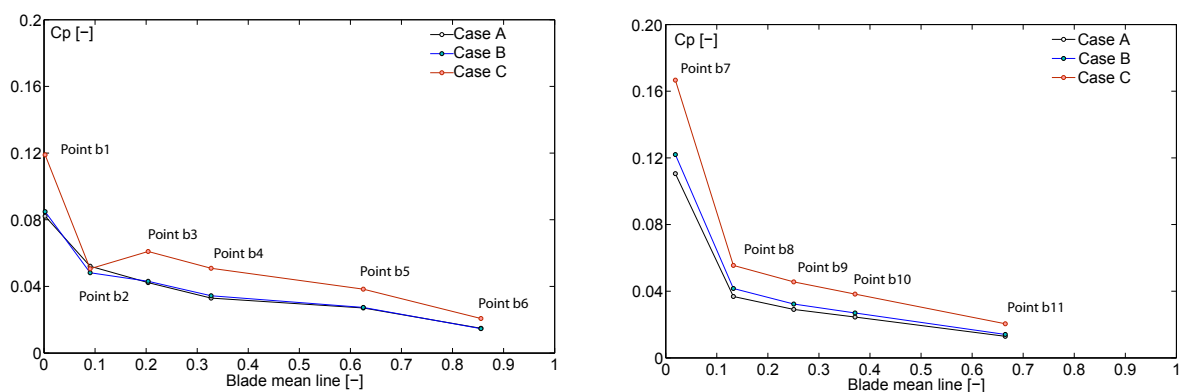


Figure 4.12: Best efficiency operating point, OP II: Pressure amplitude corresponding to the blade passing frequency,  $f = z_o \cdot f_n$ .

As it is shown, for cases *A* and *B*, the pressure amplitude at point 69 has a quite good agreement at the blade passing frequency and its harmonics. The pressure amplitude at blade passing frequency is underestimated for case *C*. However, the pressure amplitude at frequency  $f = 18f_n$  is over estimated in the case *C* as compared to cases *A* and *B*. The results of pressure fluctuation at point 58 shows the same tendency. The numerical results of RSI in the impeller are evaluated as well for all three mentioned cases. The pressure amplitude at the monitoring point *b1* is over estimated for case *C* as compared to case *A* and *B*. However at the monitoring point *b2* all three cases predicted the same pressure amplitudes, see Figure 4.11. The pressure amplitudes corresponding to the monitoring points *b1* to *b11* at the frequency  $f = 20f_n$  are represented in Figure 4.12.

### 4.2.7 Selected Configuration

Three-dimensional unsteady Reynolds-Averaged Navier-Stokes flow computations with the  $k - \varepsilon$  turbulence model and logarithmic wall functions are performed. These simulations are accomplished by the help of CFD package of ANSYS-CFX code. The code is able to solve full transient rotor-stator conditions. The medium mesh is used with the time discretization set to  $0.5^\circ$  and the maximum convergence is fixed to  $10^{-4}$ . Second-order discretization schemes in time and in space are used. The boundary conditions are summarized in Table 4.3.

Table 4.3: Applied boundary conditions

Boundary condition	Option
Inflow	Velocity field
Outflow	Const. Avg. pressure
Wall	Log. Law

### 4.2.8 Meshing

Block structured meshes are used in the whole computing domain. Spiral casing and distributor meshes are connected to each other by a fluid-to-fluid interface, Figure 4.13. In the vaneless gap zone, a mesh refinement is performed in both stationary and rotating parts to model correctly the unsteady flow features. The mesh generation process is carried out with ICEMCFD5 mesh generator software. The mesh characteristics for each component are summarized in Table 4.4.

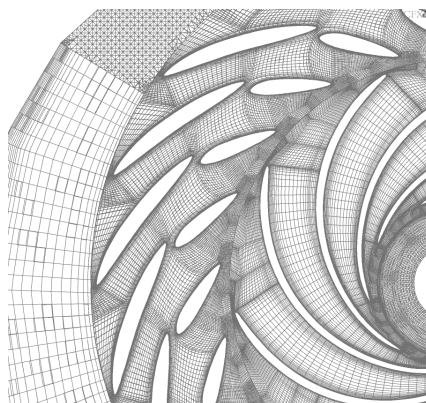


Figure 4.13: General view of the used meshes on a plane perpendicular to the axis of rotation

Table 4.4: Mesh characteristics of the computational domain

Components	Nodes	Min. Angle	$Av.y^+$
Spiral casing	400'000	23°	120
Stay vane & Guide vane	60'000/Channel	32°	100
Impeller	170'000/Channel	30°	60
Draft tube	300'000	41°	270

## 4.3 Results Comparison of RSI

### 4.3.1 Pressure Fluctuations in the Spiral Casing

The pressure fluctuations resulting from numerical simulations and measurements are compared at three investigated operating points, OP I, OP II and OP III. Experimental phase-averaged data and numerical results of one impeller revolution are used for these comparisons. The results of 11 pressure sensors installed at the inner wall of the spiral casing are used to compare with the numerical results, see Figure 4.14. Figure 4.15 represents the phase-averaged of pressure fluctuations resulting from measurements and CFD during one impeller revolution at monitoring point 1. Accordingly, the pressure fluctuations due to the RSI are clearly higher than measurements. It is supposed that the influence of the connected circuit in the experience of being at origin of this important difference [60]. In these numerical simulations, stationary boundary conditions are considered, constant flow rate at the inlet and static pressure at the outlet. The pressure reflection at the inlet boundary provided over estimated the pressure fluctuations values with respect to the corresponding experimental values. To highlight the influence of the

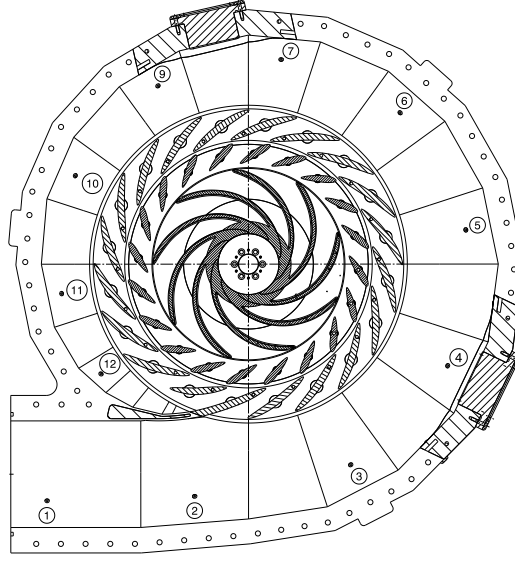


Figure 4.14: The position of the monitoring points in the spiral casing

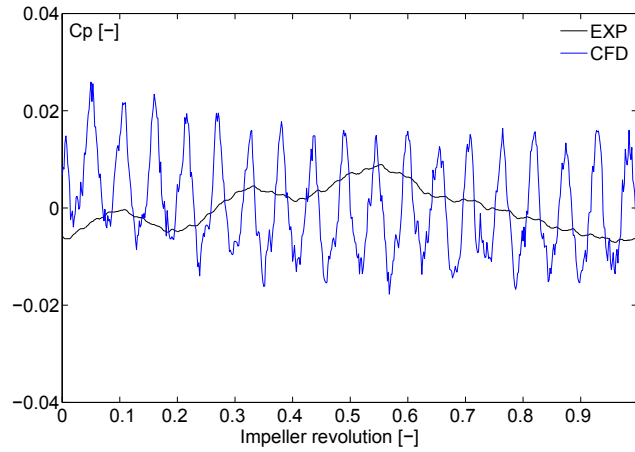


Figure 4.15: Full load operating point OP III: Pressure fluctuation resulting of numerical simulation and measurements at the inlet of spiral casing, point 1

inlet boundary conditions, two kinds of pressure coefficients are defined as below:

$$\tilde{C}_p = \frac{\tilde{p}}{\frac{1}{2} \cdot \rho U_1^2}, \quad C_p = \frac{\tilde{p} - \tilde{p}_{inlet}}{\frac{1}{2} \cdot \rho U_1^2} \quad (4.1)$$

where  $\tilde{p} = p - \bar{p}$  is the instantaneous pressure fluctuation value. Pressure coefficient,  $C_p$ , is defined as a way to eliminate the inlet pressure fluctuations.

The numerical pressure fluctuations resulting from both definitions are compared with the experimental results. The corresponding spectral analysis indicates that the frequency

corresponding to the twice of the blade passing frequency is the dominant frequency in all spiral casing domain. The coefficient pressure amplitudes,  $\tilde{C}_p$  and  $C_p$ , and the phase at this frequency are represented in Figure 4.16 and Figure 4.17. According to the Figure 4.16, the pressure amplitudes indicate two pressure peaks. Comparing the pressure amplitude corresponding to the frequency twice of the blade passing frequency illustrate a big difference between CFD and Experimental results, although the pattern of both results are the same. The first one is measured at monitoring point 6 and the second one is observed at the closing part of the tongue. At the monitoring point 9 a minimum pressure amplitude is measured.

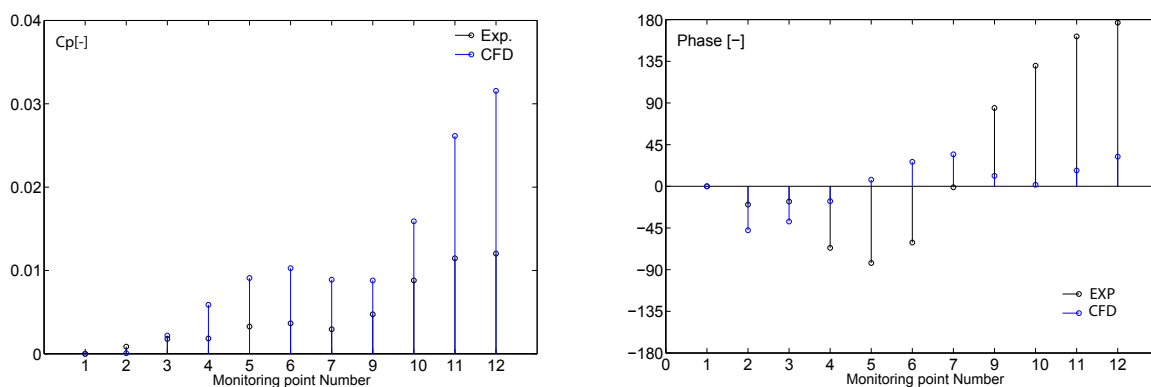


Figure 4.16: Full load operating point OP III: Comparison between the amplitudes of pressure coefficient,  $C_p$  and phase resulting of the simulation and measurement at the frequency  $f = 18 \cdot f_n$ , in the spiral casing, point 1 to point 12.

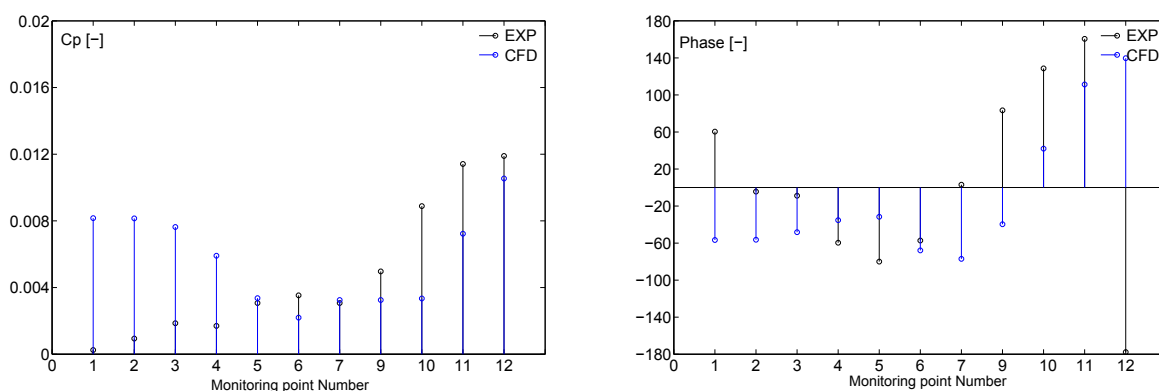


Figure 4.17: Full load operating point OP III: Comparison between the amplitudes of pressure coefficient,  $\tilde{C}_p$  and phase resulting of the simulation and measurement at the frequency  $f = 18 \cdot f_n$ , in the spiral casing, point 1 to point 12.

### 4.3.2 Pressure Fluctuations in the Stator

At the part load operating point, RSI is relatively weak. Figure 4.18 represents the comparison between numerical and experimental results at OP I. The corresponding spectral analysis highlights the pressure amplitude values at the impeller blade passing frequency and its harmonics. In the vaneless gap, monitoring point 69, the amplitude of the blade passing frequency is overestimated by the numerical simulation with respect to the experimental results. However, the absolute discrepancy of pressure coefficient is very low. The pressure amplitude corresponding to the frequency  $f = 18f_n$  is higher than the pressure amplitude of blade passing frequency. These values decrease passing through the guide vane channel to the monitoring point 58. The comparison indicates a good agreement between numerical and experimental results. According to the spectral analysis the pressure amplitude at frequency of  $f = 18f_n$  decreases to half comparing with the corresponding value in the vaneless gap. At monitoring points 34 and 40, which are placed in the stay vane channel, the last mentioned frequency remains the only out standing harmonic in the spectral analysis. Besides, the related pressure amplitude is negligible.

Results at the best operating point, OP II, are given in Figure 4.19. Increasing the discharge flow and decreasing the vaneless gap induce high pressure fluctuations in the rotor-stator zone. At the monitoring point 69 the pressure amplitude at the twice of blade passing frequency is doubled. Regarding the harmonic frequencies, the pressure amplitude shows a good agreement with the measurements in the zone of vaneless gap. However, at the point 58 that is located in the guide vane channel, the predicted numerical pressure fluctuation is over estimated.

Figure 4.20 represents the related results at full load operating point, OP III. The results show consistency between measured and computed values. As it is presented at all investigated operating points, the pressure amplitude at the blade passing frequency through the guide vane channel towards the stay vanes decreases and finally vanishes in the stay vane channel. However, the pressure amplitude at frequency  $f = 18f_n$  is observed at the stay vane inlet.

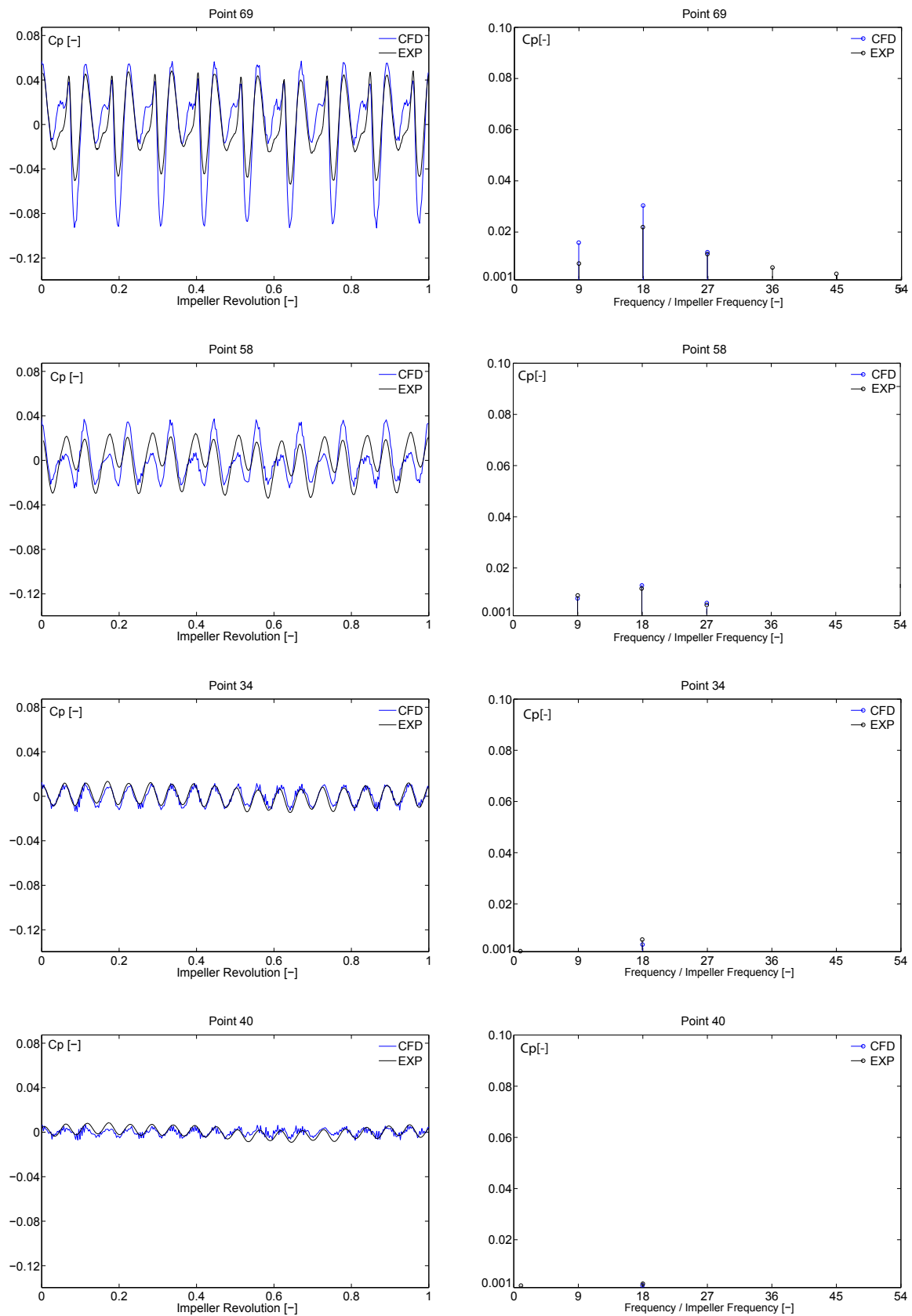


Figure 4.18: Part load operating point, OP I: Time history oscillations and spectral analysis of pressure coefficient in a distributor channel, numerical and experimental results

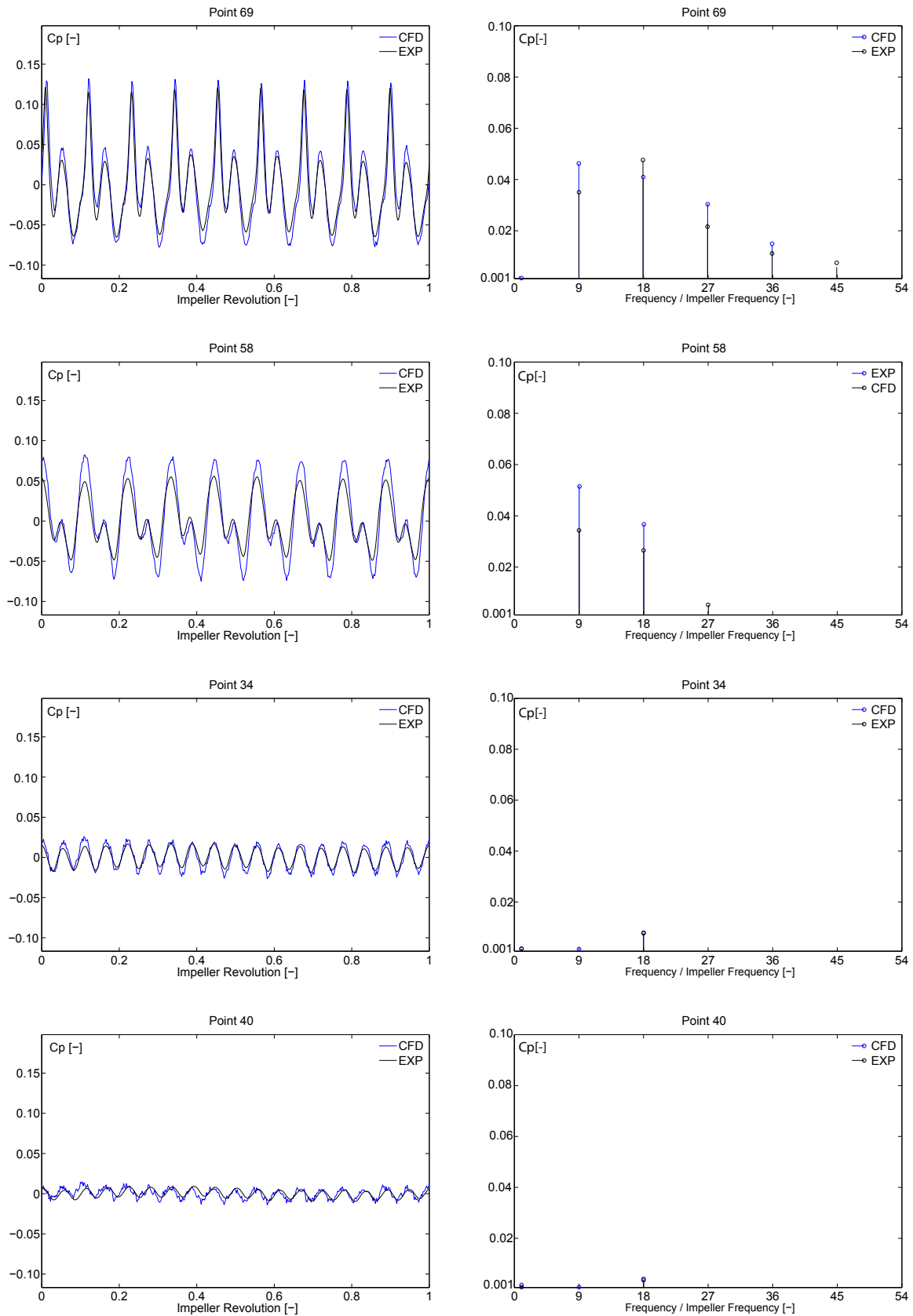


Figure 4.19: Best efficiency point, OP II: Time history oscillations and spectral analysis of pressure coefficient in a distributor channel, numerical and experimental results



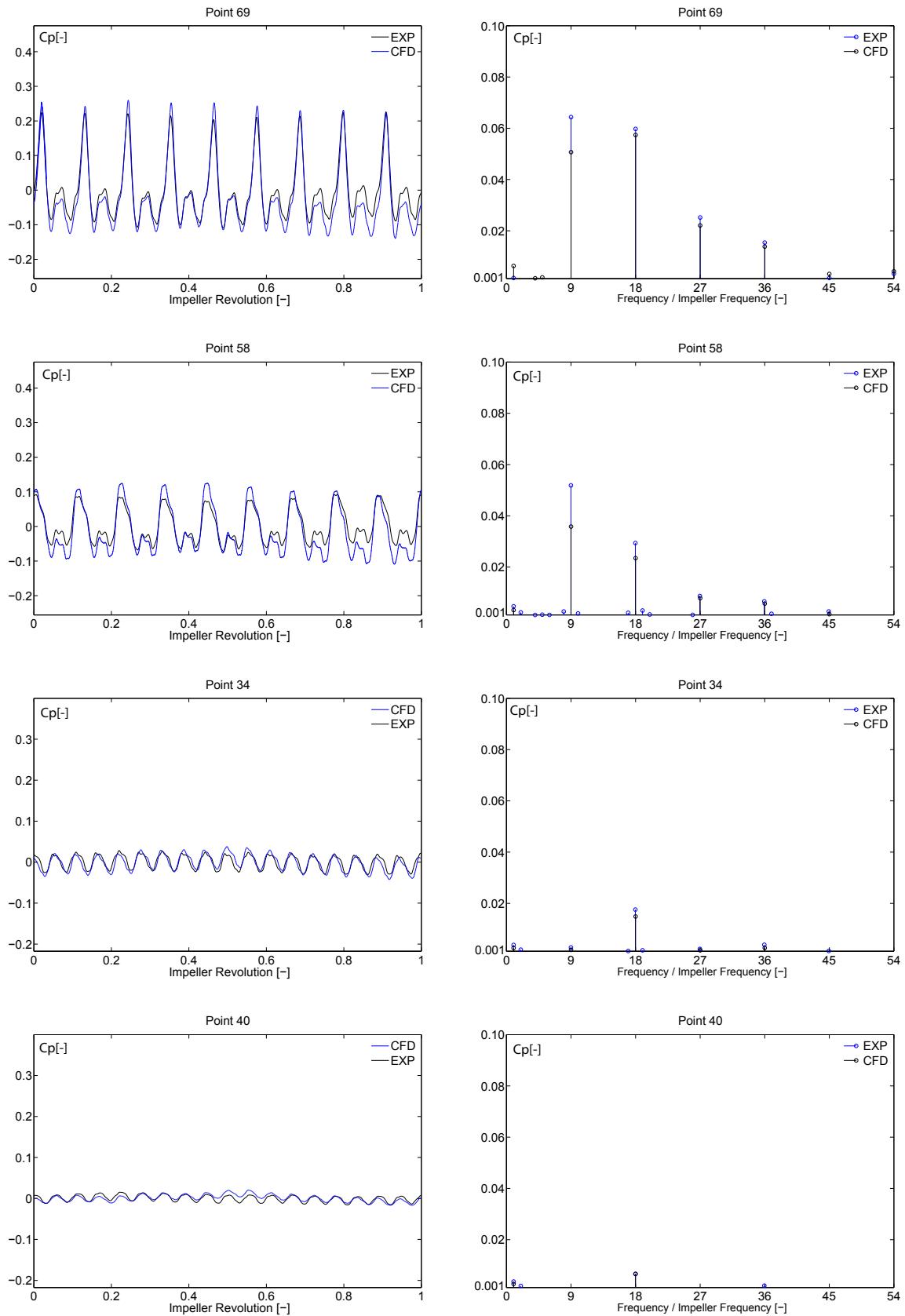


Figure 4.20: Full load operating point, OP III: Time history oscillations and spectral analysis of pressure coefficient in a distributor channel, numerical and experimental results

### 4.3.3 Pressure Fluctuations in the Impeller

Pressure fluctuations resulting from numerical simulations in the impeller are compared with the corresponding measurements. Figure 4.21 represents the time history of the pressure fluctuations at the part load operating point, OP I. These results are evaluated at the monitoring points  $b1$  to  $b4$ , located on the pressure side of a rotating blade. The numerical pressure amplitude corresponding to the frequency is well predicted on the impeller. The frequency spectra of the pressure fluctuations indicate the peaks of  $z_o f_n$  as well as the spiral casing tongue effect at the frequency of impeller revolution. The pressure amplitude at the mentioned frequency has the maximum value at the leading edge where the impact of the stagnated flow is higher than the monitoring points located along the blade,  $b2$  to  $b4$ .

Figure 4.22 represents the time history and frequency spectra of pressure fluctuations at the suction side. The comparison presents a consistency between the experimental and numerical results, however the pressure pulsation due to the closing part of the spiral casing is not well predicted by the numerical simulations. Pressure amplitude corresponding to the blade passing frequency  $f = z_o \cdot f_n$  at both suction and pressure sides of an impeller blade, monitoring points  $b1$  to  $b11$ , are represented in Figure 4.23.

At the operating point OP II, the pressure fluctuations as well as spectral analysis are compared, see Figure 4.24. The frequency spectra indicate the effect of closing part of spiral casing which is called tongue effect. This effect is distinguished with the high pressure amplitude at the impeller blade passing frequency. Regarding to the pressure fluctuation in time at the monitoring point  $b1$ , it is observed that they are not fully periodic at each impeller blade passage. It could be explained by a signal modulation between the blade passing frequency and its harmonics with the tongue effect. Moreover, any slightly different positioning at the leading edge, where there is a strong pressure gradient can produce an important discrepancy for the comparison. The pressure pulsations at the suction side are represented in Figure 4.25 as well as pressure amplitude at guide vane passing frequency at all eleven monitoring points. The same tendency for the peaks of  $z_o f_n$  and tongue effect are observed in Figure 4.27, which represents the pressure fluctuations at full load operating point, OP III. However the measurement indicates a high pressure amplitude at the frequency  $f = 3 \cdot z_o f_n$  which does not appear in the numerical simulations. This tendency becomes more powerful towards the trailing edge of the impeller blades. These higher harmonics appear just at the full load conditions. The frequency spectra at the leading edge of the impeller blade, monitoring point  $b1$  and  $b7$ , show many sidebands between the frequency  $f_n$  and  $z_o f_n$ .

Accordingly, using the  $k - \varepsilon$  turbulence model with the relevant medium mesh and small time step gives a good consistency between numerical and experimental results in both stator and impeller domains.

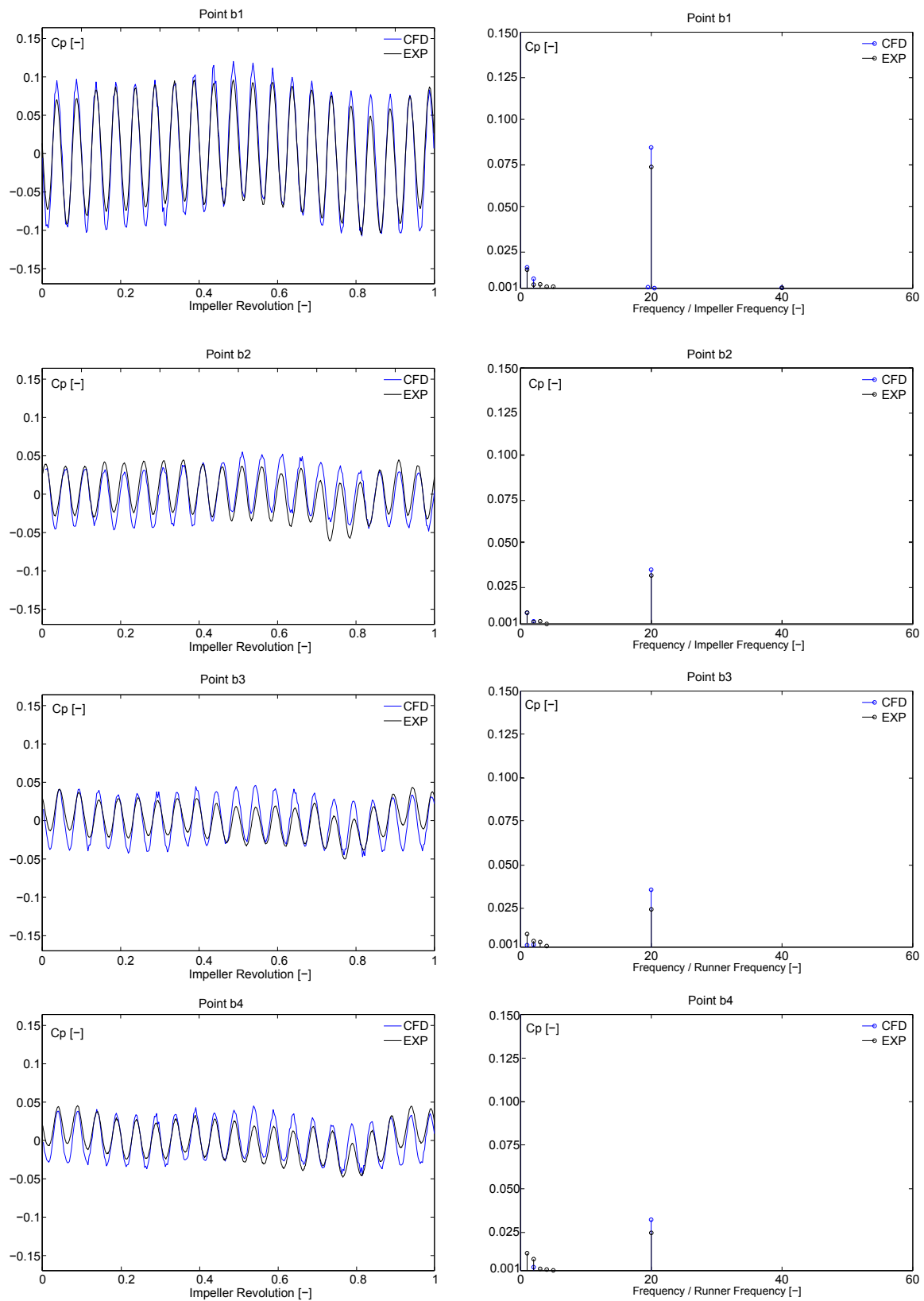


Figure 4.21: Part load operating point, OP I: Time history oscillations and spectral analysis of pressure coefficient, comparison between numerical and experimental results at the pressure side of an impeller blade

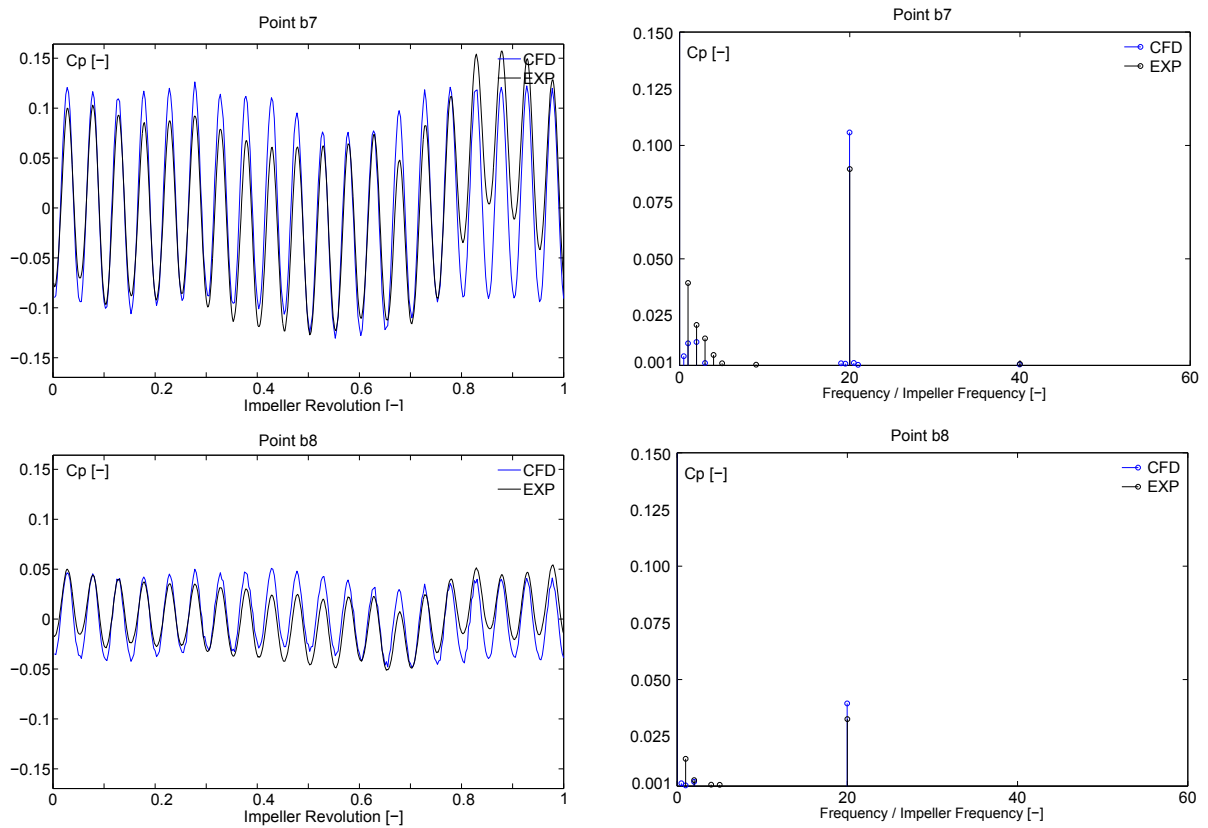


Figure 4.22: Part load operating point, OP I: Time history oscillations and spectral analysis of pressure coefficient, comparison between numerical and experimental results at the suction side of an impeller blade

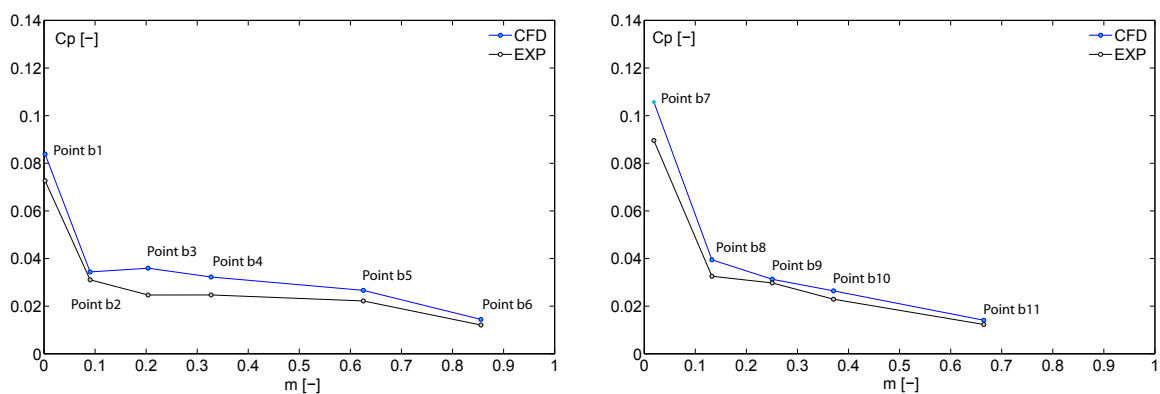


Figure 4.23: Part load operating point, OP I: Pressure amplitude corresponding to the frequency  $f = z_o \cdot f_n$  at the pressure side of an impeller blade, monitoring points  $b1$  to  $b6$  (left) and suction side, monitoring points  $b7$  to  $b11$  (right)

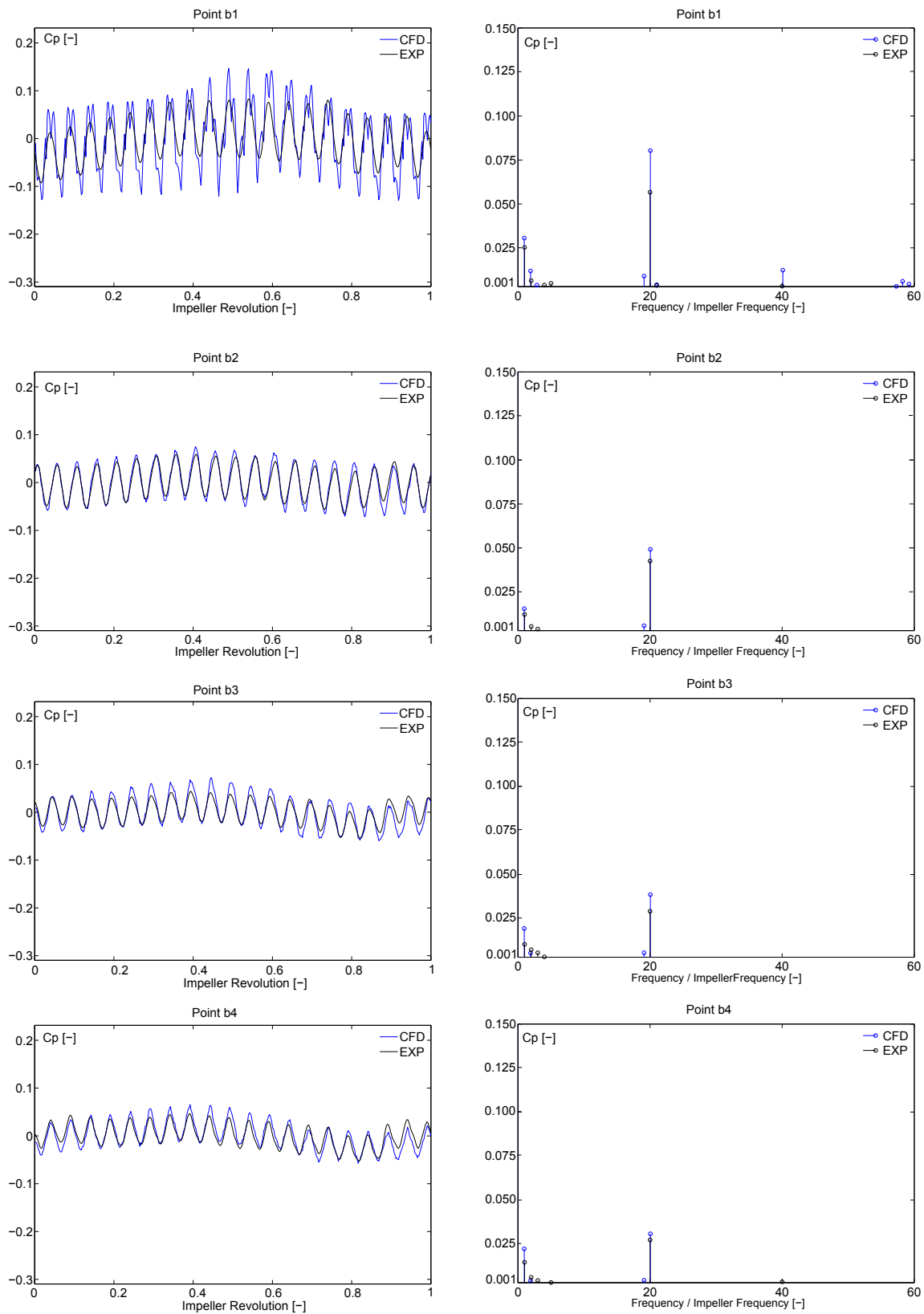


Figure 4.24: Best efficiency operating point, OP II: Time history oscillations and spectral analysis of pressure coefficient, comparison between numerical and experimental results at the pressure side of an impeller blade

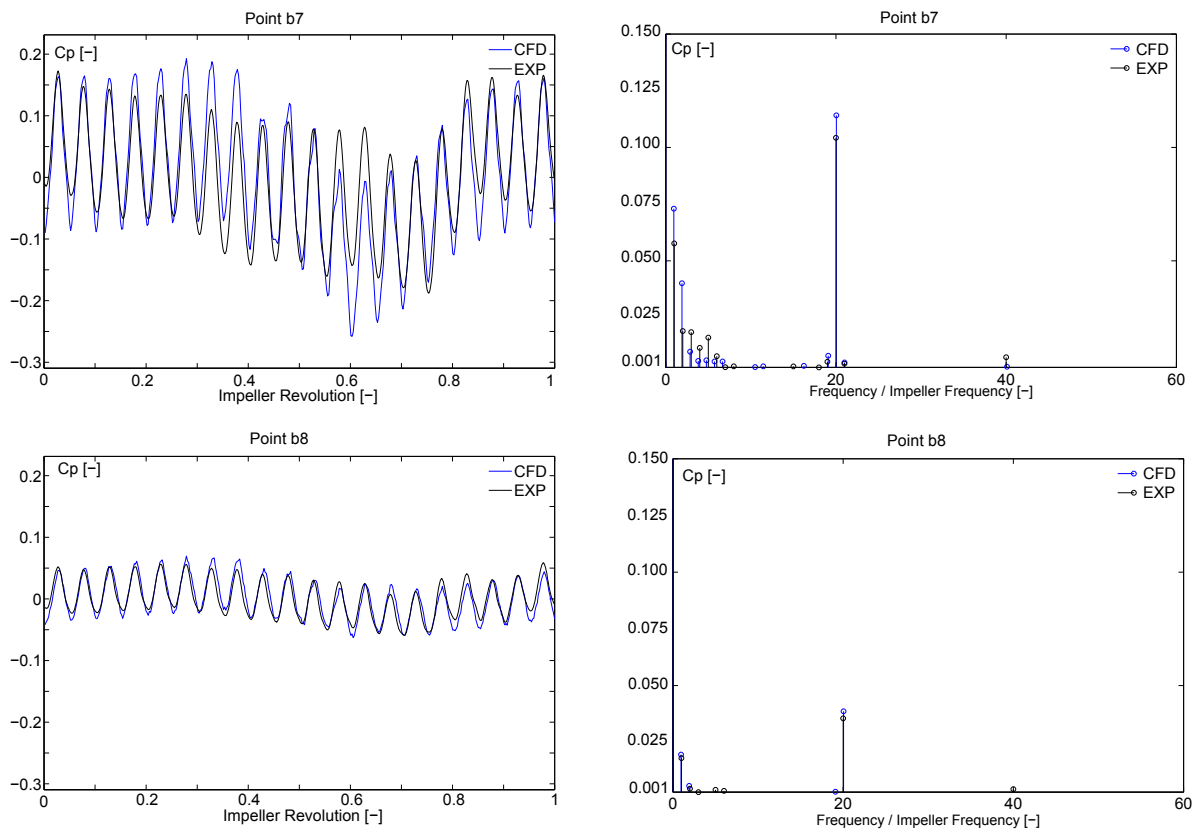


Figure 4.25: Best efficiency operating point, OP II: Time history oscillations and spectral analysis of pressure coefficient, comparison between numerical and experimental results at the suction side of an impeller blade

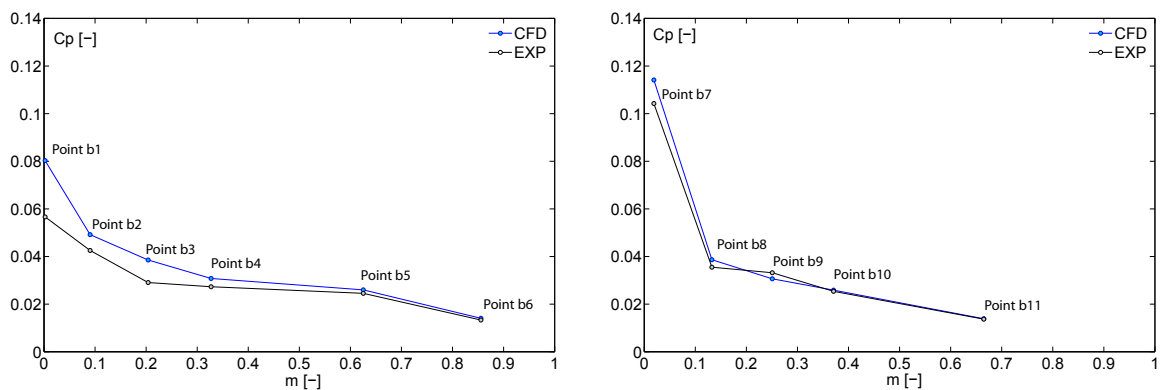


Figure 4.26: Best efficiency operating point, OP II: Pressure amplitude corresponding to the frequency  $f = z_o \cdot f_n$  at the pressure side of an impeller blade, monitoring points  $b1$  to  $b6$  (left) and suction side, monitoring points  $b7$  to  $b11$  (right)

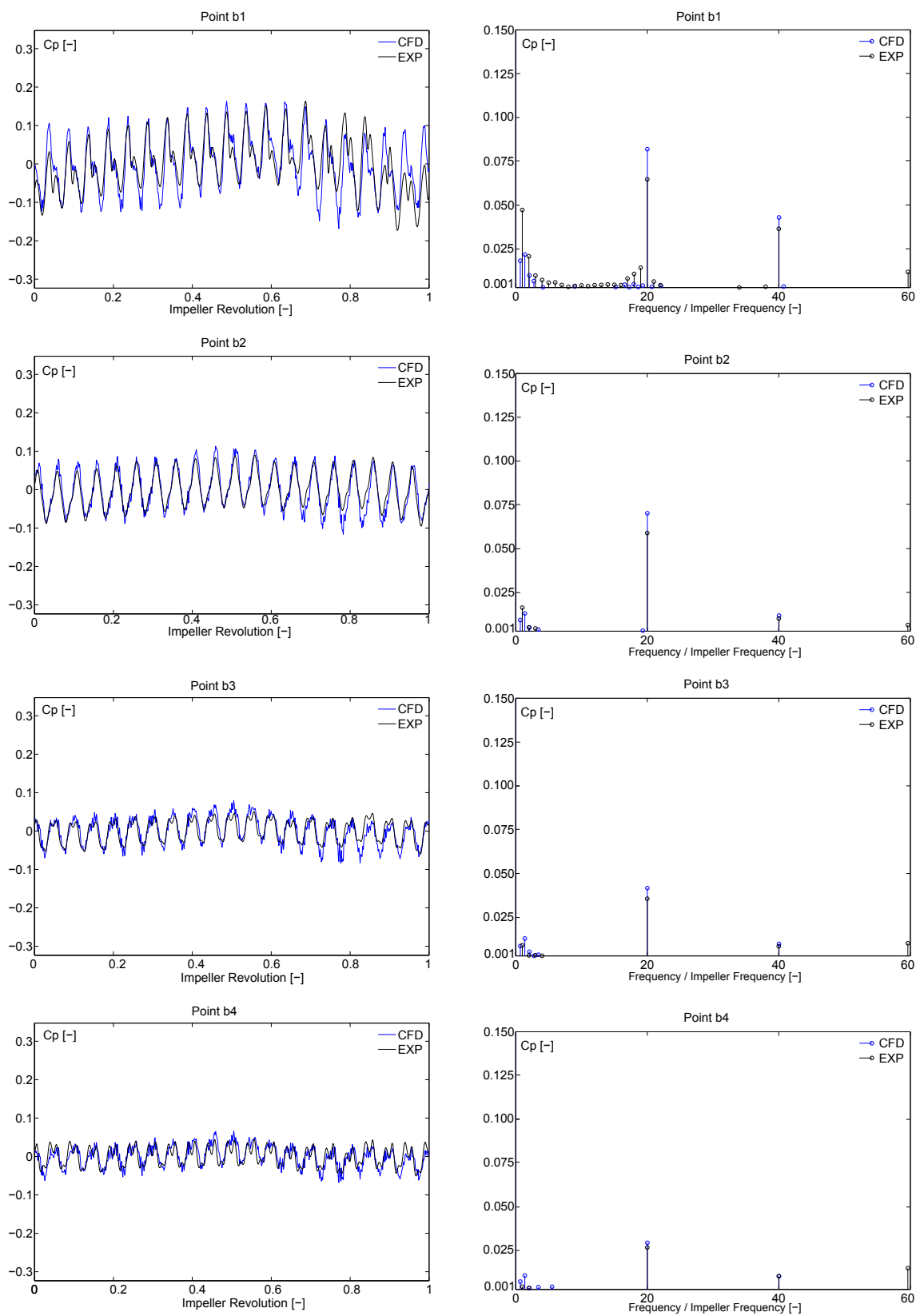


Figure 4.27: Full load operating point, OP III: Time history oscillations and spectral analysis of pressure coefficient, comparison between numerical and experimental results at the pressure side of an impeller blade

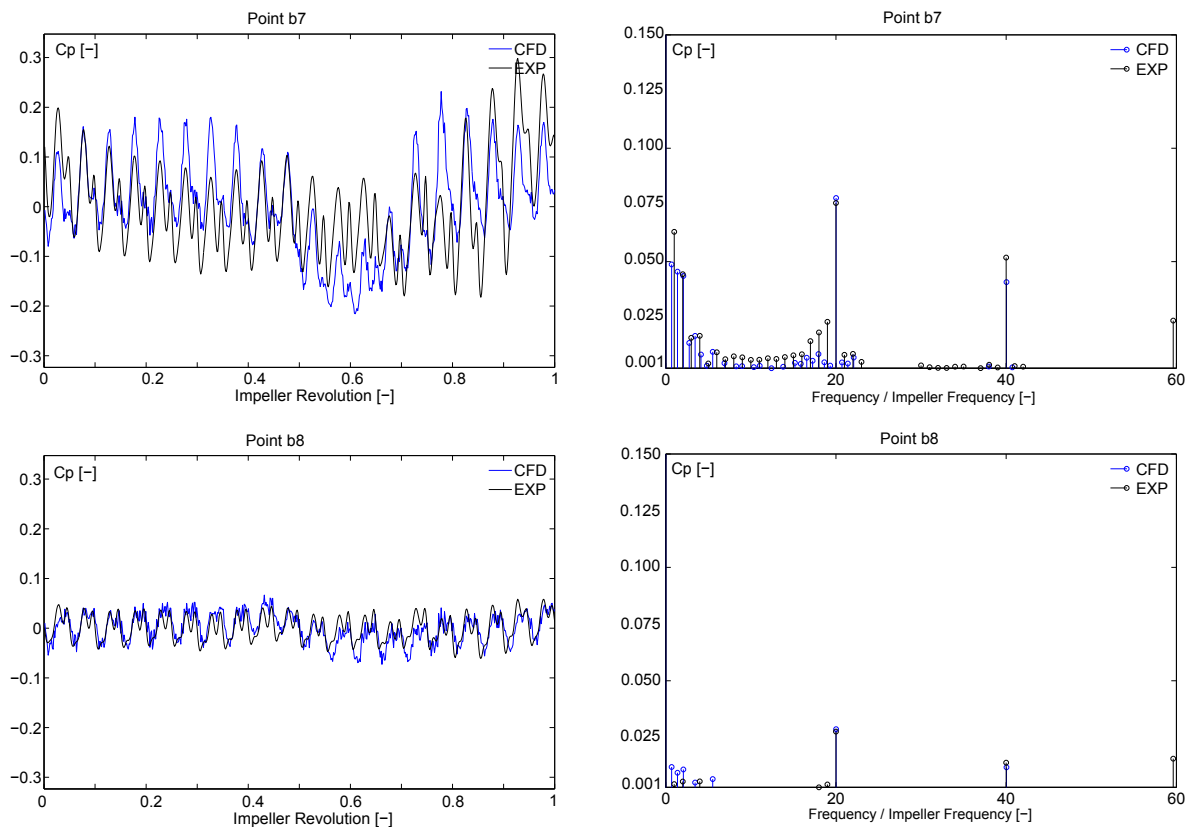


Figure 4.28: Full load operating point, OP III: Time history oscillations and spectral analysis of pressure coefficient, comparison between numerical and experimental results at the pressure side of an impeller blade

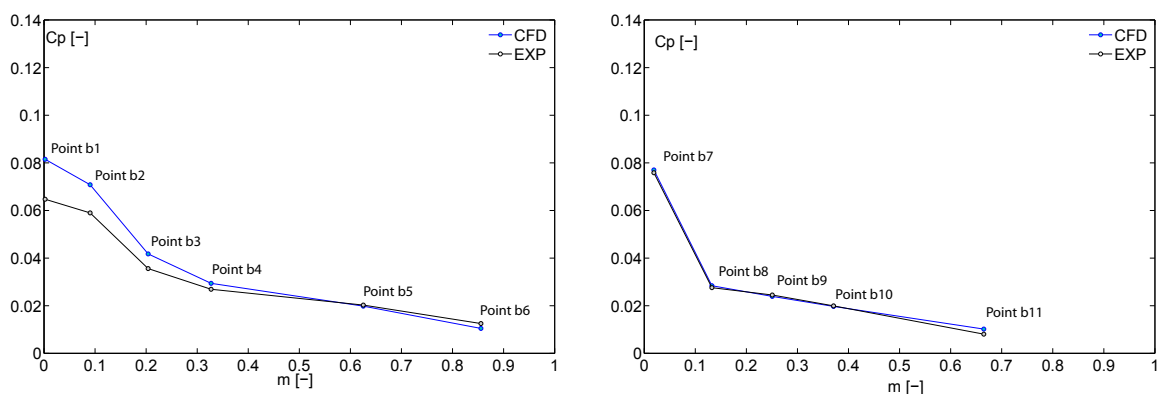


Figure 4.29: Full load operating point, OP III: Pressure amplitude corresponding to the frequency  $f = z_o \cdot f_n$  at the pressure side of an impeller blade, monitoring points  $b1$  to  $b6$  (left) and suction side, monitoring points  $b7$  to  $b11$  (right)



# Chapter 5

## RSI Physical Analysis

### 5.1 Pressure Propagation in the Stationary Domain

Any pressure perturbation in a hydro turbine is propagated in all directions. With respect to the compressible or incompressible flow characteristics, two mechanisms for pressure propagation are determined. The first one is propagation of hydroacoustic waves in whole installation and the second mechanism is potential flow advection based on the pressure gradient field. In the absence of hydroacoustic aspects in the numerical simulation, the pressure advection due to RSI is investigated. In the stationary part of the turbine, this pressure advection could be analyzed in two parts. In the angular direction, where it creates diametrical modes and in the radial direction that shows the evaluation of the pressure perturbation due to RSI from vaneless gap through a distributor channel to spiral casing.

#### 5.1.1 Angular Pressure Advection

The analysis of pressure advection in the angular direction is performed to identify the diametrical modes at the periphery of distributor channels. The amplitude of the mentioned rotating mode is relatively strong in the vaneless gap; however, it decreases toward the spiral casing. In the spiral casing, this rotating mode converts to the standing modes with weak pressure amplitudes. The number of the guide vanes and impeller blades are the key issues to identify the diametrical modes.

In this section, the angular advection of pressure in the stationary domain is investigated at three circular sections,  $R1$ ,  $R2$  and  $R3$ . At each section, 20 monitoring points with equal angular intervals are considered, see Figure5.1. The first section,  $R1$ , is selected in the vaneless gap between guide vanes and impeller blades, where the most powerful pressure fluctuations occur due to RSI. The second one,  $R2$ , is considered at the radius corresponding to the gap between guide vanes and stay vanes. Finally, section  $R3$  is defined at the entrance of the stay vanes. The monitoring points at each radius are located such as to have one in each distributor channel.

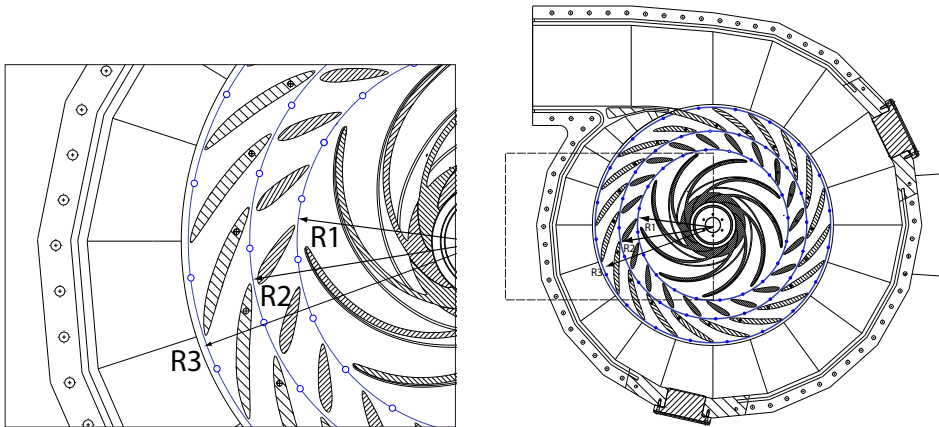


Figure 5.1: Monitoring points at sections  $R1$ ,  $R2$  and  $R3$  in the stationary part.

### Pressure Fluctuations in the Vaneless Gap, $R1$ (Diametrical mode)

An unsteady pressure fluctuation field in the vaneless gap is induced by the periodic perturbation due to the rotating blades. With regards to the instantaneous pressure values at the periphery of the vaneless gap,  $R1$ , an elongated shape with two high and two low pressure zones are identified, see Figure 5.2. It occurs while, the leading edge of the rotating blades pass in front of the distributor channels. In such a motion, the pressure value increases in the semi blocked guide vane channel. The pitch angle between the guide vane and impeller channels is the cause of a phase shift of pressure peak in the distributor channels. With respect to the time history of pressure fluctuation at a monitoring point, for example  $R1.11$ , the passage of the pressure peaks is clearly distinguished.

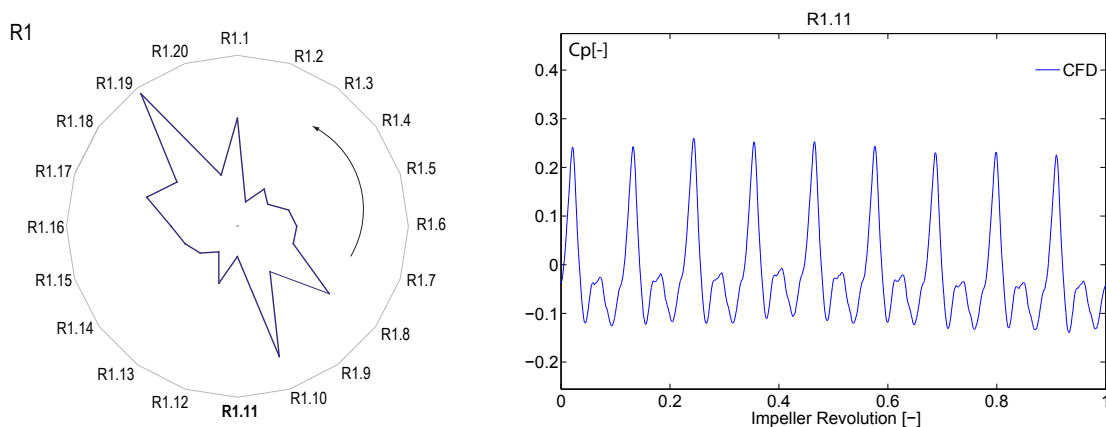


Figure 5.2: Full load operating point, OP III: (left) instantaneous pressure values at the periphery of the vaneless gap, section  $R1$ , and (right) time history oscillations at monitoring point  $R1.11$

Figure 5.3 represents the pattern of pressure fluctuations at the periphery of the vaneless gap in time at circular section  $R1$ . The angular position indicates the location of the monitoring points at the periphery. Time axis is normalized by the impeller blade passage, period over impeller blade number. The black lines illustrate the angular traveling passage of the pressure peaks in time that corresponds to the impeller blade passage.

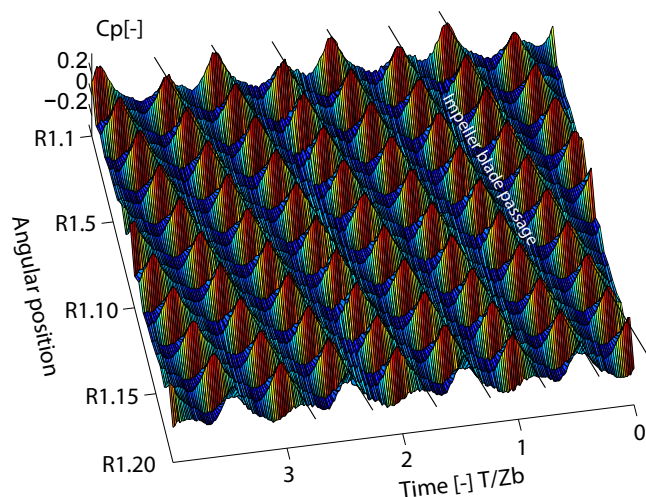


Figure 5.3: Full load operating point, OP III: the pattern of pressure fluctuations at the periphery of the vaneless gap in time at circular section  $R1$ , monitoring points  $R1.1$  to  $R1.20$

Three sequential pattern of pressure field at section  $R1$  are represented in Figure 5.4. The black stars indicate the positions of the pressure peaks. The rotational velocity of this pressure pattern is a function of the impeller blade number. In the present case, the pressure field rotates with the angular velocity corresponding to  $Cu = z_b\omega$ , in the opposite direction of impeller revolution. Two high and two low pressure zones determine the second order of diametrical mode,  $k=2$ . The angular revolution of impeller during two successive sequences is represented by  $\theta_b$ . In the same period the angular displacement of the pressure peaks is indicated by  $\theta_s$ . The revolution of impeller as  $4^\circ$ , corresponds to revolution of the elongated shape of pressure field as a couple guide vane passages,  $\theta_s = 36^\circ$  in the opposite angular direction, see Figure 5.4. Regard to the frequency spectra at section  $R1$  for the full load operating point, one observes the dominance of the pressure amplitude at blade passing frequency and its first harmonic,  $f = 18f_n$ . Figure 5.5 represents the pressure amplitudes and related phase values at the refereed frequencies at the monitoring points  $R1.1$  to  $R1.20$ . Accordingly, the phase shift between two monitoring points with the interval of  $18^\circ$  is constant and equal to  $162^\circ$ .

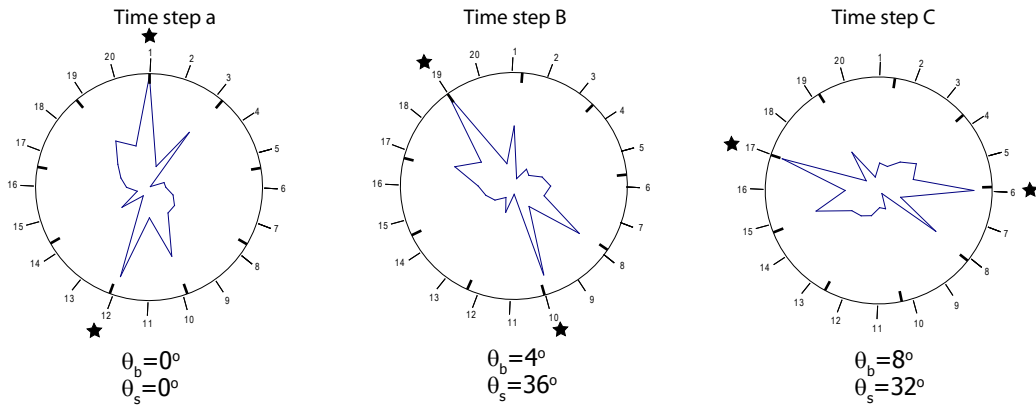


Figure 5.4: Full load operating point, OP III: three sequential pattern of instantaneous pressure values at the periphery of the vaneless gap,  $R1$ .

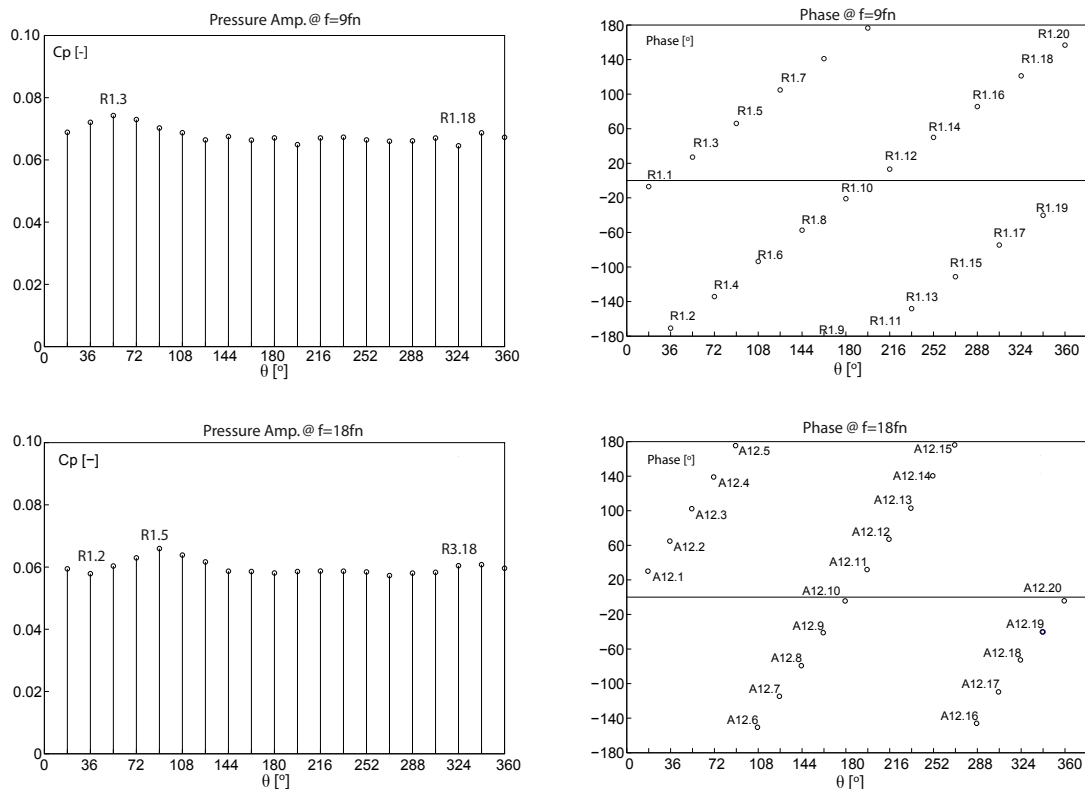


Figure 5.5: Full Load operating point, OP III: the pressure amplitude at blade passing frequency and  $f = 18 \cdot f_n$  (top-left and bottom-left) and corresponding phase values (top-right and bottom-right) at the monitoring points  $R1.1$  to  $R1.20$

Moreover, in case of vibration, the pressure fluctuations interact with the structure and generate hydroacoustic waves, which propagate in the installation. The order of the triggering of the pressure peaks as well as pressure amplitude are used for modeling the hydroacoustic effects [76].

### Pressure Fluctuations in the Stay vanes-Guide vanes Gap, R2 (Diametrical mode)

The simulated pressure fluctuations at the periphery of the gap between stay vanes and guide vanes, section *R2*, are represented in Figure 5.6. The form of the instantaneous pressure indicates the same tendency as observed at the periphery of the vaneless gap, section *R1*. However, the amplitude of pressure fluctuation is lower. The time history of pressure fluctuation at monitoring point *R2.11* is presented as well. Figure 5.7 illustrates the pattern of the pressure fluctuations at section *R2*. The high pressure zones rotate in time with a constant angular velocity. This motion pattern is conserved at the section *R2*. Figure 5.8 represents the pressure amplitude and related phase values at the mentioned frequencies at the monitoring points *R2.1* to *R2.20*. Accordingly, the phase shift between two monitoring points corresponds to the difference in angular position, which is equal to  $18^\circ$ . The values of the pressure amplitude at the mentioned section show a considerable variation at the frequency  $f = 18 \cdot f_n$ .

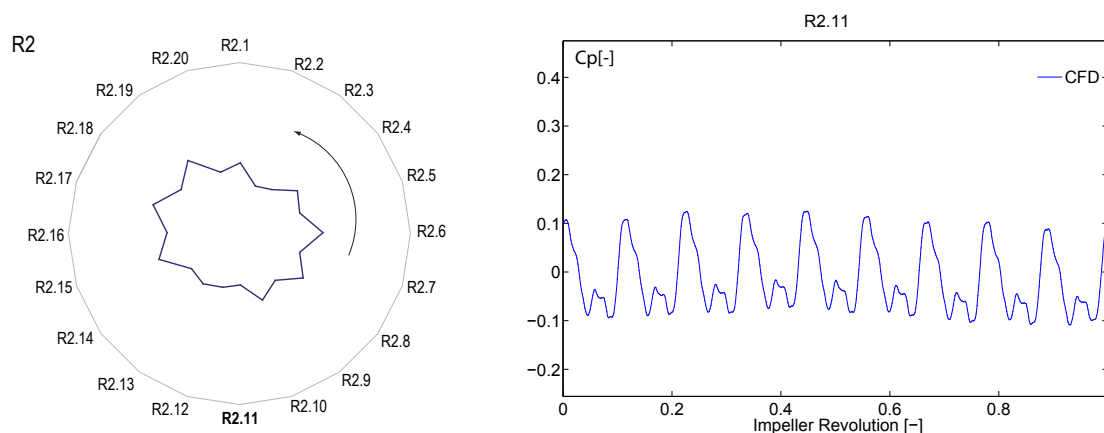


Figure 5.6: Full load operating point, OP III: (left) instantaneous pressure values at the periphery of the gap between guide vane and stay vane, section *R2*, and (right) time history oscillations at monitoring point *R2.11*.

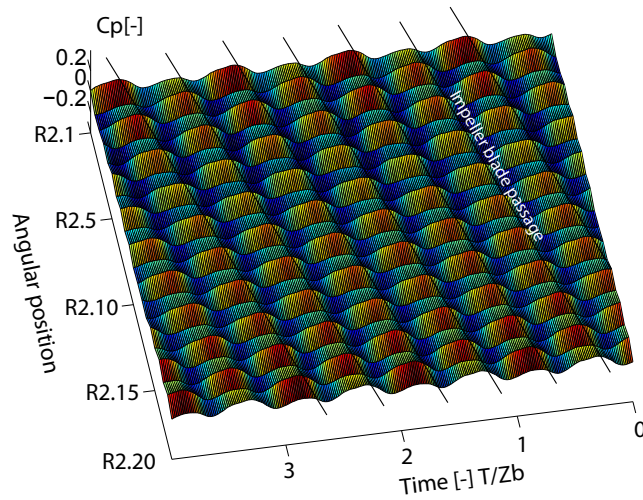


Figure 5.7: Full load operating point, OP III: the pattern of pressure fluctuations at the periphery of the gap between guide vane and stay vane, section  $R2$ , monitoring points  $R2.1$  to  $R2.20$ .

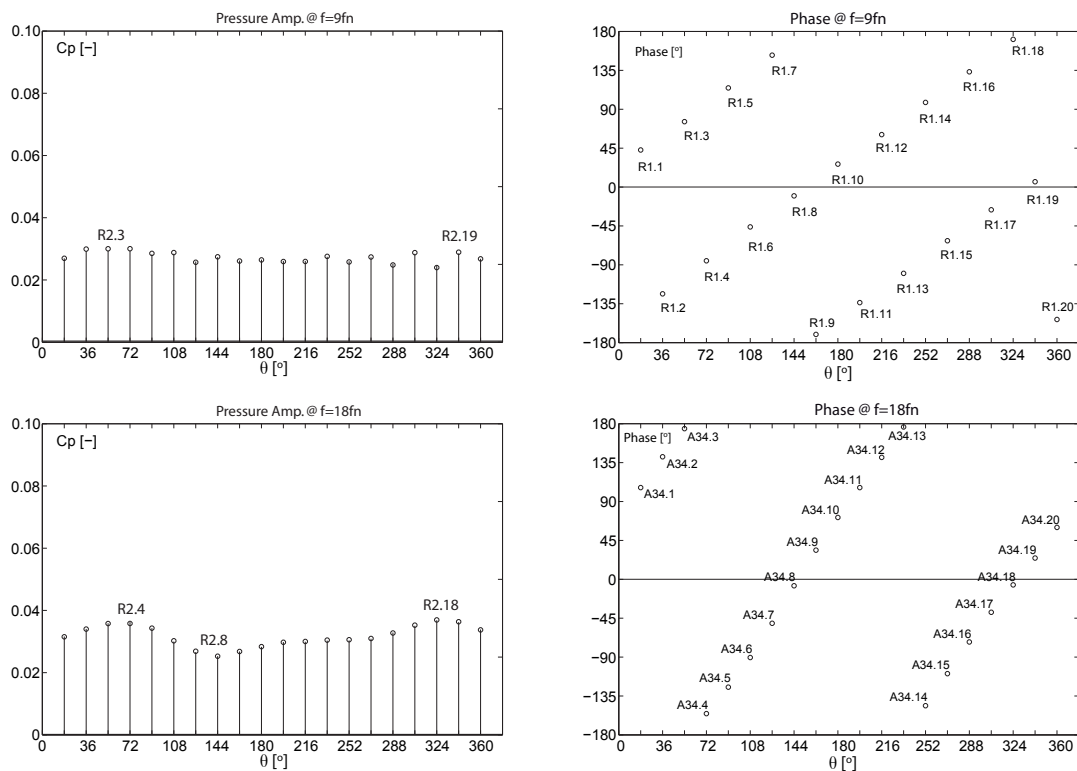


Figure 5.8: Full load operating point, OP III: (left) the pressure amplitude at blade passing frequency and  $f = 18 \cdot f_n$  and (right) corresponding phase values at the monitoring points  $R2.1$  to  $R2.20$

### Pressure Fluctuations in the Spiral Casing, R3 (Standing mode)

The pressure fluctuations in the spiral casing could be critical in the case of the resonance with the structure of the power plant. The characteristics of the flow pattern in the spiral casing are analyzed at the entrance of the stay vanes, see Figure 5.9. Accordingly, the pressure amplitude at frequency  $f = z_b f_n$  is very weak; however, the variation is considerable at the periphery. The highest pressure fluctuations occur in the spiral casing tongue. In contrast with the angular motion of the pressure field at sections  $R1$  and  $R2$ , the pressure field is quasi standing in the spiral casing.

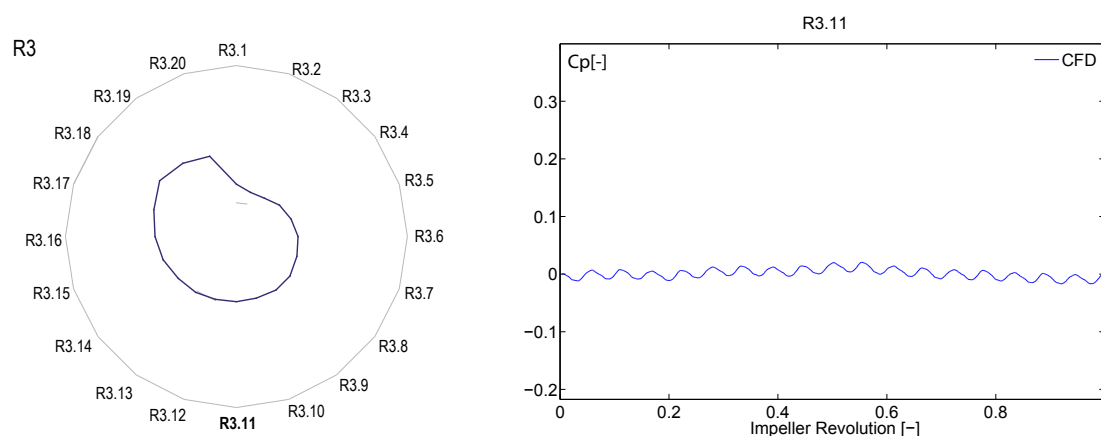


Figure 5.9: Full Load operating point, OP III: (left) instantaneous pressure values at the periphery of stay vane inlet, section  $R3$ , and (right) time history oscillations at monitoring point  $R3.11$

The pattern of the pressure fluctuations could be caused by the acoustic waves as well as viscous flow. In the numerical simulation of an incompressible flow, this flow pattern could be explained by the pressure advection. Regarding the map of pressure fluctuations in time and space at the entrance of the stay vanes, see Figure 5.10, one observes a significant change in the form of a high pressure zone traveling in section  $R1$  rather than the sections  $R2$  and  $R3$ . To better understand, the pressure amplitude and the phase corresponding to the 20 monitoring points,  $R3.1$  to  $R3.20$ , are indicated in Figure 5.11. The pressure amplitude shows a minimum value at monitoring point  $R3.12$ . According to the definition of the pressure coefficient the pressure fluctuation at the inlet is eliminated. Therefore, in the distributor channel close to the inlet of spiral casing this value is very low. Accordingly, the diametrical mode in the spiral casing rotates more slowly than sections  $R2$  and  $R3$ . Moreover, it is interrupted at the monitoring point  $R3.12$ . This effect could be due to the high pressure zone reflection at the walls of the spiral casing tongue.

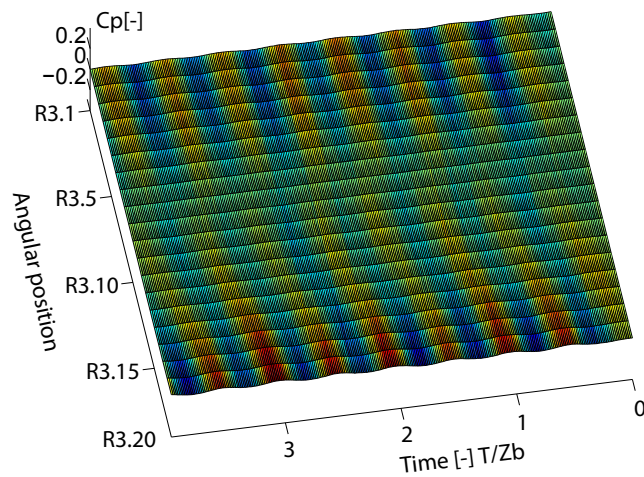


Figure 5.10: Full load operating point, OP III: the pattern of pressure fluctuations at the periphery of stay vane inlet in time at circular section  $R3$ , monitoring points  $R3.1$  to  $R3.20$

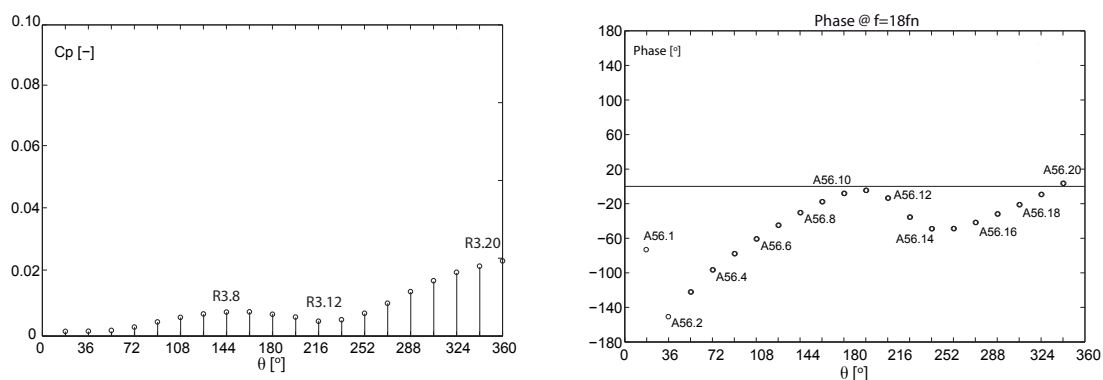


Figure 5.11: Full load operating point, OP III: (left) the pressure amplitude at blade passing frequency and  $f = 18 \cdot f_n$  and (right) corresponding phase values at the monitoring points  $R3.1$  to  $R3.20$



Figure 5.11 illustrates the pressure coefficient at the periphery of the spiral casing, monitoring points  $R3.1$  to  $R3.20$ , and corresponding phase values. Accordingly, the maximum pressure fluctuations appear in the tongue, monitoring point  $R3.20$  and a local peak is also distinguished at monitoring point  $R3.8$ , however at monitoring point  $R3.12$  a very low pressure amplitude is obtained. The corresponding phase values show a rotating pressure mode that pass half of the periphery, from  $\theta = 36^\circ$  to  $\theta = 180^\circ$ . In this part the high pressure zone rotates with a quasi constant angular velocity. The same tendency is obtained at the section between  $\theta = 252^\circ$  to  $\theta = 360^\circ$ . The phase evaluation between these two spatial sections shows a rotating pressure zone at the opposite angular direction. To understand the reason of a minimum pressure amplitude at monitoring point  $R3.8$ , the pressure field at the mid span of the spiral casing including the instantaneous pressure value at the section  $R3$  is illustrated while the monitoring point  $R3.8$  obtains the maximum pressure value, see Figure 5.12. The pressure value at the periphery of spiral casing,  $R3.1$  to  $R3.20$  at the related time step is also represented in the last mentioned figure. Accordingly, while the impeller blades pass to the monitoring points  $R3.8$  and  $R3.19$ , two pressure peaks are distinguished at the periphery, see the blue line. These two high pressure zones are placed in the channel 6, monitoring point  $R3.6$ , and the other one in channel 19, monitoring point  $R3.19$ . In this snap shot, the low pressure peak is observed at monitoring point  $R3.8$ , however this value is positive. By rotating the impeller blade to the position that is represented in Figure 5.13, the high pressure zones are installed in the channel 12 and 3. In spite of the fact that the pressure value at monitoring point  $R3.12$  is higher than the monitoring point  $R3.8$  and  $R3.20$ , it is lower than the instantaneous pressure value at the previous time step. The difference of pressure values at these two time steps represents the peak to peak pressure amplitude at each monitoring point. Figure 5.14 represents the pressure value at the periphery of spiral casing, monitoring points  $R3.1$  to  $R3.20$ , during one period of blade passage.

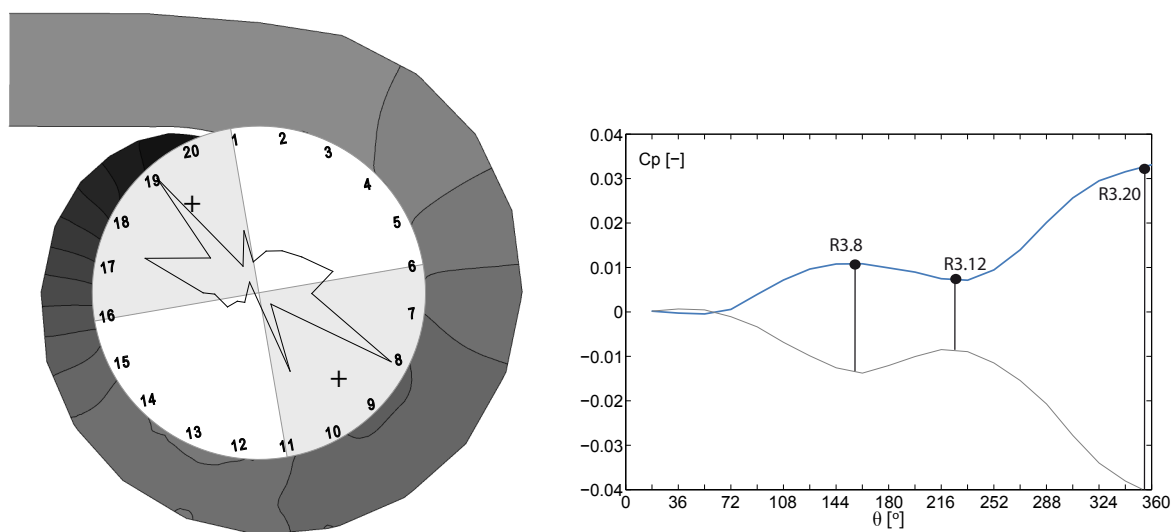


Figure 5.12: Left) Pressure field at the time step corresponding to the max. pressure value at  $R3.12$  at the mid horizontal section of the spiral casing, right) pressure value at the periphery of spiral casing,  $R3.1$  to  $R3.20$  at the same timestep

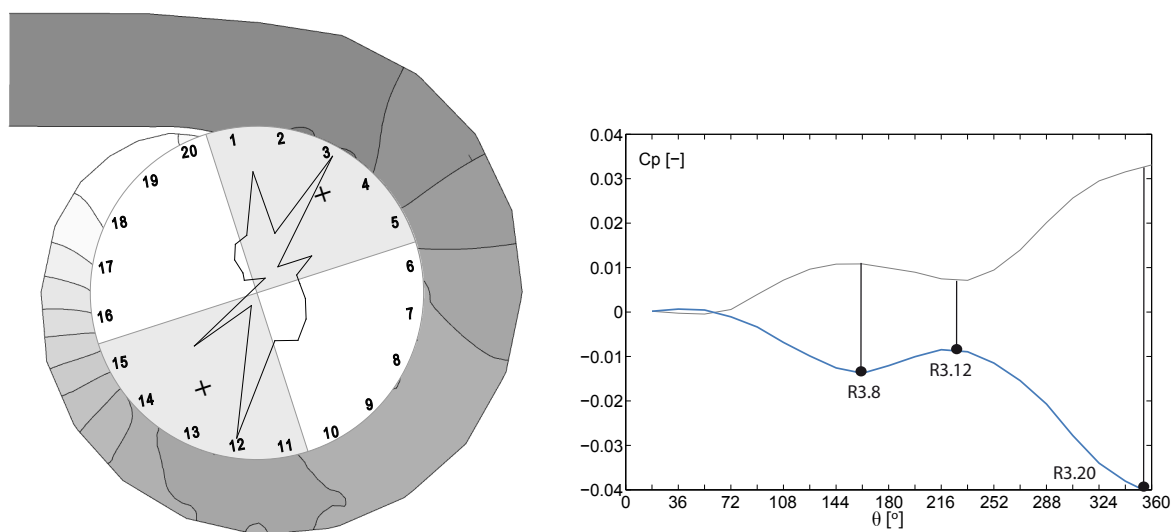


Figure 5.13: Left) Pressure field at the time step corresponding to the min. pressure value at  $R3.12$  at the mid horizontal section of the spiral casing, right) pressure value at the periphery of spiral casing,  $R3.1$  to  $R3.20$  at the same timestep

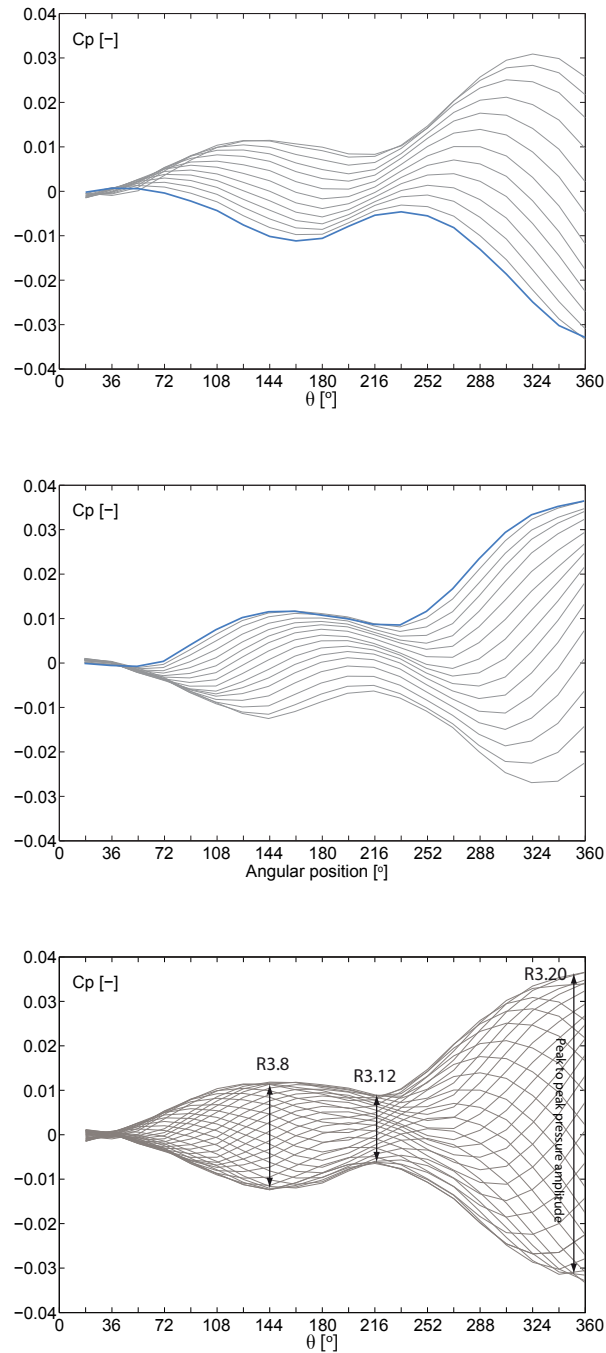


Figure 5.14: Represented pressure value as a curve at the periphery of spiral casing,  $R3.1$  to  $R3.20$ : Top) Pressure values at the periphery for half a period from Min. to Max. value at  $R3.12$ , Middle) Pressure values at the periphery for half a period from Max. to Min. value at  $R3.12$  and Bottom) Pressure values at the periphery for a period at  $R3.12$

### 5.1.2 Radial Advection of Pressure

The goal of this analysis is to explain how the pressure amplitude due to rotor-stator interactions rises and propagates in a distributor channel. The pressure fluctuations behaviors in different distributor channels are studied as well. Eight monitoring points are considered in 3 successive distributor channels. Figure 5.15.a shows the positions of these monitoring points. The corresponding pressure fluctuations during one impeller blade passage at all monitoring points are indicated in Figure 5.15.b. As it is shown, the first peak caused by blockage effect of rotating impeller blade damps progressively from point  $S2.1$ , located at the guide vane outlet, into the stay vane entrance at point  $S2.8$ . The pressure amplitude of the second peak also decreases from vaneless gap to spiral casing. The gap between stay vane and guide vane permits the high pressure zones to spread into the neighboring channels. That is why all of the points near the gap, point  $S2.3$  to  $S2.6$ , face the same pressure fluctuations.

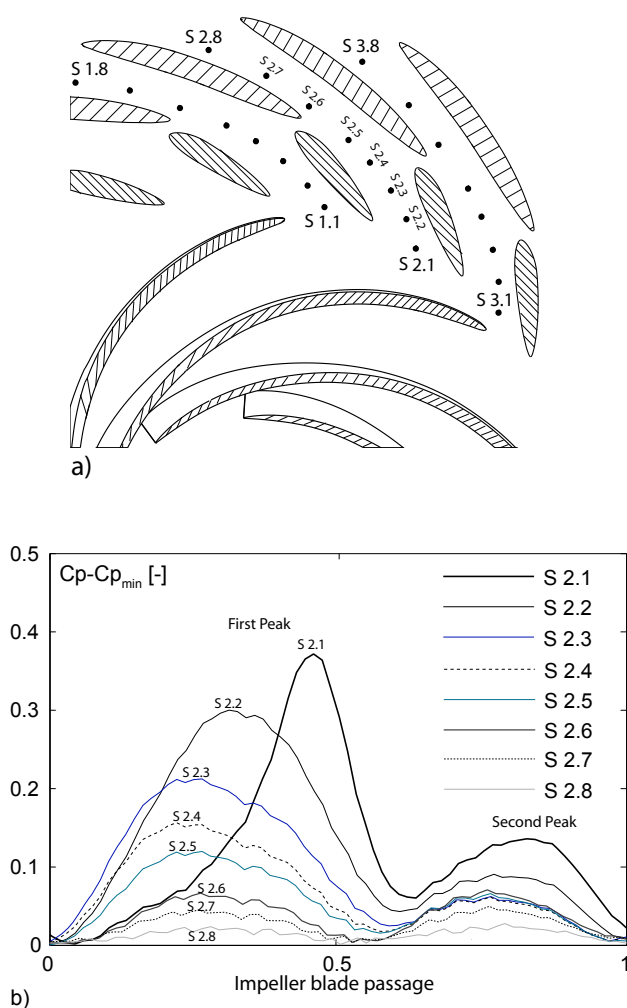


Figure 5.15: a) Positions of 8 monitoring points in three successive guide vane channels, b) Pressure fluctuations at 8 monitoring points during one impeller blade passage.

This effect is identified in Figure 5.16 as well. Pressure fluctuations for 3 successive guide vane channels during two impeller blade passages at the above mentioned monitoring points are illustrated in this figure. Figure 5.16 presents pressure fluctuations as a function of time at the monitoring points  $S1.2$ ,  $S2.2$  and  $S3.2$  placed in the guide vane channel. The time occurs of higher pressure peaks of point  $S2.2$  is asynchronous with the time occurs of lower pressure peaks the corresponding points in the neighboring channels, monitoring points  $S1.2$  and  $S3.2$ . This is true for all of the monitoring points in the guide vane channel. Accordingly the origin of local peak that occurs because of high pressure zone in the neighboring channels is confirmed. By passing from point  $S2.2$  to point  $S2.8$  trough the guide vane channel into the stay vane channel, the both above mentioned local peaks find the same patterns. The pressure amplitudes at the point  $S2.6$  to point  $S2.8$  placed in the stay vane channel are equivalent for both peaks and they are almost in phase, however pressure fluctuation is very weak. Thereby, it is the reason why in the spectral analysis second frequency mode appears as a dominant frequency. The pressure amplitude at the blade passage frequency damps very fast how in the gap between guide vane and stay vane.

Figure 5.17 shows the pressure fluctuations at point 69 during one impeller blade passage. The time steps  $a$ ,  $b$ ,  $c$  and  $d$  indicate the local minimum and local maximum values at the mentioned monitoring point. In order to better understand the origin of these peaks, pressure fields on the mid plane of the guide vane channels at the above-mentioned time steps are presented in Figure 5.17.a to Figure 5.17.d. The pressure coefficient values at point 69 at these time steps are noted on the legend bar. At time step  $a$ , corresponding to the minimum pressure fluctuation, the distributor flow channel is open and impeller blades are located along the wakes of guide vanes, see Figure 5.17.a. Thereby the flow passes freely and the pressure has its minimum value in the channel. By the impeller rotation, when the leading edge is placed in front of the channel, time step  $b$ , maximum pressure peak happens due to blockage effect, see Figure 5.17.b. The high pressure field spreads in the guide vane channel and the other monitoring points in this channel measure high pressure values. Time step  $c$  presents a local minimum pressure at monitoring point 69, because of the decreasing of blockage effect, see Figure 5.17.c. Time step  $d$  indicates the local peak while guide vane flow passage is open and impeller blades are located in front of the neighboring guide vane channels, see Figure 5.17.d. High pressure zone convects to the next channel through the gap between stay vane and guide vane and rotor-stator zone in order to have equilibrium pressure. This issue is sketched in Figure 5.18.

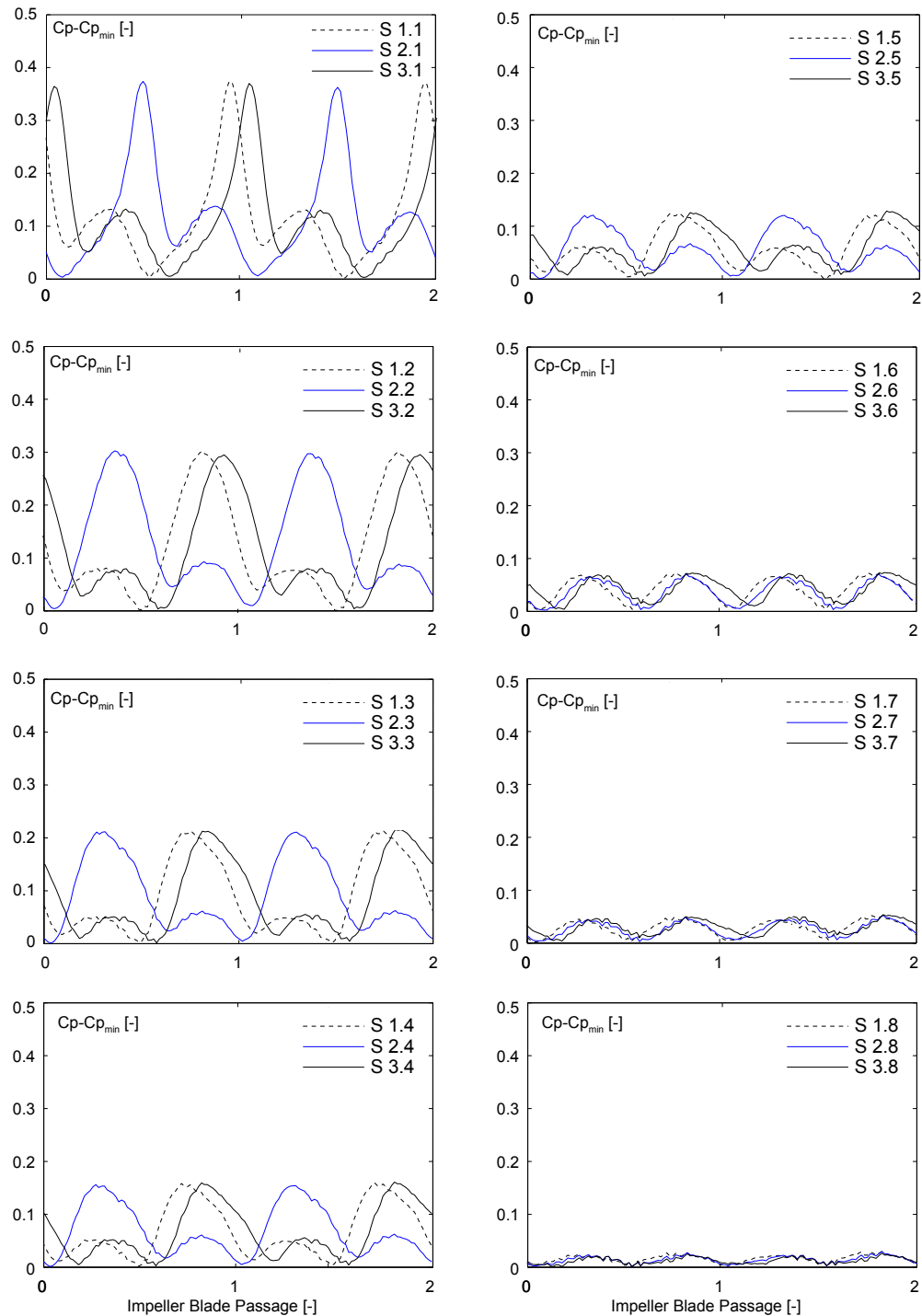
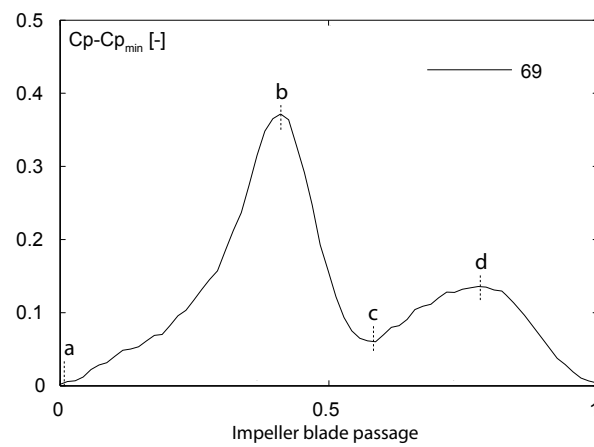


Figure 5.16: Pressure fluctuations at the 8 monitoring point for three successive guide vane channel during two impeller blade passage



Pressure fluctuations at point 69 during one impeller blade passage

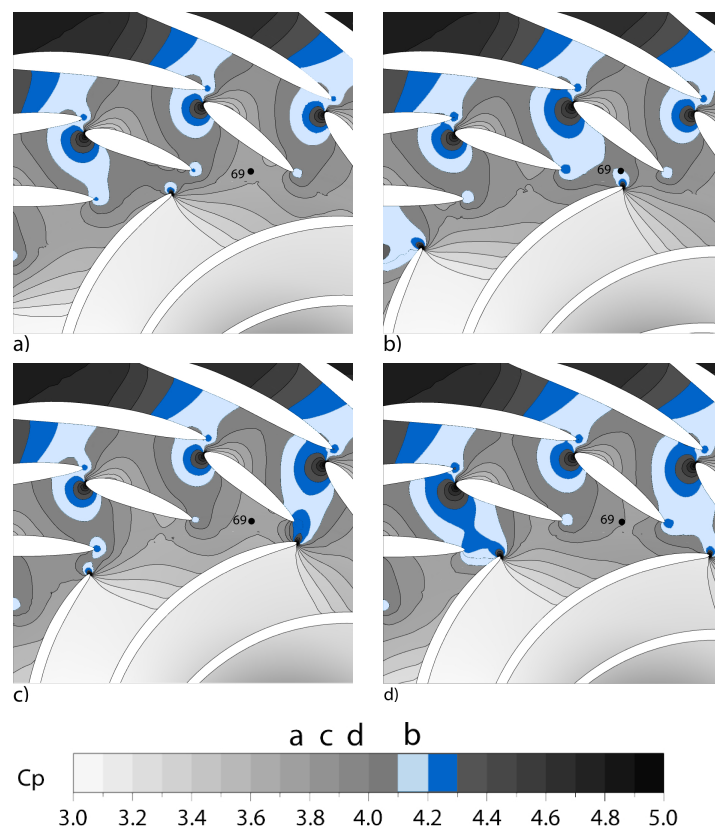


Figure 5.17: Pressure field on the mid plane of guide vane channels at the time steps corresponding to the local maximum and minimum pressure fluctuations: a) minimum pressure, b) maximum pressure value, c) local minimum and d) local peak value at point 69

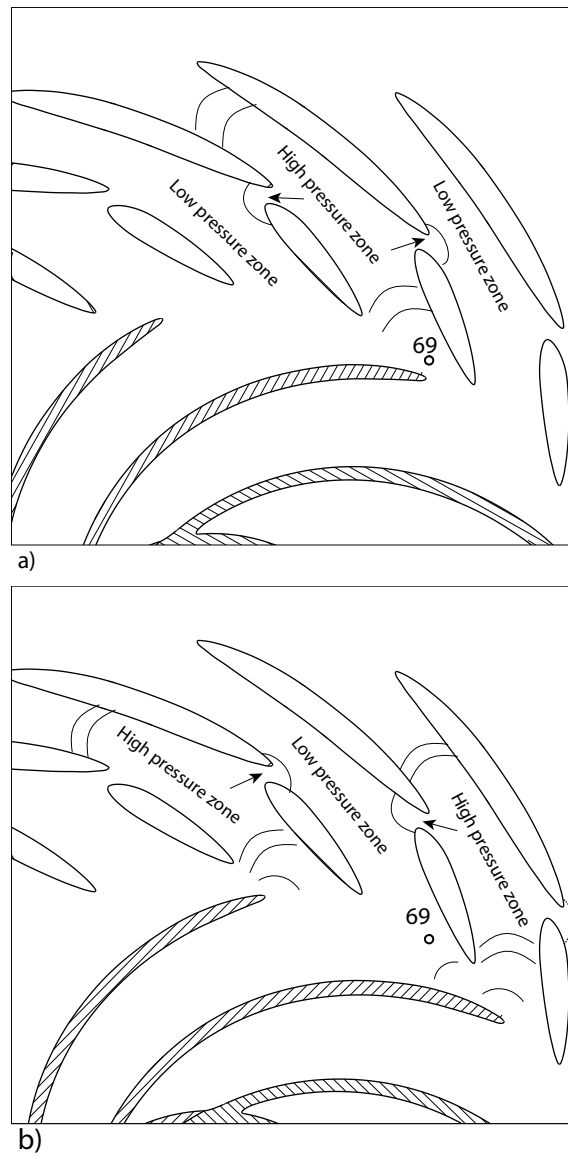


Figure 5.18: Pressure field on the mid plane in the guide vane channel



## 5.2 Pressure Fluctuations in the Impeller

Pressure fluctuations due to RSI could excite the impeller blades and might be at the origin of vibration. While the rotating blades pass periodically through the guide vane channels, the pressure perturbation possesses the frequency  $f = z_o f_n$  in the rotating frame. The large pressure amplitudes at the above-mentioned frequency could make serious damage to hydraulic power plant. To prevent a very strong pressure oscillation, turbines are designed in a way to have no common denominator between the number of guide vanes,  $z_o$ , and impeller blades,  $z_b$ . It helps to stagger the impact of the pressure shocks induced by RSI in successive impeller channels.

According to the literature, the most high pressure fluctuations could arise on the hub and shroud parts of the impeller and the region close to the vaneless gap. Consequently, the stress concentrations are focalized at the blade roots where they connect to the hub and shroud, see Figure 5.19 [96].

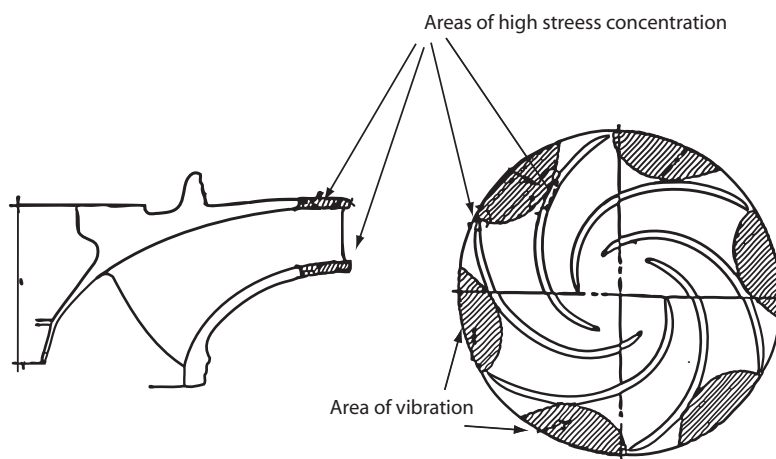


Figure 5.19: The most sensitive areas in the impeller to the RSI effects ,  $z_b = 7$ . [96]

In the present work, the fluctuations of the pressure field at both pressure and suction sides of the impeller blades are investigated. This issue is analyzed at three operating points from part load to full load operating points, OP I to OP III. Moreover, a detailed analysis is performed at the full load operating point, where the most considerable effects are detected. The pressure amplitudes corresponding to the dominant frequencies as well as the effect of phase shift of the pressure peaks in the impeller are studied. The leading edge of the impeller blade is the region that receives a highest pressure fluctuation in the impeller. The difference between the instantaneous pressures at both sides of the impeller blade determines the exerted oscillating force. The blade roots at the leading edge are the regions with the most high stress concentrations.

### Pressure Fluctuation in the Impeller at Full Load Operating Point

The pressure fluctuation at full load operating point is analyzed at the impeller walls. The pressure fluctuation resulting from numerical simulations at the leading edge of an impeller blade is represented in Figure 5.20. In order to have a global vision on the periodic pressure perturbation on the structure, the pressure amplitude corresponding to the guide vane passing frequency,  $f = 20f_n$ , and its harmonics are represented on the solid walls of the impeller, see Figure 5.21. With respect to the pressure amplitude field, three high pressure amplitude zones are observed on the pressure side of the impeller blades. The leading edge, A1, is where the coming flow from the guide vane stagnates. This region detects the maximum pressure fluctuations. The second zone, A2, is located very close to the leading edge, which corresponds to the trace of wake shed at the guide vane trailing edge. The third area, A3, is located at 1/3 of the pitch chord length from the inlet. The perturbation at the last mentioned region is much lower than the regions A1 and A2. The main reason of pressure oscillation at the region A3 is the interaction of high pressure zone coming back from the stator channels to impeller.

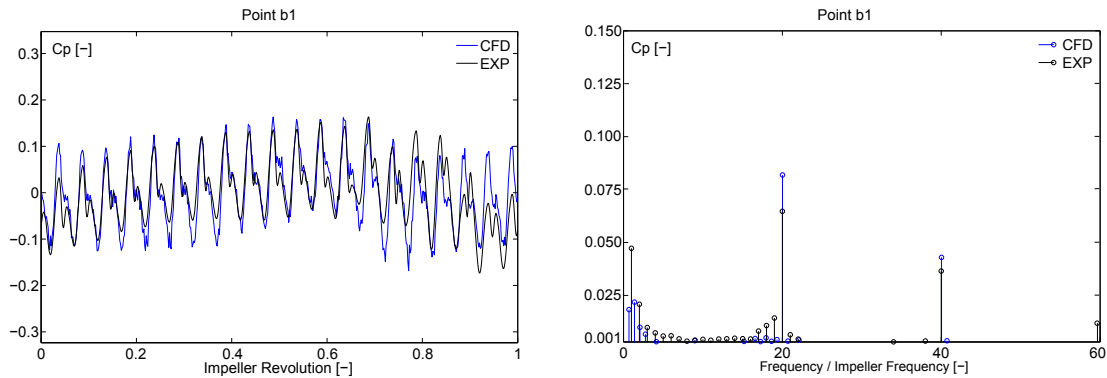


Figure 5.20: Full load operating point, OP III: Time history oscillations and spectral analysis of pressure coefficient at the leading edge of an impeller blade, b1

Figure 5.22 represents the pressure amplitude at the frequency  $f = 20f_n$  on the impeller blade as well as on the shroud. These three regions, A1 to A3, are distinguished on the impeller blade. Accordingly, a pressure fluctuation variation can be observed at the leading edge. At the roots of a blade, where they connect to hub and shroud, the perturbations are more considerable than mid span. At the region close to the leading edge, A2, a high pressure zone is detected. It is induced by the impact of rotor-stator blockage effect in the guide vane. The pressure field on the pressure side of the impeller gradually decreases toward the impeller outlet. However, the traces of guide vane wakes mark low pressure amplitude on the blade. Figure 5.23 represents the pressure amplitude at the frequency  $f = 40f_n$ . At the blade roots of the leading edge a high pressure amplitude at the mentioned frequency is observed. This effect might be at the origin of fatigue and even blade cracks. According to this figure, the high pressure amplitude is only observed at the leading edge and zone A2. The same tendency is detected for the pressure amplitude corresponding to the harmonic  $f = 60f_n$ , see Figure 5.24.

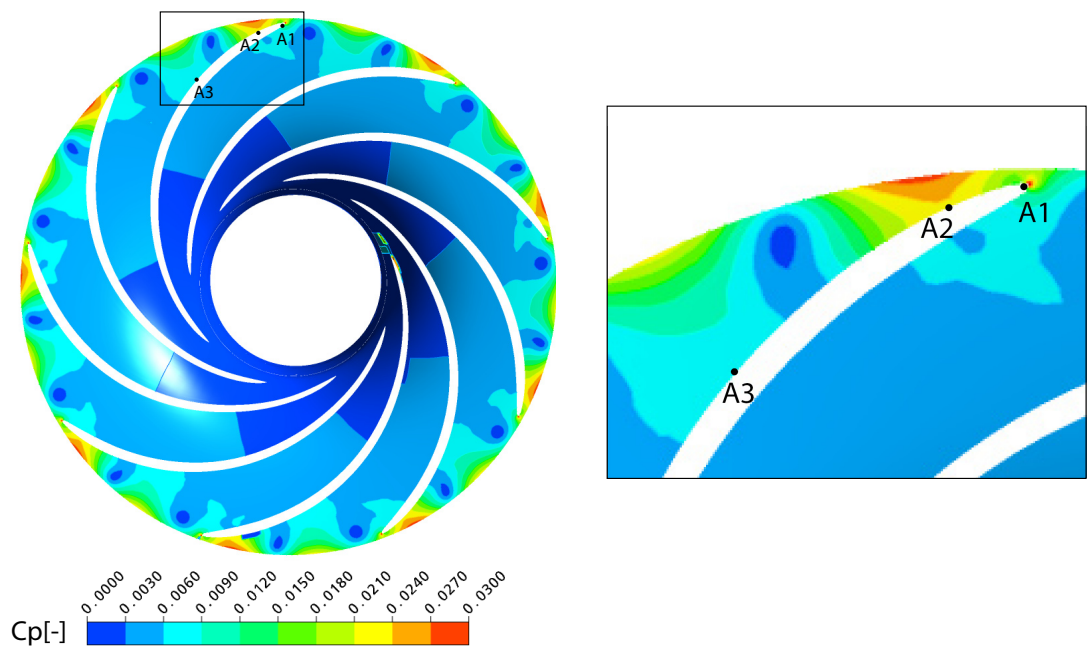


Figure 5.21: Pressure amplitude corresponding to the frequency  $f = 20f_n$  at the full load operating point, OP III, at mid span plane of the impeller.

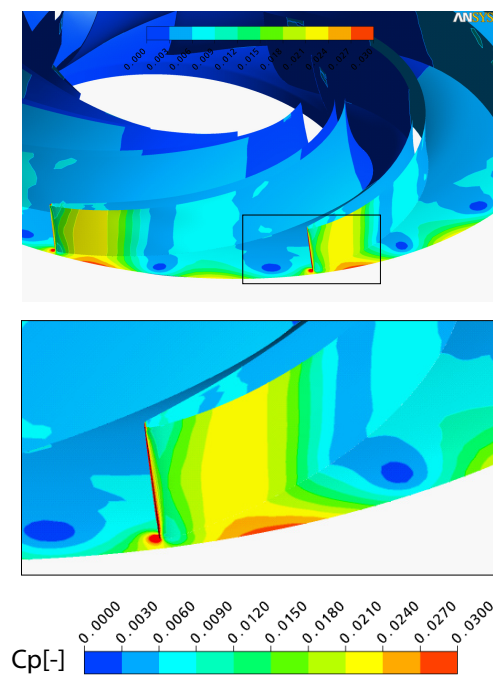


Figure 5.22: Pressure amplitude corresponding to the frequency  $f = 20f_n$  at the full load operating point, OP III, on the impeller blade as well as in the shroud.

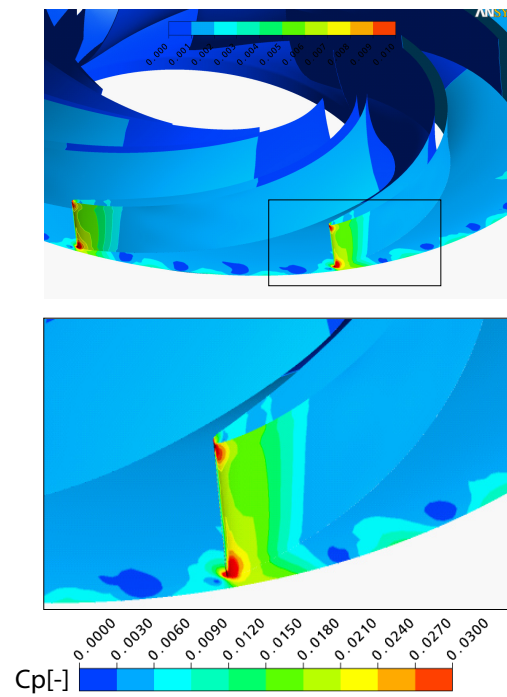


Figure 5.23: Pressure amplitude corresponding to the frequency  $f = 40f_n$  at the full load operating point, OP III, on the impeller blade as well as on the shroud.

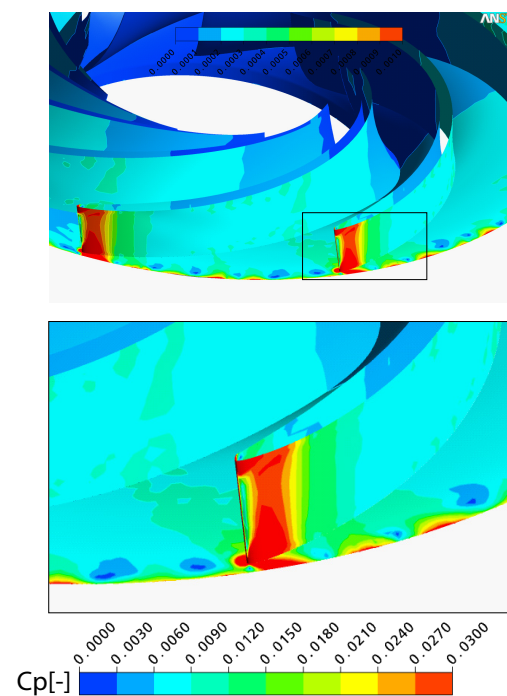


Figure 5.24: Pressure amplitude corresponding to the frequency  $f = 60f_n$  at the full load operating point, OP III, on the impeller blade as well as on the shroud.

Figure 5.25 represents the phase values corresponding to the frequency  $f = 20f_n$  at the full load operating point, OP III, on mid span plane. A constant phase shift between the pressure peaks in neighboring impeller channels is detected. To understand the reason of this phase shift, one should regard to the combination of the guide vane and impeller numbers. The guide vanes and impeller blades have different blade numbers. It causes a time difference between the arrivals of a blade channel to the equivalent position of the prior channel. Therefore, a phase lag between the pressure peaks in two neighboring impeller blades is detected, which is associated with the pitch angle between impeller and guide vane channels.

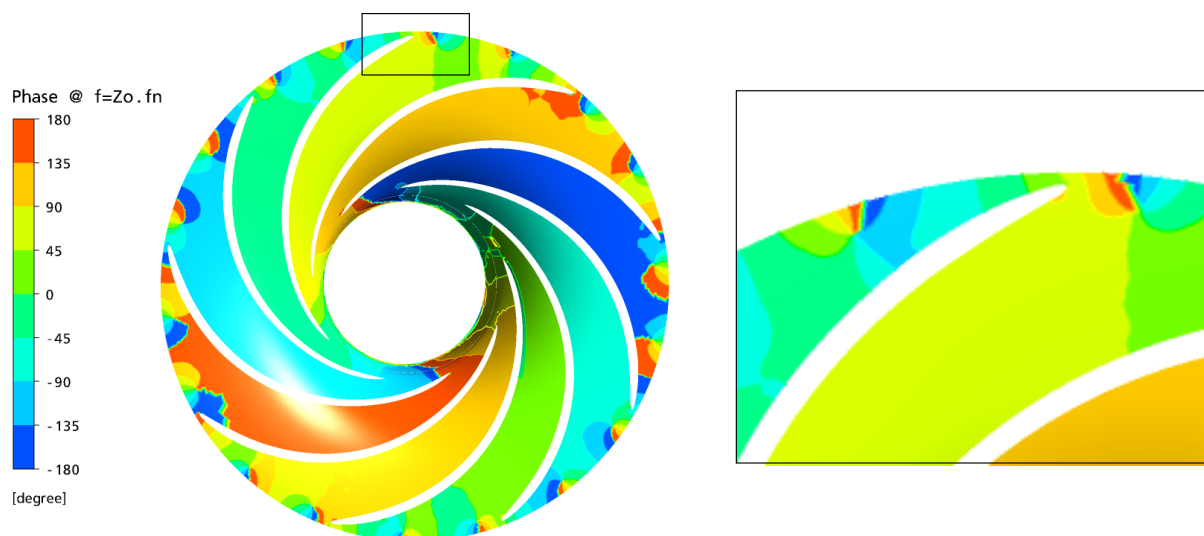


Figure 5.25: Phase values corresponding to the frequency  $f = 20f_n$  at the full load operating point, OP III, at mid span plane of the impeller.

### Pressure Fluctuations at the Leading Edge of Impeller

The experienced pressure at the leading edge is obtained from the difference of time history pressure value between both sides of a blade. The time history of pressure fluctuations at two monitoring points,  $b1$  and  $b7$ , located at both pressure and suction sides of a blade leading edge are represented in Figure 5.26. As it is shown, a phase shift between the two pressure signals is observed. This is the reason why the pressure fluctuations due to the difference between pressure and suction sides at the leading edge,  $b17 = b1 - b7$ , is higher than pressure fluctuations at both pressure and suction sides,  $b1$  and  $b7$ , see Figure 5.27. Moreover, the interaction between the spiral casing tongue and the runner blades produces a pressure fluctuation at the rotational frequency of turbine,  $f_n$ , see Figure 5.27.

The phase shift between the two sides of the blade leading edge at three conditions, part load, best efficiency and full load operating points is investigated. In Figure 5.28, the pressure fluctuations at both sides and corresponding frequency spectra are represented. As it is shown, the dominant frequencies are  $f_n$  and  $f = 20f_n$ , moreover at full load operating point the frequency  $f = 40f_n$  indicates a high pressure amplitude.

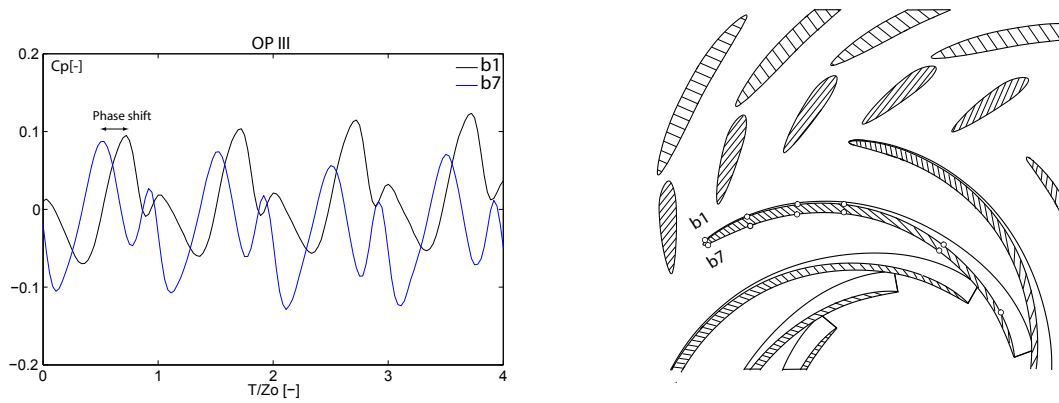


Figure 5.26: Full load operating point, OP III:(left) Time history of Pressure fluctuations at both suction and pressure sides of impeller blades, monitoring point , (right) the positions of the  $b1$  and  $b7$  monitoring points.

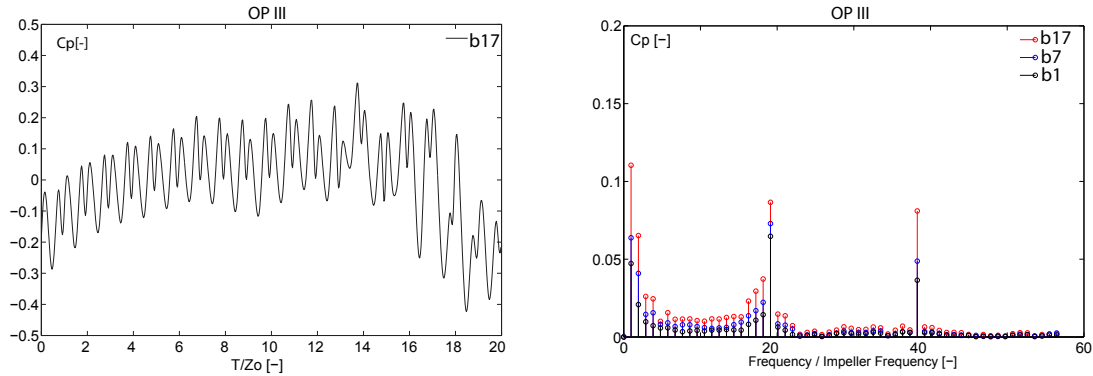


Figure 5.27: Full load operating point, OP III:(left) Time history of the pressure fluctuations at the leading edge, computed by the difference pressure between  $b1$  and  $b7$ , (right) corresponding frequency spectra  $b17$ .

The phase shift between monitoring points  $b1$  and  $b7$  at the frequency  $f = 20f_n$  shows a constant value, equal to  $\Delta\varphi = 80^\circ$ , for the three investigated operating points, see Figure 5.29. This value at the frequency  $f = 40f_n$  at the full load operating point increases to  $\Delta\varphi = 160^\circ$ . Consequently, the effect of phase shift at the leading edge is more considerable at the frequency  $f = 40f_n$ .

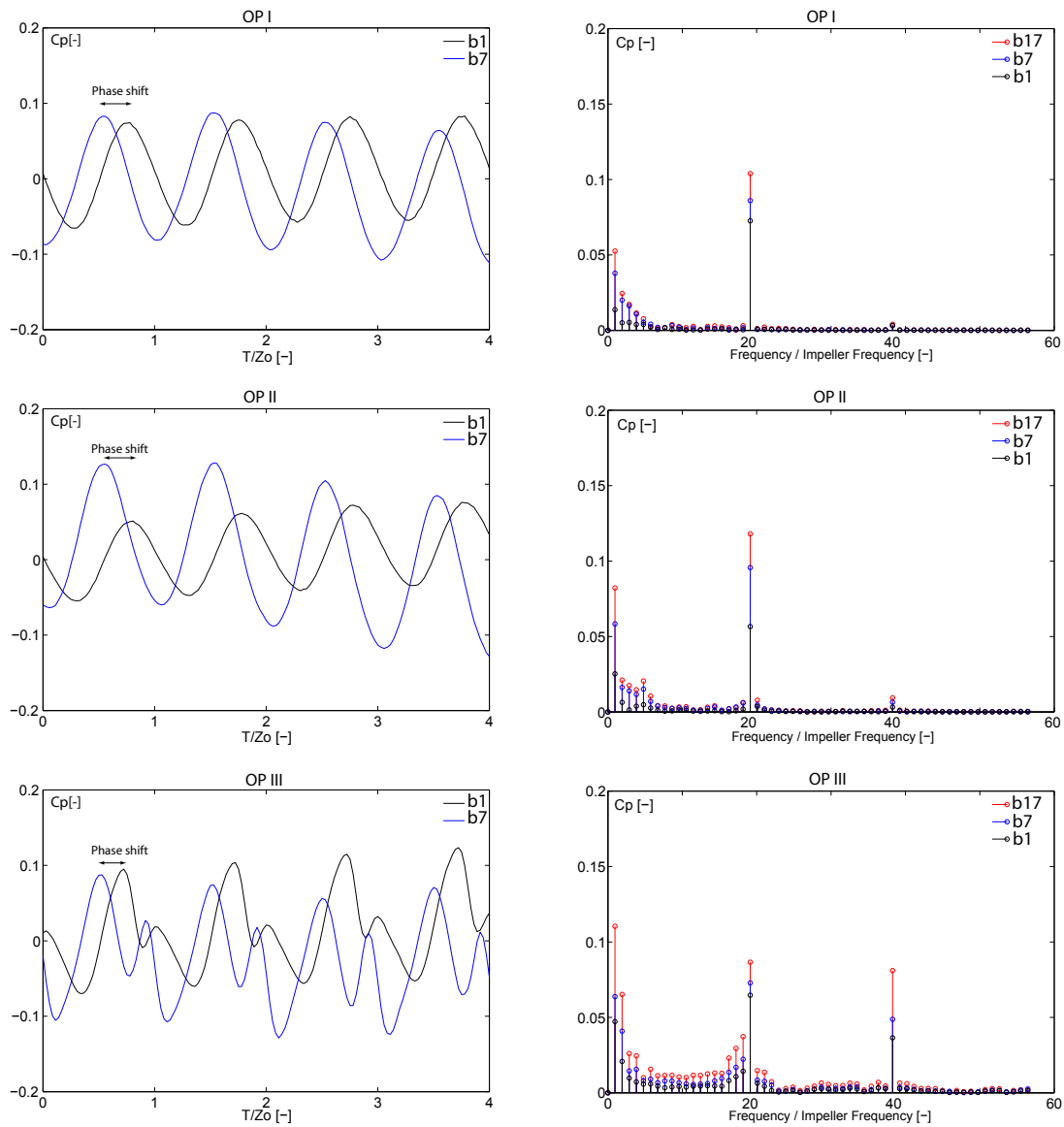


Figure 5.28: (left) Time history of the pressure fluctuations at both sides of the leading edge,  $b1$  and  $b7$ , (right) corresponding frequency spectra  $b17$ , at the investigated operating points, OP I (top), OP II (middle) and OP III (bottom)

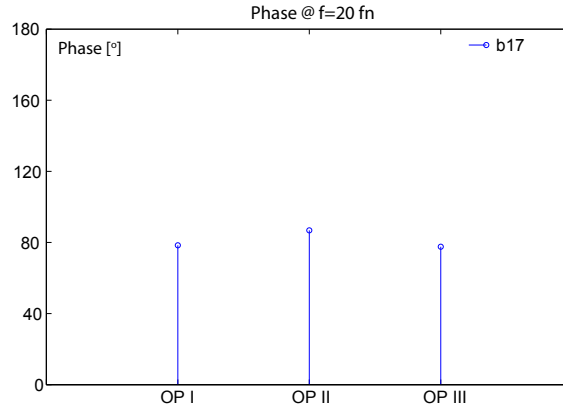


Figure 5.29: Phase shift between the monitoring points  $b1$  and  $b7$  at three investigated operating points.

The predicting of phase shift between pressure and suction sides of impeller blades is important to estimate the exerted force on the leading edges. It is supposed that this phase shift is related to the pitch angle between impeller and guide vane channels, see Figure 5.30. It is expressed with Equation 5.1, where  $\Delta\varphi$  is the phase shift,  $n$  is integer number,  $z_o$  is the guide vane number and  $z_b$  is the impeller blade number.

$$\Delta\varphi = \left( \frac{2\pi}{z_b} - n \frac{2\pi}{z_o} \right) \Rightarrow \quad \Delta\varphi = \frac{2\pi}{z_o} \left( \frac{z_o}{z_b} - n \right) \quad (5.1)$$

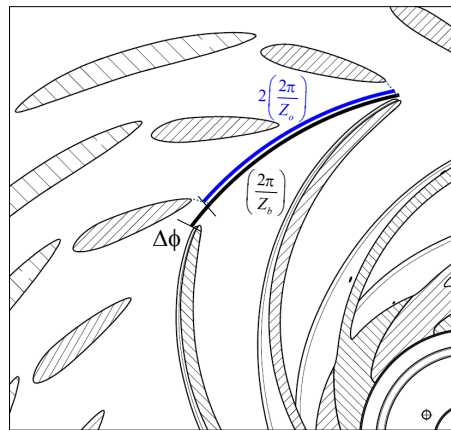


Figure 5.30: Modulation process between impeller blade flow and guide vanes flow field.

Moreover, the frequency of pressure fluctuations due to RSI in the rotating frame,  $f_b$  is a multiple of guide vane number,  $z_o = 20$  to the frequency of impeller revolution,  $f_n$ , see Equation 5.2:

$$f_b = z_o f_n \quad (5.2)$$



Consequently, the same relationship exists between the angular position of the impeller blade and time history of pressure value. Equation 5.3 indicates the mentioned relationship.

$$p_b = A\cos(\omega_b t + \varphi_b) = A\cos(z_o(\omega t + \varphi)) \quad (5.3)$$

where  $\omega_b$  is the angular velocity of pressure fluctuation in the rotating frame and  $\varphi_b$  is the corresponding phase value.  $\omega$  represents the impeller angular velocity and  $\varphi$  is the phase of impeller position from the reference. The relationship between angular position of two successive impeller blades,  $\varphi$ , and phase shift between the rotor-stator pressure fluctuations  $\varphi_b$ , is expressed with Equation 5.4.

$$\varphi_b = z_o \varphi \quad (5.4)$$

Equation 5.3 and 5.1 lead us to the following equation:

$$\Delta\varphi_b = 2\pi \left( \frac{z_o}{z_b} - n \right) \quad (5.5)$$

The phase shift between the pressure values at two successive impeller blades is defined with Equation 5.6. In the present case study this phase shift is  $\Delta\varphi_b = 80^\circ$

$$\Delta\varphi_b = 2\pi \left( \frac{z_o}{z_b} - 1 \right) = 2\pi \left( \frac{20}{9} - 1 \right) \quad (5.6)$$

### 5.3 Resulting Modes of RSI

According to the RSI model, the pressure fluctuations due to the RSI are the result of the interaction between two non-uniform velocity-pressure fields. One coming from the guide vanes and the other is the non-uniform pressure field at the runner inlet. In the stator frame, the non uniform flow field at the guide vane outlet caused by wake effect and blade loading generates a periodic flow pattern. In the rotor frame also, the pressure field attached to the rotating impeller blade induces periodic flow field distortions [13], [96]. These stationary and rotating periodic flows can be expressed as the following Fourier series:

$$p_s(\theta_s, t) = \sum_{n=0}^{\infty} A_n \cdot \cos(nz_o\theta_s + \varphi_n) \quad (5.7)$$

$$p_r(\theta_r, t) = \sum_{m=0}^{\infty} A_m \cdot \cos(mz_b\theta_r + \varphi_m) \quad (5.8)$$

Where  $m$ ,  $n$  are the harmonic orders,  $A_m$ ,  $\varphi_m$  being respectively the amplitude and the phase for the  $m^{th}$  harmonic,  $\theta_r$ ,  $\theta_s$  being the angle coordinates in, respectively, the rotating and the stationary systems,  $z_b$  is the impeller blade number and  $z_o$  is the guide vanes number. The resulting pressure field, combining the guide vane and the impeller blade pressure fields are characterized by a strong modulation process as illustrated in Figure 5.31. Therefore this modulation can be expressed as the product of both pressure fields:

$$p = \left[ \sum_{n=0}^{\infty} A_n \cdot \cos(nz_o\theta_s + \varphi_n) \right] \cdot \left[ \sum_{m=0}^{\infty} A_m \cdot \cos(mz_b\theta_r + \varphi_m) \right] \quad (5.9)$$

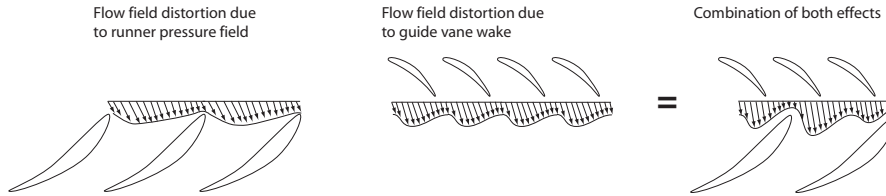


Figure 5.31: Modulation process between impeller blade flow and guide vanes flow field

This modulation for one harmonic is expressed as Equation 5.10

$$p_{mn}(\theta_r, \theta_s) = A_{mn} \cdot \cos(mz_b\theta_r + \varphi_m) \cdot \cos(nz_o\theta_s + \varphi_n) \quad (5.10)$$

According to the impeller angle coordinate expression for the stationary reference frame,  $\theta_r = \theta_s - \omega t$ , the modulation yields the following resulting pressure field:

$$p_{mn}(t, \theta_s) = \frac{A_{k_2}}{2} \cdot \cos(mz_b\omega t - \overbrace{(mz_b + nz_o)}^{k_2} \theta_s + \varphi_n + \varphi_m) + \frac{A_{k_1}}{2} \cdot \cos(mz_b\omega t - \overbrace{(mz_b - nz_o)}^{k_1} \theta_s - \varphi_n + \varphi_m) \quad (5.11)$$

where  $k_1$  and  $k_2$  are the contributions of high and low order diametrical pressure modes. indicates the rotating direction of diametrical mode, positive  $k$  value meaning a rotational mode in the same direction than that of the impeller.

$$p_{mn}(t, \theta_s) = \frac{A_{k_2}}{2} \cdot \cos(mz_b\omega t - k_2\theta_s + \varphi_n + \varphi_m) + \frac{A_{k_1}}{2} \cdot \cos(mz_b\omega t - k_1\theta_s - \varphi_n + \varphi_m) \quad (5.12)$$

According to the blade arrangement in this case study,  $z_o = 20$  and  $z_b = 9$ , the RSI model determines the modes of pressure fluctuations in the pump-turbine. The pressure values at a given time step are analyzed at the circular section in the vaneless gap, see Figure 5.32.

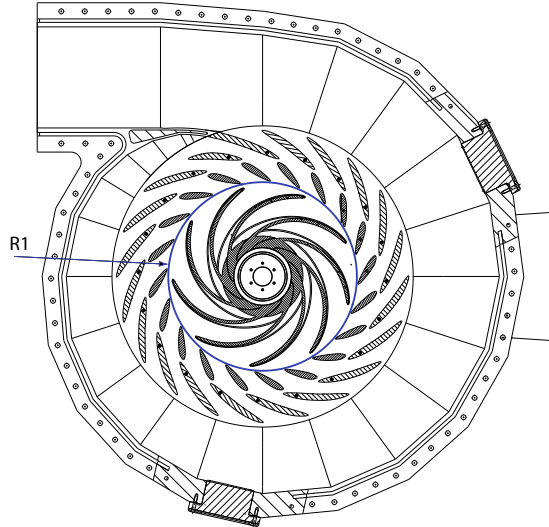


Figure 5.32: Section of the selected monitoring sections of  $R1$ , in the vaneless gap.

Instantaneous pressure values at the vaneless gap, section  $R1$ , are represented in Figure 5.33. Accordingly, the pressure peaks correspond to the impact of flow stagnation at the leading edge of impeller blades. It is modulated with the non-uniform pressure field at the guide vane outlet. The corresponding frequency spectra highlight the resulting

modes of rotor-stator interaction. Accordingly, Figure 5.34 represents all the main frequencies correlated with RSI. The frequencies of pressure fluctuations in the stationary frame,  $f = 9f_n$ , rotating frame,  $f = 20f_n$ , and their harmonics as well as the frequencies corresponding to the diametrical modes,  $f = 2f_n$   $f = 11f_n$ , are detected.

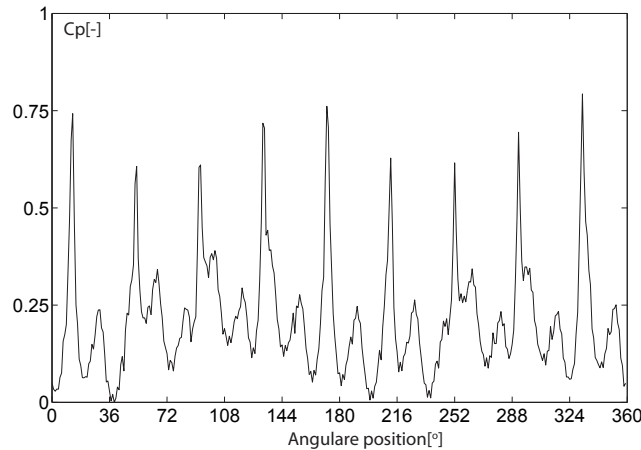


Figure 5.33: The instantaneous pressure coefficient at the periphery of rotor-stator zone,  $R1$

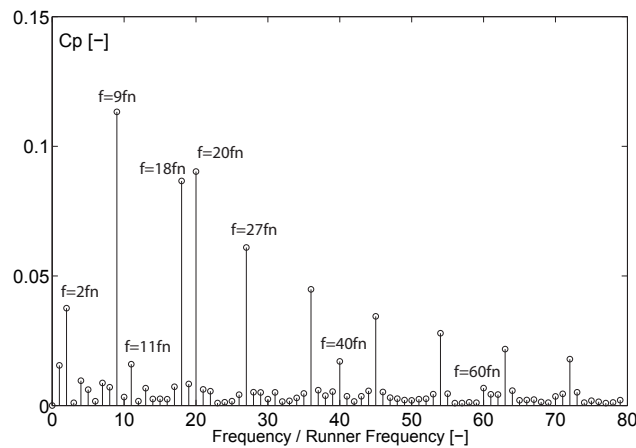


Figure 5.34: The spectral analysis of the instantaneous pressure coefficient at all monitoring points around the radius  $R1$

Pressure fluctuation due to RSI at the periphery of turbine is a function of time (blade passing) and angular position (non-uniform flow pattern at the periphery due to wakes and blade loading). 2D Fourier transform could be an appropriate method to determine the pressure amplitude of blade passing frequencies and diametrical modes.

Figure 5.35 represents the results of the 2D frequency spectrum, where the line  $n = 0$  indicates the amplitudes and frequencies of the pressure fluctuations in the stationary

frame. The line  $m = 0$  represents these terms, pressure amplitudes and frequencies, in the impeller and  $k$  axis shows the diametrical modes. 2D Fourier transform method permits to identify the pressure amplitudes corresponding to each harmonic of the frequencies in the stator frame,  $n$  lines, as well as rotor frame,  $m$  lines. The pressure amplitude corresponding to the diametrical modes are represented in Table 5.1. Accordingly, the most high pressure amplitude is represented at diametrical mode  $k = 2$ . 2D frequency spectrum method enables to determine the pressure amplitude of diametrical modes, which could be one of the origins of the vibration and resonance in turbine.

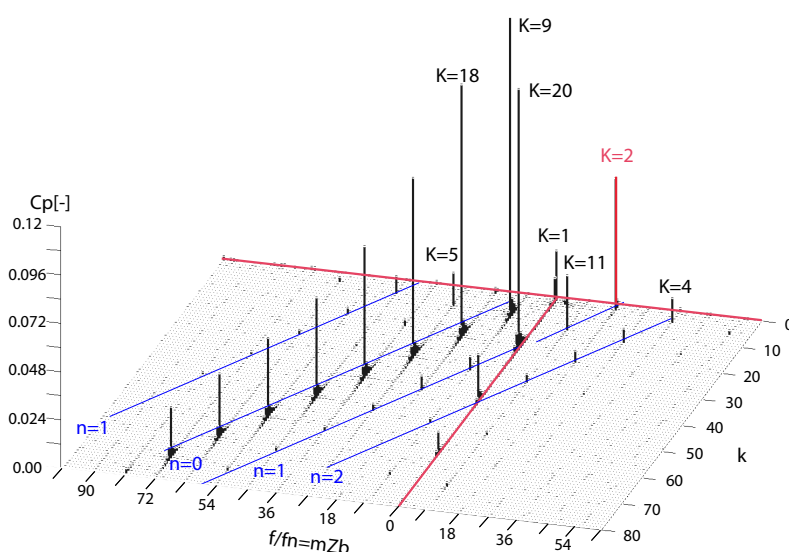


Figure 5.35: Spectral analysis in space and in time at the periphery of the rotor-stator zone, section  $R1$ , during one impeller revolution

Table 5.1: RSI patterns of the pump-turbine

$n$	$m$	$k_1 = mZ_b - nZ_o$	$k_2 = mZ_b + nZ_o$	$A_{k_1}$	$A_{k_2}$
1	1	-11	29	0.018	0.005
<b>1</b>	<b>2</b>	<b>-2</b>	<b>38</b>	<b>0.045</b>	<b>0.005</b>
1	3	7	47	0.012	0.002
2	4	-4	76	0.009	0
2	5	-5	85	0.006	0

## 5.4 Influence of operating points on RSI

The evaluation of pressure fluctuations due to RSI as a function of operating condition is investigated in the present section. For more analysis, 15 operating conditions at a constant specific energy are selected, see Figure 5.36. The last mentioned operating points cover all range of discharge coefficients from the part load to the full load operating points. The analysis of the unsteady pressure, resulting of the measurements permit to evaluate and predict the importance of RSI at different operating points.

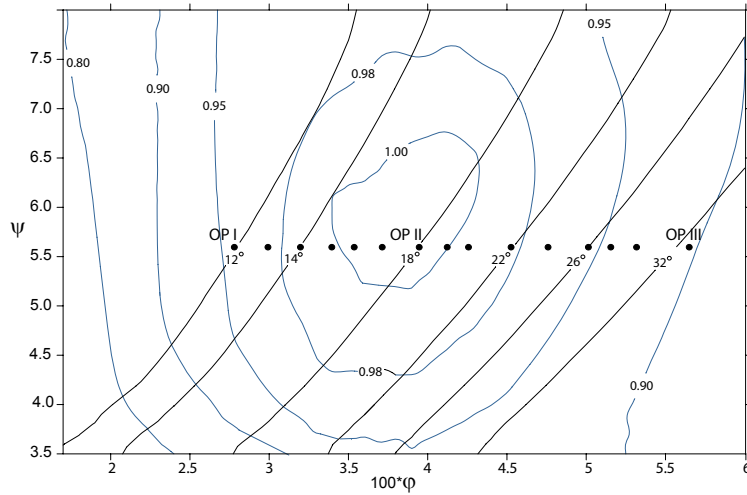


Figure 5.36: The 15 investigated operating points at a constant specific energy to study the pressure fluctuations at a large range of operating conditions

Figure 5.37 represents the experimental results of pressure oscillation at 4 monitoring points in a distributor channel. These results are compared at three investigated operating points, part load, OP I, best efficiency, OP II and Full load operating point, OP III. Accordingly, the higher discrepancy occurs at the guide vane outlet, monitoring point 69 and gradually decreases toward the upstream of the distributor channel. At monitoring point 40, which is located at the stay vane inlet, no significant discrepancy is detected. Thereby, the effect of operating points to the pressure fluctuations due to RSI is investigated in the vaneless gap. Table 5.2 represents the pressure fluctuations at three investigated operating points.

Table 5.2: Pressure amplitude in a distributor channel relative to OP III.

Operating point	$9fn$	$18fn$	$27fn$
OP I	0.2	0.3	0.5
OP II	0.5	0.6	0.7
OP III	1	1	1

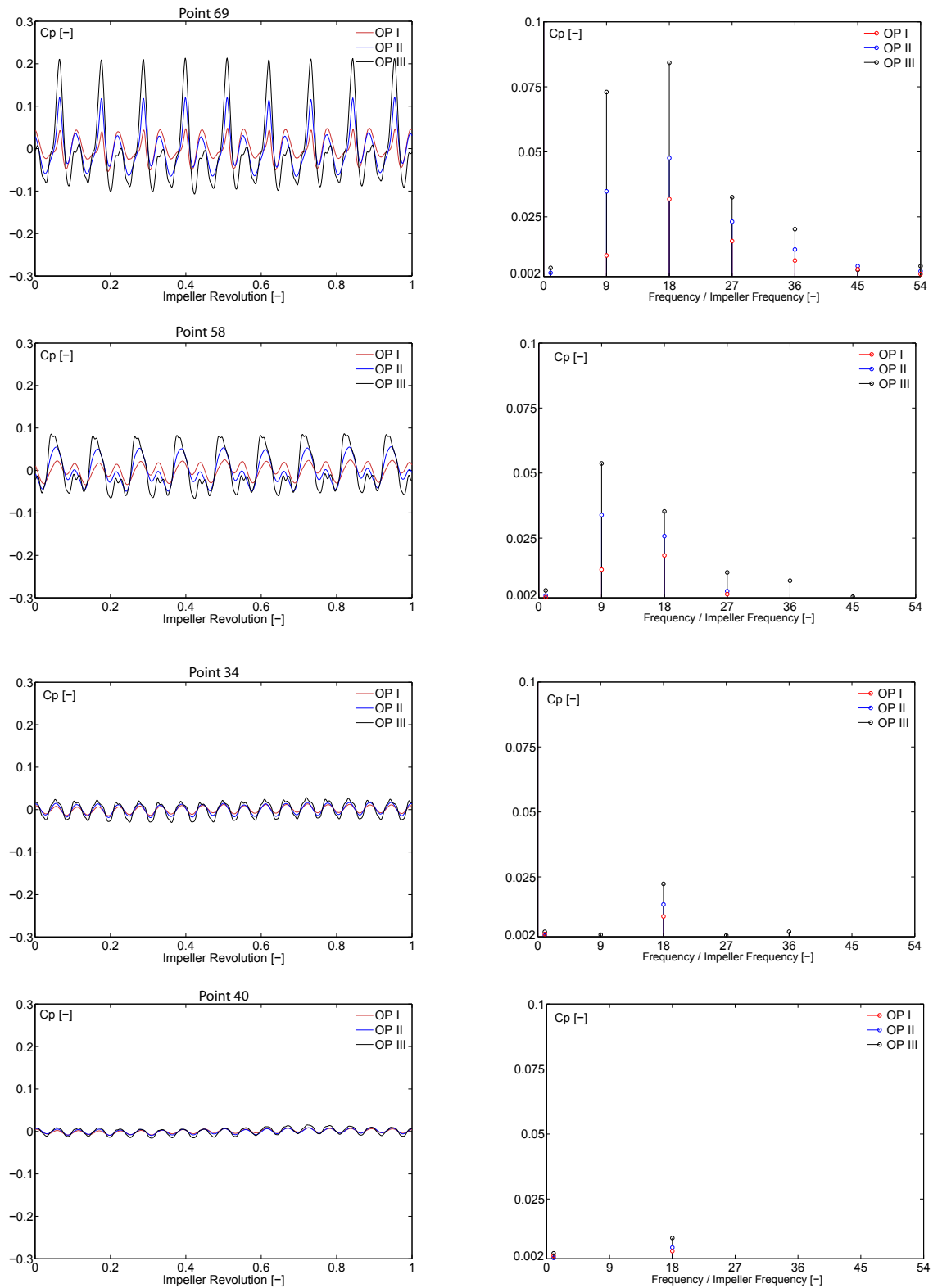


Figure 5.37: Measurements: Time history oscillations and spectral analysis of pressure coefficient in a distributor channel, at part load, OP I, rated, OP II, and full load operating point, OP III.

The pressure fluctuation on an impeller blade is illustrated in Figure 5.38 and Figure 5.39. Accordingly, there is no significant discrepancy between the pressure amplitude at the monitoring point  $b1$ , located at the leading edge. However, at the full load operating point, this value is very strong at frequency  $f = 40f_n$ . The evaluation of the pressure amplitudes at the guide vane passing frequency,  $f = 20f_n$ , at the monitoring points  $b1$  to  $b3$  are represented in Table 5.3.

Table 5.3: Pressure amplitude in the impeller relative to OP III.

Operating point	$b1$	$b2$	$b3$	$b4$
OP I	1.1	0.5	0.8	1
OP II	0.9	0.8	0.9	1
OP III	1	1	1	1

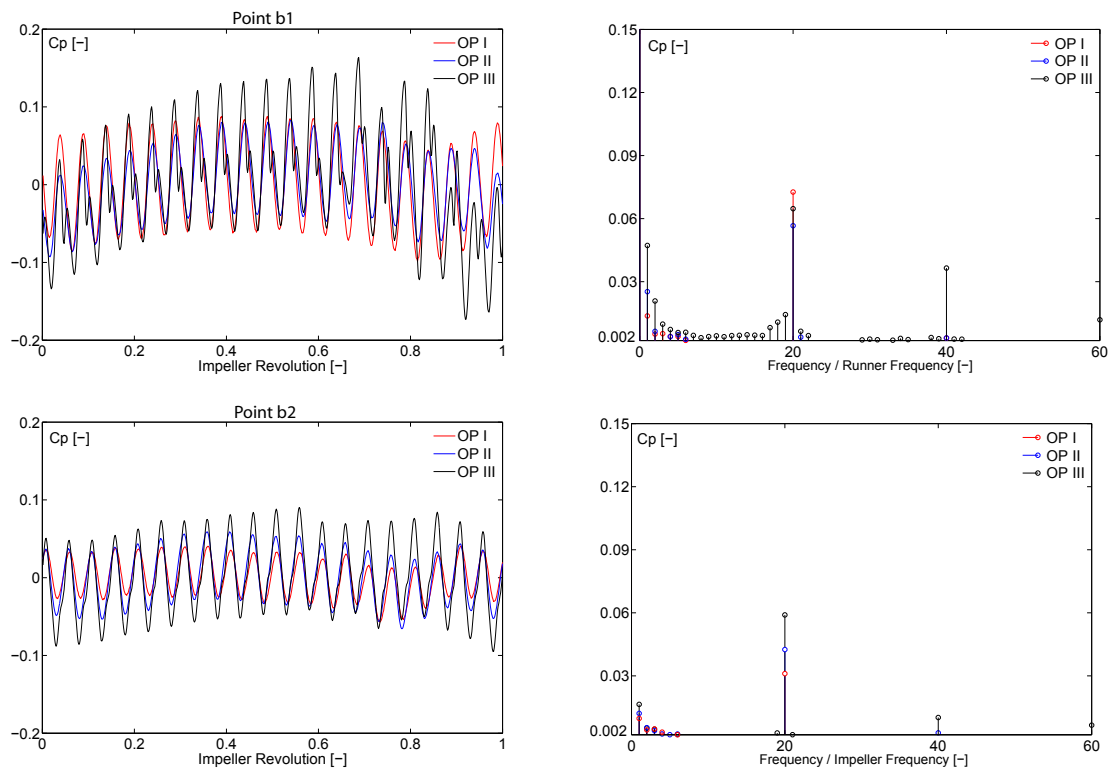


Figure 5.38: Measurements: Time history oscillations and spectral analysis of pressure coefficient in the impeller, at part load, OP I, BEP, OP II, and full load operating point, OP III.



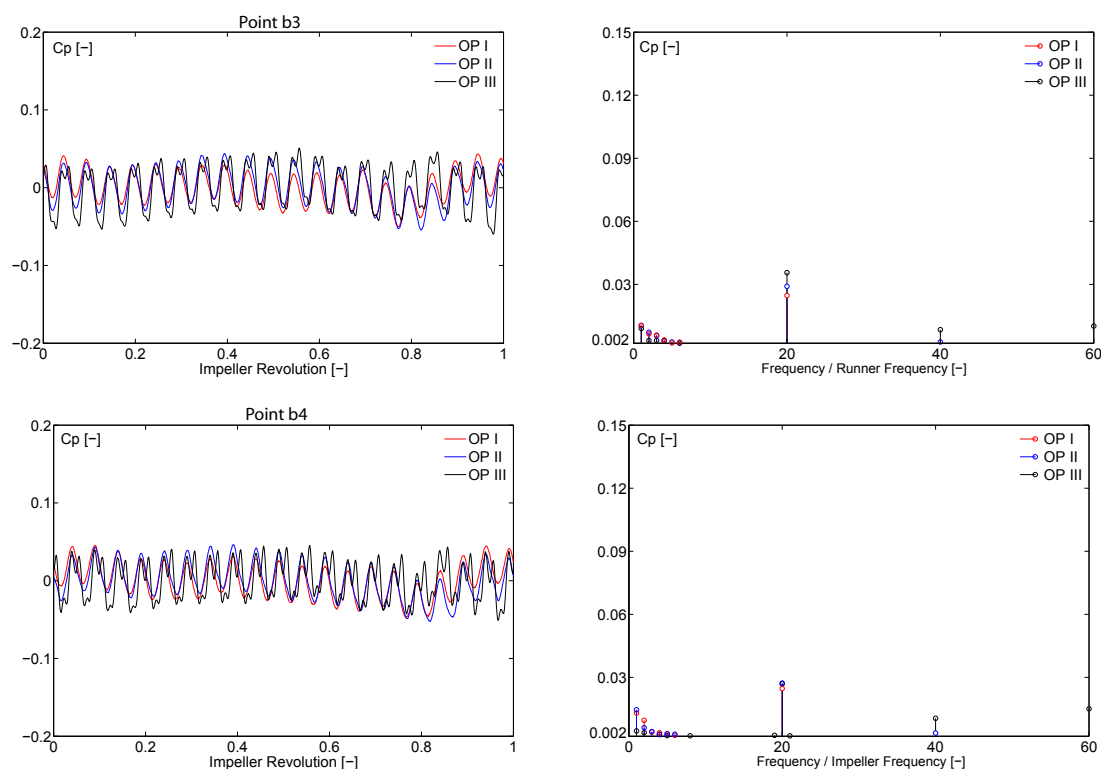


Figure 5.39: Measurements: Time history oscillations and spectral analysis of pressure coefficient in the impeller, at part load, OP I, rated, OP II, and full load operating point, OP III.

By changing the guide vane opening, the position of the fixed pressure sensors change relative to the guide vane channel. To avoid any error caused, 4 monitoring points that cover the outlet section of a guide vane channel are considered. The experimental results of pressure fluctuations at these 4 monitoring points,  $O1$  to  $O4$ , are represented in Figure 5.40. This comparison is performed for three operating points, OP I to OP III. By considering the time history of mentioned results, a phase lag is observed in the time occurrence between the pressure peaks of mentioned monitoring points. It is caused by the arrival time of the rotating impeller to monitoring points. Based on these results, the maximum perturbation appears at the monitoring point  $O3$  for all three operating points. Accordingly, monitoring point  $O3$  is selected to analyze the evaluation of the pressure fluctuations due to rotor-stator interaction for 15 operating points from part load to full load operating conditions.

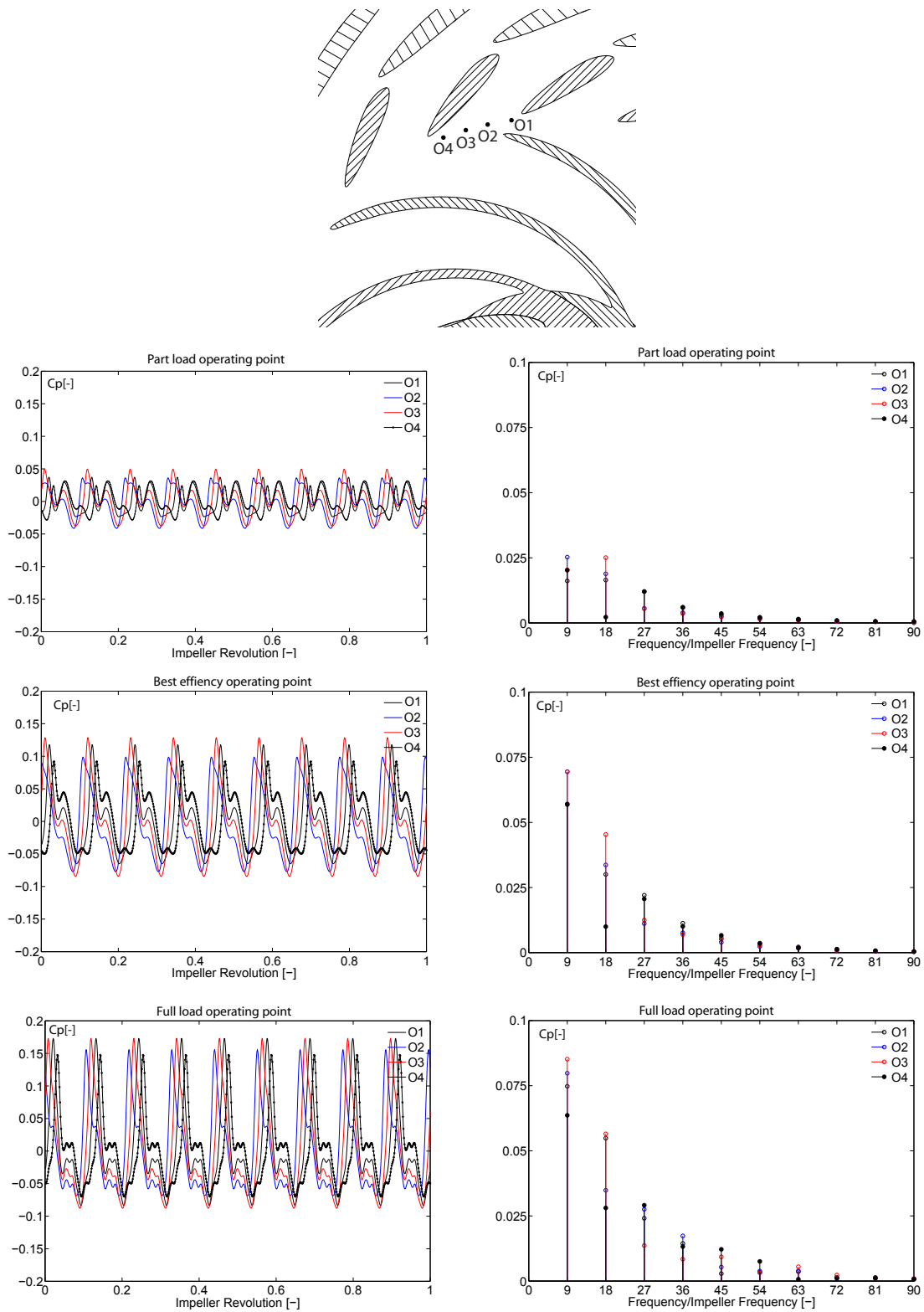


Figure 5.40: Measurements: Time history oscillations and spectral analysis of pressure coefficient in the vaneless gap, monitoring point O1 to O4, at part load, OP I, rated, OP II, and full load operating point, OP III.

The variation of the pressure fluctuation due to rotor-stator interaction depends on the operating conditions. For a given turbine, by changing the operating point, several parameters might be changed; such as discharge,  $Q$ , angular velocity of impeller,  $\omega$ , vaneless gap between guide vanes and impeller,  $r_{gap}$ , and hydraulic energy,  $E$ . Figure 5.41 represents the pressure amplitude corresponding to the blade passing frequency and its harmonics versus non-dimensional discharge at 15 operating points. The amplitudes of the pressure fluctuations increase from part load to the best efficiency point (BEP) and with the different slope increase again from the BEP to the full load operating point. Figure 5.42 indicates the pressure amplitudes at the blade passing frequency and its harmonics as a function of vaneless gap,  $r_{gap}$ . Accordingly, the effect of RSI is increased by decreasing the vaneless gap, from part load to full load operating point. The line BEP indicates the best efficiency operating condition.

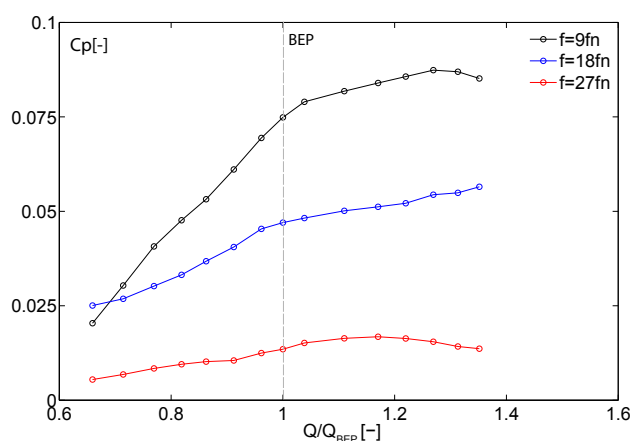


Figure 5.41: Measurements: Pressure amplitudes at the blade passing frequency and its harmonics as a function of discharge at 15 operating points

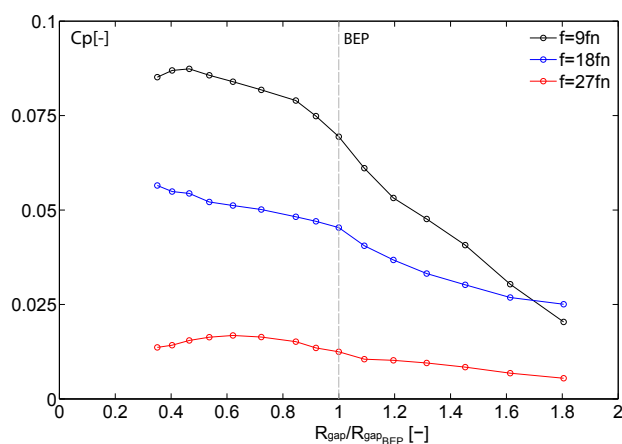


Figure 5.42: Measurements: Pressure amplitude at the blade passing frequency and its harmonics as a function of vaneless gap at 15 operating points

A non-dimensional number,  $\zeta$ , based on the specific speed,  $\nu$ , and vaneless radial gap,  $r_{gap}$ , is defined to evaluate the pressure amplitudes at the different operating points. Specific speed,  $\nu$ , involves the three above mentioned variables (discharge,  $Q$ , angular velocity,  $\omega$ , and energy,  $E$ ). It is expressed as below:

$$\nu = \frac{\varphi^{1/2}}{\psi^{3/4}} = \left(\frac{Q}{\pi\omega r^3}\right)^{1/2} \cdot \left(\frac{\omega^2 r^2}{2E}\right)^{3/4} \quad (5.13)$$

Then, the influence of the vaneless gap,  $r_{gap}$ , is taken into account and non-dimensional number  $\zeta$ , could be introduced such as:

$$\zeta = \frac{r_{\bar{1}}}{r_{gap}} \nu^2 \quad (5.14)$$

$$\zeta = \frac{r_{\bar{1}}}{r_{gap}} \cdot \frac{Q\omega^2}{\pi(2E)^{3/2}} \quad (5.15)$$

where  $r_{\bar{1}}$  is the outlet runner radius,  $r_{gap}$  is the gap distance between guide vane outlet and impeller inlet,  $Q$  is the discharge and  $E$  is the hydraulic energy.

The  $\zeta$  number, quantifies the amplitude of pressure fluctuations at different operating points. Figure 5.43 represents the pressure amplitudes at the blade passing frequency and its harmonics in function of  $\zeta$ . As it is shown, the amplitudes of the pressure fluctuations increase by increasing  $\zeta$ . For the operating conditions between BEP to full load, the increase of pressure amplitude is linear at the twice of blade passing frequency  $f = 18f_n$ .

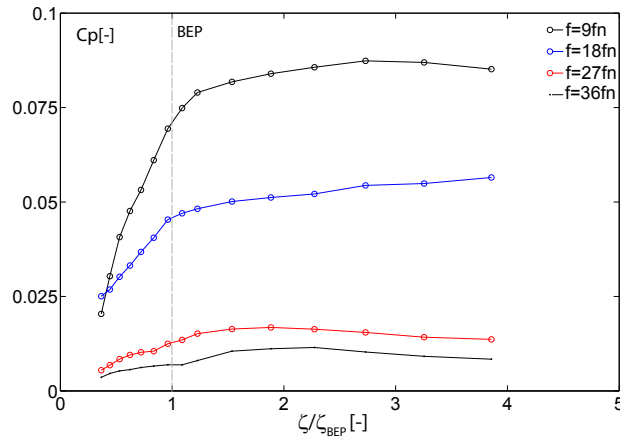


Figure 5.43: Measurements: Pressure amplitude at the blade passing frequency and its harmonics in function of  $\zeta/\zeta_{BEP}$  at 15 operating points

Accordingly, it is found that the magnitudes of the pressure fluctuations well correlate with the proposed function for the 15 operating conditions investigated from the part load through the full load conditions. The  $\zeta$  number should be tested and confirmed by more case studies.

## **Part III**

# **PRECESSING VORTEX ROPE**



# Chapter 6

## Numerical Simulation of Vortex Rope

### 6.1 Numerical Configuration

#### 6.1.1 Investigated Operating Point

A cavitation-free part load operating point is investigated to predict and study the precessing vortex rope in the elbow draft tube ( $\varphi = 0.26$ ,  $\psi = 1.18$ ,  $Q = 0.7Q_{BEP}$ ,  $\sigma = 1.18$ ). The numerical results are validated by the wall pressure measurements at the wall of the cone. They are performed for a range of cavitation numbers varying from cavitation-free condition;  $\sigma = 1.18$ , to maximum rope volume,  $\sigma = 0.38$  [6]. Since, the numerical simulation is carried out for single-phase flow condition, the experimental results corresponding to the cavitation free condition are applied for numerical validations. Figure 6.1 represents the hill chart of the case study as well as the operating point.

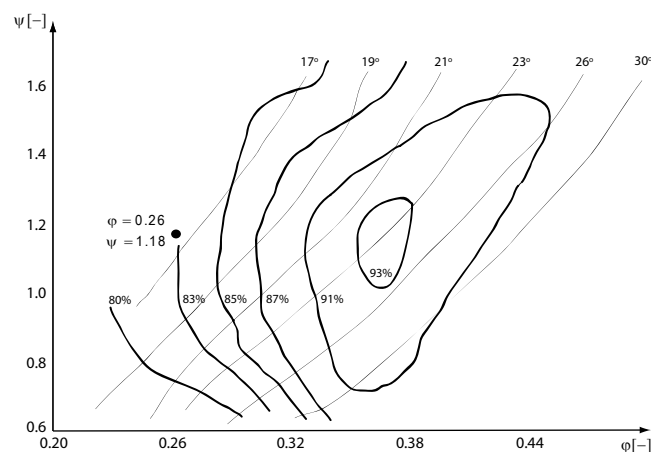


Figure 6.1: Efficiency hillchart of Francis turbine case study and investigated operating point

## 6.1.2 Computational Domain

Two configurations of computational domains are investigated. In the first one, the runner and draft tube both compose the flow passage domain. The fact that vortex rope develops in the runner and draft tube is the reason to define the first computational domain. The mentioned domain is investigated for the physical analysis of vortex rope. The second one is a reduced computational domain, made up of draft tube and the runner cone, which is used for the quality checks. The inlet section is the surface of revolution of blade trailing edge, see Figure 6.2. Three components of the averaged velocity profile, obtained from runner steady simulations, are imposed as the inlet boundary condition. The average static pressure is imposed as the outlet boundary condition.

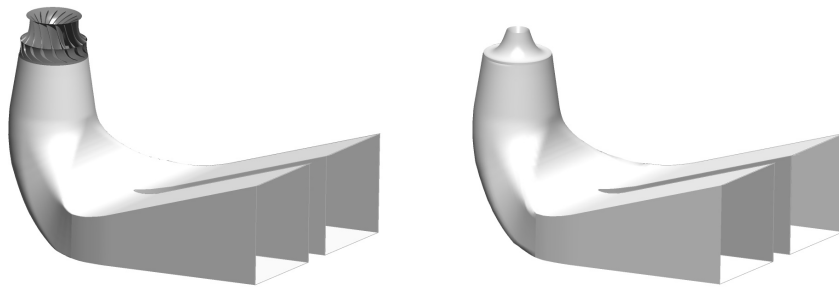


Figure 6.2: Investigated computational domains: left) Reduced domain to runner and draft tube, right) Reduced domain to draft tube and runner cone, used for quality checks

## 6.2 Quality Checks

### 6.2.1 Purpose of the Quality Checks

Depending on the phenomenon that is expected to predict (RSI or PVR), the configuration of the numerical simulation might be modified. Accordingly, a new set of quality checks is required. Mesh refinement, turbulence model and time desctitization, are the subjects of the quality checks. Figure 6.3 represents the positions, used for comparison with related measurements.

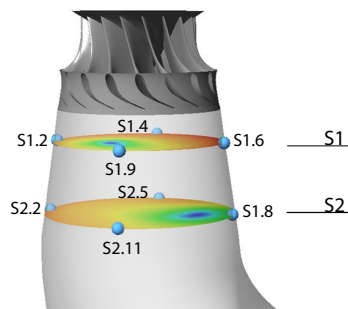


Figure 6.3: The monitoring points used for the results comparison in the cone



## 6.2.2 Spatial Discretization

The influence of the spatial discretization (mesh size) is studied. Three different mesh refinements are generated, see Table 6.1 and Figure 6.4. In all three cases, the structured fine mesh is generated in the inlet region and the cone, where the flow instability developed precessing vortex rope. Figure 6.5 represents the frequency of the vortex revolution resulting from Coarse, Medium and Fine simulations. Accordingly, the discrepancy of frequency between coarse and medium meshes is 11%. This value reduces to 5% for medium and fine meshes. Structured meshes are used in the whole computational domain.

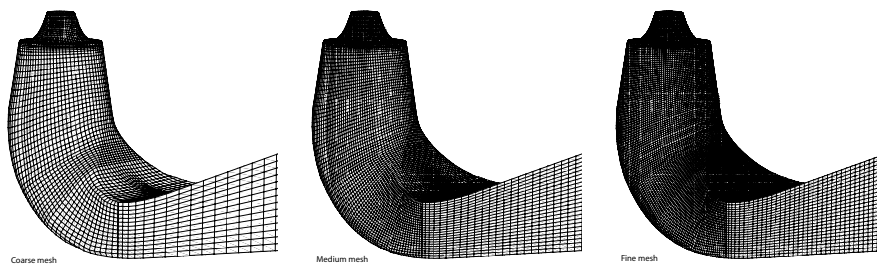


Figure 6.4: Mesh sizes: left) Coarse mesh, middle) Medium mesh, right) Fine mesh

Table 6.1: Different mesh sizes used to check mesh sensitivity

Mesh	Coarse	Medium	Fine
Cone & Elbow	200'000	700'000	1'600'000
Diffuser	50'000	200'000	400'000
Total	250'000	900'000	2'000'000

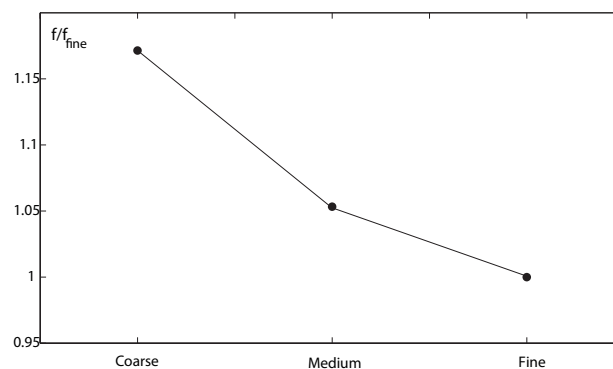


Figure 6.5: Sensitivity of spatial discretization: normalized frequency of vortex revolution at monitoring point S1.6

### 6.2.3 Turbulence Models

Three turbulence models,  $k - \varepsilon$ , SST and SAS, are applied. The frequency of the vortex rope are compared with the measurements at both sections,  $S1$  and  $S2$ , see Figure 6.6. Accordingly, better results could be obtained by using the  $SAS$  turbulence model, as the numerical simulation of vortex rope requires a turbulence model to predict the recirculation flow correctly.

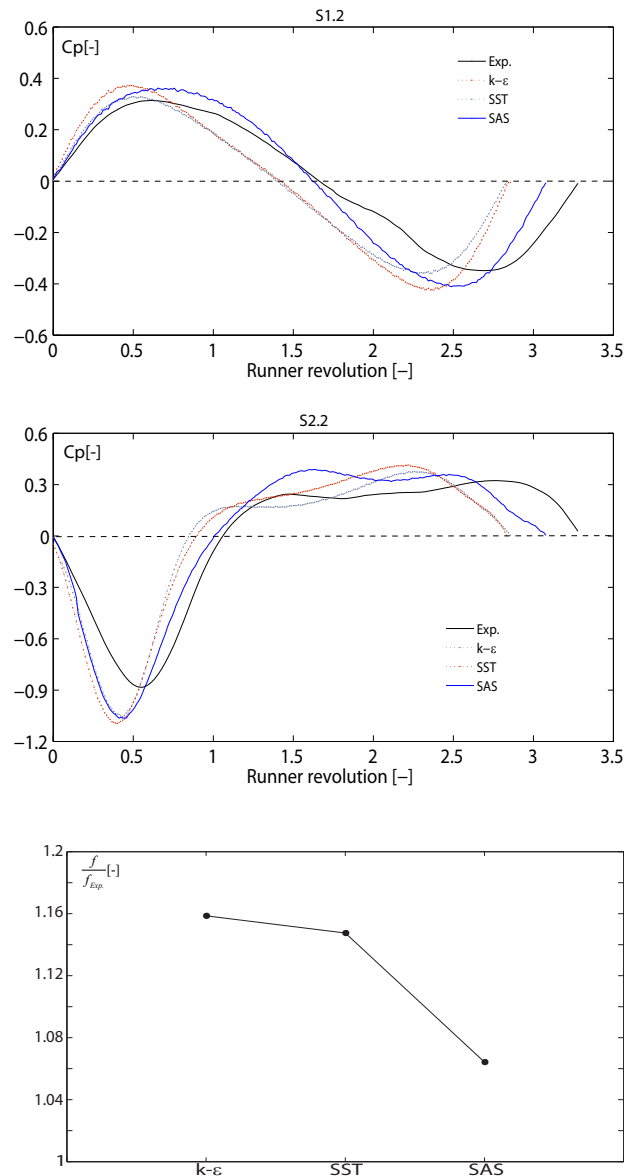


Figure 6.6: The effect of turbulence models on the vortex rope frequency in the cone at monitoring point  $S1.2$  and  $S2.2$ .

### 6.2.4 Time Discretization

The influence of time discretization (time step) on the pressure fluctuations is investigated by applying *SAS* turbulence model. Three time steps corresponding to  $1^\circ$ ,  $2^\circ$  and  $4^\circ$  of runner rotation are compared. Since the frequency of vortex rope is between 0.25 to 0.3 of runner revolution, the time step of  $4^\circ$  corresponds about to  $1^\circ$  of vortex revolution. This value is selected as the maximum time step. The medium mesh is used for this study. Figure 6.7 indicates the frequency of the vortex rope in the cone resulting from numerical simulations related to the measurements. With respect to the frequency, better result is obtained from the small time step  $1^\circ$ . However the difference between time step  $1^\circ$  and  $2^\circ$  is negligible. Therefore, the time step  $2^\circ$  is used for the numerical simulation

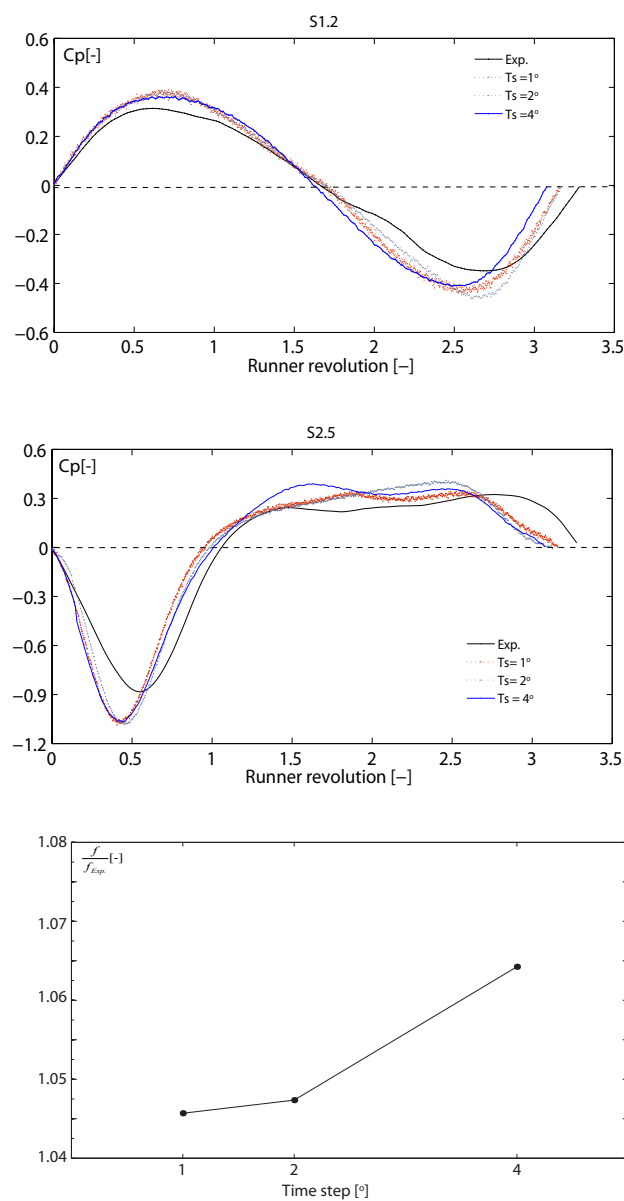


Figure 6.7: Time step sensitivity for pressure fluctuations for the time steps corresponding to  $1^\circ$ ,  $2^\circ$  and  $4^\circ$  of runner rotation

### 6.2.5 Boundary Conditions

Three-dimensional URANS flow computations are performed with the SAS turbulence model and logarithmic wall functions. The CFD package of ANSYS-CFX code is applied for modeling of vortex rope. Fully transient interface is defined at the intersection between runner and draft tube. The medium mesh is used with the time discretization set to  $2^\circ$  of runner revolution. The maximum convergence residual is fixed to  $10^{-3}$ . Second-order discretization schemes in time and in space are used. The transactional averaged velocity at the runner inlet section obtained from a previous stage flow of the stay vanes, guide vanes and runner assembly. The applied boundary conditions are summarized in Table 6.2

Table 6.2: Boundary conditions

Boundary condition	Location	Option
Inflow	Runner inlet	Velocity profile
Outflow	draft tube outlet	Const. Avg. pressure
Wall	Solid surfaces	Log. Law

Figure 6.8 represents the form of the vortex rope as well as flow pattern at a horizontal section in the cone. The pressure fluctuations resulting of this simulation are compared with the measurements at two sections of the cone, S1 and S2. Experimental phase-averaged data and numerical results of 9 impeller revolution are used for these comparisons. Figure 6.9 and Figure 6.10 represents the above mentioned comparison at 4 monitoring points at the periphery of section S1 and S2. The corresponding spectral analysis highlights the pressure amplitude values at the precessing vortex frequency and its harmonics. Accordingly, a frequency discrepancy equal to 5.1% is detected between numerical and experiential results. The numerical results obtained by the  $k - \varepsilon$  model shows 15.3% discrepancy of the vortex rope frequency with measurement.

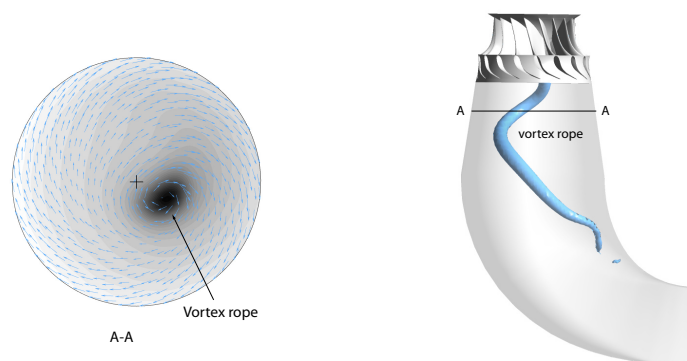


Figure 6.8: Left) flow pattern at a horizontal section in the cone, right) iso-pressure surface corresponding to the vortex rope

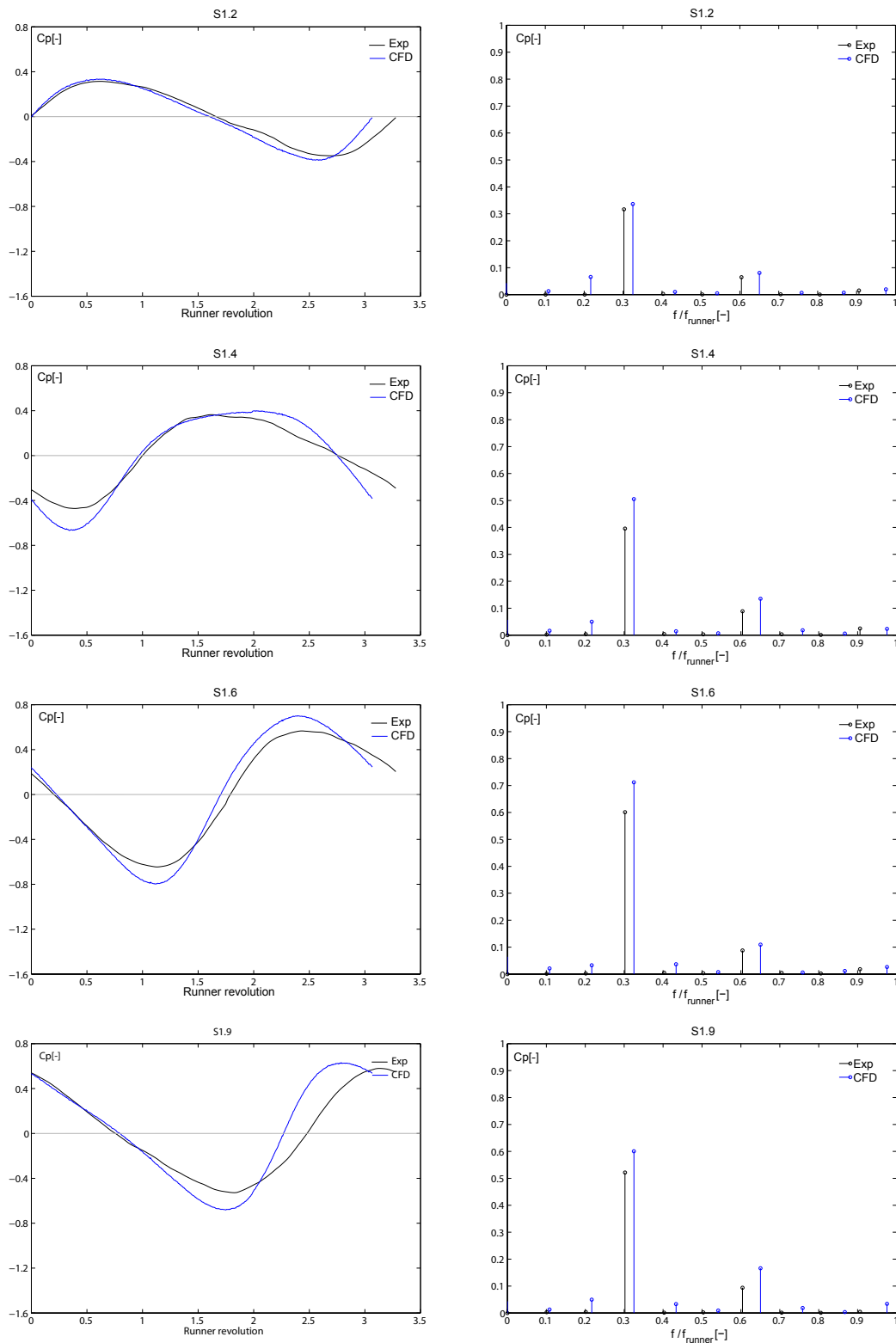


Figure 6.9: Section S1: Time history oscillations and spectral analysis of pressure coefficient, comparison between numerical and experimental results in the cone

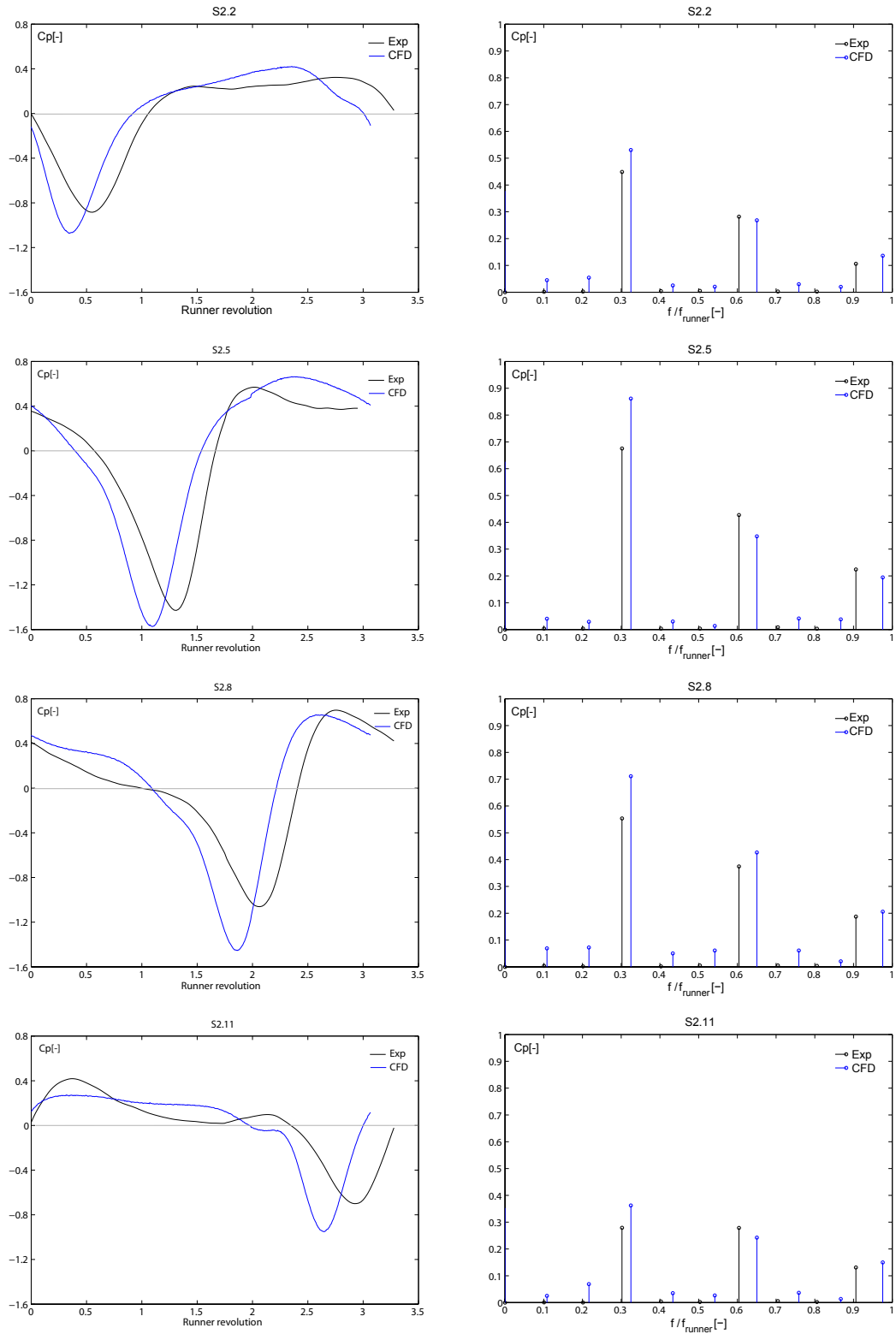


Figure 6.10: Section S2: Time history oscillations and spectral analysis of pressure coefficient, comparison between numerical and experimental results in the cone

### 6.3 Pressure Fluctuations in the Draft Tube

Pressure fluctuations in the presence of vortex rope have a complex structure in the draft tube. Several monitoring points are positioned at the periphery of two horizontal sections in the draft tube cone, see Figure 6.11. The recorded pressure fluctuations at these locations enable to follow the position of the vortex rope. Theoretically, the precessing vortex in a straight diffuser rotates with a constant rotational velocity on a circular trajectory. In a draft tube, the elbow induces a non-homogenous pressure field, which modifies the pattern of pressure fluctuations at the periphery [79].

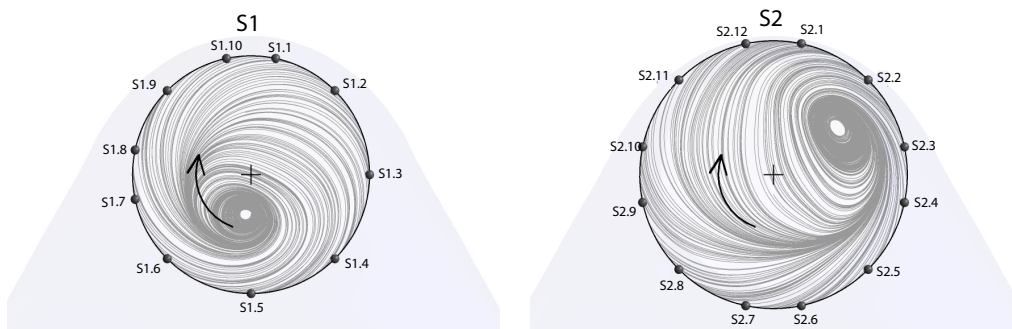


Figure 6.11: Monitoring points used for the analysis of pressure fluctuations in the cone

Figure 6.12 represents the pressure fluctuations resulting from numerical simulations at the periphery of the cone for three vortex revolution at the sections  $S1$  and  $S2$ . Regarding to the last mentioned time history, at the periphery, angular position axis, as well as in time, the axis of vortex revolution, pressure perturbations are observed .

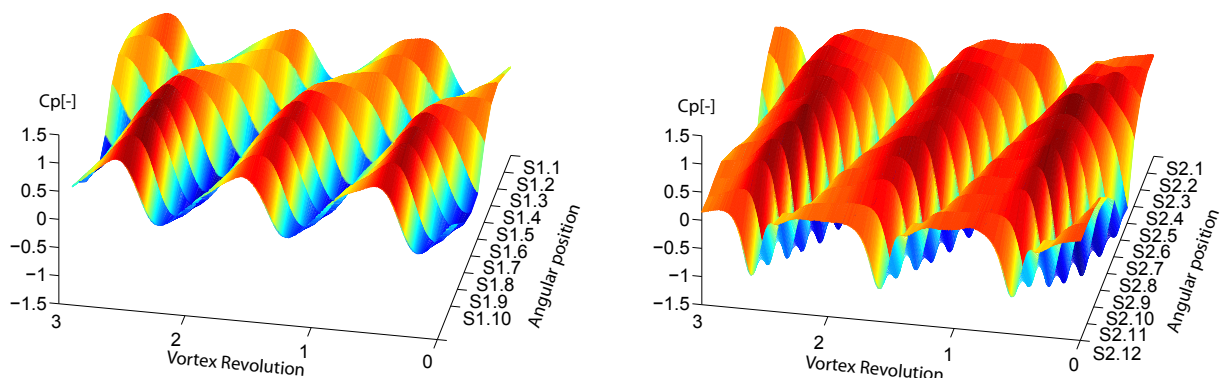


Figure 6.12: Numerical results: pressure fluctuations at the periphery of cone for three vortex revolution at sections  $S1$  (left) and  $S2$  (right)

Figure 6.13 illustrates the map of pressure fluctuations at the monitoring points, located at the periphery of the sections  $S1$  and  $S2$ . The minimum pressure value corresponds to the passage of vortex rope in front of the monitoring point. Accordingly, one can observe the trajectory of helical vortex. The minimum value corresponding to vortex passage is more pronounced at section  $S2$  than  $S1$ . The pressure fluctuations at the investigated sections,  $S1$  to  $S2$ , represents a super position of two kind of periodic fluctuations, which fluctuates with the same frequency as that of the rotating vortex, see Figure 6.13 (bottom).

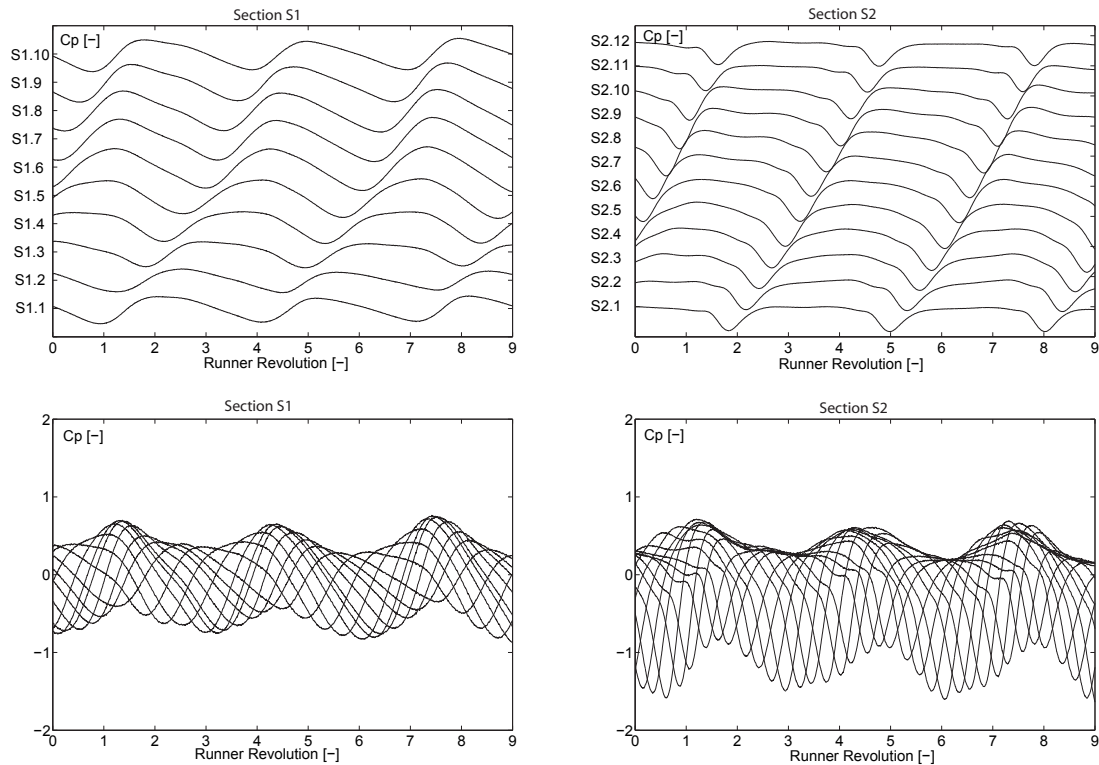


Figure 6.13: Numerical results: pressure fluctuations at the periphery of cone for three vortex revolutions at sections  $S1$  (left) and  $S2$  (right)

The pressure amplitude corresponding to the frequency of vortex rope as well as related phases are represented in Figure 6.14. It represents a sinusoidal shape where the maximum pressure amplitude occurs at monitoring point  $S1.6$  and  $S2.5$  and the minimum value detected at  $S1.2$  and  $S2.12$ . This issue indicates a displacement of the vortex center from cone axis and the trajectory of the vortex rope on the section is not circular. An angular phase shift about  $90^\circ$  is detected between the maximum pressure amplitude of the monitoring points  $S1.6$  and  $S2.5$ . The phase shift between the monitoring points is illustrated in function of their angular positions. Both numerical and experimental results show a curved shape. These results at section  $S1$  indicate the acceleration of vortex rope in the region near to the inner wall of elbow, monitoring points  $S1.4$ . This acceleration is higher in the numerical simulation than the measurements. However on section  $S2$ , flow decelerates close to the right channel of draft tube.



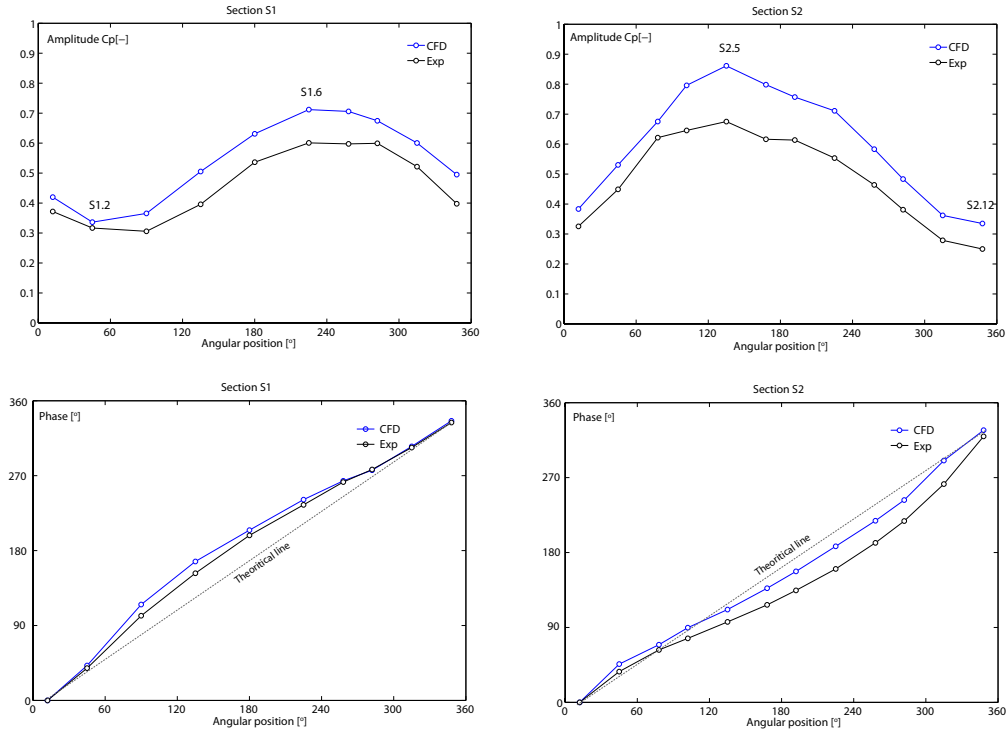


Figure 6.14: Numerical results: pressure amplitudes corresponding to frequency of vortex revolution and related phase shift at the periphery of cone at sections S1 (left) and S2 (right) for three vortex

The physical explanation of this non-linear flow behavior is based on the presence of a synchronous mode. The superposition of this pressure perturbation with the rotating mode is the cause of different pressure amplitudes at the mentioned monitoring points. At the monitoring points where the synchronous and rotating fluctuations are in phase a higher pressure fluctuations is observed. According to the literature [95], the origin of synchronous perturbation is the interaction between the non-homogenous pressure field in the elbow of the draft tube with the rotating part due to precessing vortex rope. In the case of resonance a fluid-structure interaction occurs, which could be at the origin of hydroacoustic waves and vibration. This phenomenon could be expressed by Equation 6.1, which is a superposition of two pressure fluctuations.

$$p(t) = p_{rot}(t) + p_{syn}(t) \quad (6.1)$$

These stationary and rotating periodic flows can be expressed by the following Fourier series, Equation 6.2. They fluctuate at the same frequency, however the their amplitude and phase are different.

$$p_{rot}(t) = \sum_{n=0}^{\infty} A_n \cdot \cos(n\omega t + \varphi_{rot}) \quad (6.2)$$

$$p_{syn}(t) = \sum_{m=0}^{\infty} B_m \cdot \cos(m\omega t + \varphi_{syn}) \quad (6.3)$$

Where  $m, n$  are the harmonic orders,  $A_n$  and  $B_m$ , are the pressure amplitude corresponding to rotating and synchronous mode and  $\varphi_{rot}$  is the phase of rotating part. Equation 6.4 represents the pressure fluctuations corresponding each harmonic.

$$p(t) = \sum_{n=0}^{\infty} A_n \cdot \cos(n\omega t + \varphi_{rot}) + \sum_{m=0}^{\infty} B_m \cdot \cos(m\omega t + \varphi_{syn}) \quad (6.4)$$

Figure 6.15 represents the polar representation of pressure fluctuations at the frequency of vortex revolution. Temporal decomposition method is applied to identify the rotating and synchronous components of vortex rope. The blue vectors indicate the pressure amplitudes and phase values at the investigated monitoring points. Around the blue vectors a circle with a displaced center is fitted. The radius of this circle corresponds to the pressure amplitude of the rotating component of vortex rope. The vector between the displaced center of fitted circle and the center of the graph indicates the pressure amplitude of the synchronous oscillation.

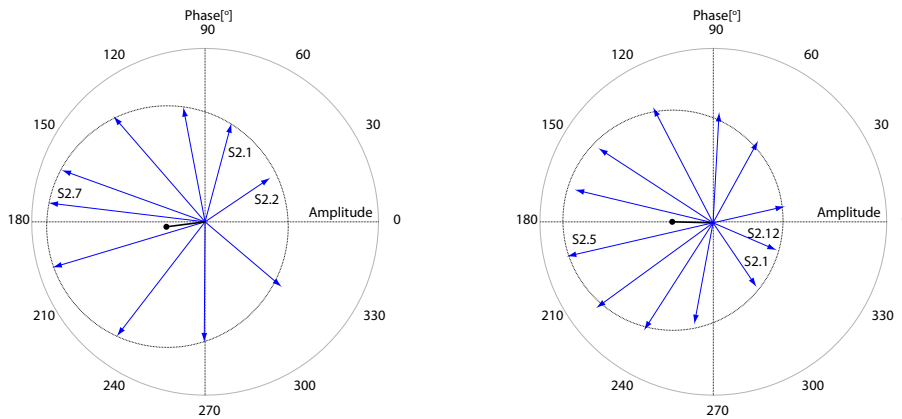


Figure 6.15: Numerical results: polar representation of pressure amplitude corresponding to the vortex rope revolution at the periphery of cone at sections  $S1$  (left) and  $S2$  (right).

Figure 6.16 illustrates the rotating and synchronous fluctuations resulting from decomposition of pressure fluctuations on sections  $S1$  and  $S2$ . They are reconstructed from the results of the Fourier series.

The synchronous and rotating components of vortex rope induced pressure fluctuations are well predicted by the incompressible numerical simulation. It confirms that, at a cavitation-free operating point, where the value of Mach number,  $M$ , is very small, around 0.005 in the present case, the hypothesis of incompressible flow remains valid.

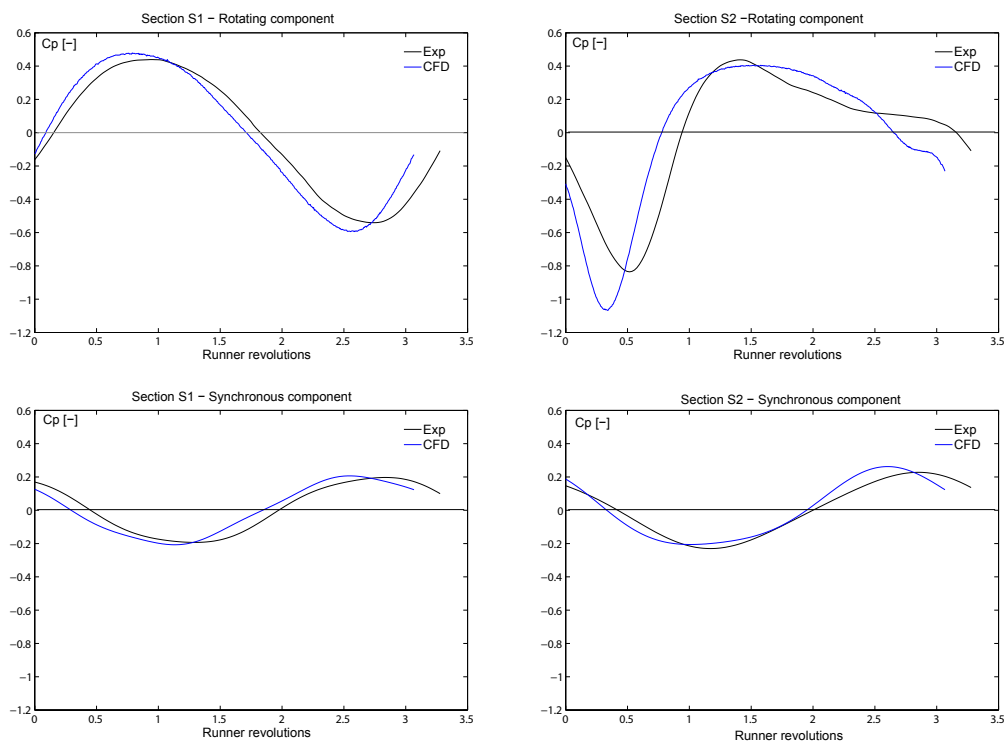


Figure 6.16: Numerical and experimental results: decomposition of the rotating and synchronous fluctuations at sections  $S1$  (left) and  $S2$  (right).



**Part IV**  
**CONCLUSIONS**



# Chapter 7

## Conclusions and Perspectives

### 7.1 Conclusions

#### Rotor-Stator Interaction

Numerical and experimental investigations of the rotor-stator interaction are performed in the generating mode of a reduced-scale model pump-turbine in the framework of the Hydrodyna project. Three operating points corresponding to part load, best efficiency and full load conditions are selected at a constant energy coefficient. Since a strong rotor-stator interaction occurs at full load operating point, detailed analyses are made in stationary and rotating components.

The numerical simulations of the unsteady incompressible flow in a flow passage domain, including the full pump-turbine water passage are carried out. The numerical configuration using the standard turbulence model  $k - \varepsilon$ , relevant medium mesh resolution and a time step corresponding to  $0.5^\circ$  gives a good consistency between numerical and experimental results.

The advection of pressure fluctuations due to RSI are analyzed at the periphery of the vaneless gap as well as along a distributor channel. The related analysis identified the diametrical modes, which rotate due to the pressure gradient field in the distributor channel. A 2D spectral analysis in time and space permits to identify the pressure amplitude corresponding to the diametrical mode. This result could be applied to analyze the response of impeller structure to hydraulic excitation.

Regarding the pressure fluctuations along a distributor, further analysis is made to explain how pressure amplitude due to rotor-stator interactions rise and damp. One observes that during each impeller blade passage two pressure peaks appear. The higher peak is caused by the blockage effect of rotating impeller blades, when placed in front of the guide vane channel. The origin of the lower peak is the high pressure zones of the neighboring channels, which extends to the channel in between.

The fluctuations of the pressure field due to RSI in the impeller at both pressure and suction sides of the impeller blade are investigated at three operating points from part load to full load conditions. The difference between the instantaneous pressures at both sides of the impeller blade determines the exerted oscillating force. The blade roots at the leading edge are the region with the most powerful stress concentrations. With respect to

the phase shift between the neighboring impeller channels, a fixed value, which related to the pitch angle between guide vane and impeller channels is obtained. The same tendency is also obtained at both sides of the leading edge of a rotating blade for three investigated operating points, which is confirmed by both numerical and experimental results.

The hydraulic force on the structure due to rotor-stator pressure fluctuation varies in function of operating conditions. Discharge, angular velocity and the gap distance between guide vanes and impeller are the determinant variables, which affect the unsteady pressure perturbation. An appropriate non-dimensional number,  $\zeta$ , based on the time of flow passage through the vaneless gap,  $t_n = \frac{r_{gap}}{C_m}$  over the period of impeller revolution,  $T_n = \frac{2\pi}{\omega}$  is defined to take into account all variables which influence RSI. Pressure fluctuations, resulting from measurements at 15 operating points from part load to full load with constant specific energy are investigated. Evaluation of pressure perturbation in function of  $\zeta$  number at the above-mentioned operating conditions is investigated.

### Part Load vortex Rope

The numerical simulation of part load vortex rope is investigated. The goal of the present study is to develop a computational methodology, which can provide a detailed description of this time dependent phenomenon. An analysis of pressure fluctuations due to precessing vortex rope is performed in the draft tube cone.

3D unsteady state incompressible numerical simulation is accomplished in a computational domain, which involves full runner and draft tube. The result of pressure fluctuations at the periphery of the cone are compared with measurements. Accordingly, using the SAS turbulence model with the relevant medium mesh and time step gives a good consistency between numerical and experimental results.

Pressure fluctuations in the presence of a vortex rope have a complex structure in the draft tube. This pressure perturbation consists of two synchronous and rotating oscillations. The origin of synchronous perturbation is the interaction between the non-homogenous pressure fields in the elbow of the draft tube with the rotating part due to precessing vortex rope. The decomposition of these pressure modes resulting from numerical simulations is investigated and compared with measurements.

The physical mechanisms of RSI and PVR are associated with both viscous flow perturbation and hydroacoustic effects. Comparing the measurements, which include both compressible and incompressible flow characteristics with the numerical results, based on the incompressible flow hypothesis permits to judge about the ability of unsteady phenomena prediction by CFD. With respect to very good agreement between measurements and the results of the incompressible flow simulation at all three operating points, one can conclude that with the exception of vibration condition or fluid-structure interaction, the incompressible flow hypothesis is a correct assumption.

## 7.2 Perspectives

Vibration plays an increasingly significant role on the development of new pump-turbines. The present study has provided the necessary data to model the response of structures due to rotor-stator pressure fluctuations. The result of 2D spectral analysis could be applied



on the structure to model vibrations due to diametrical modes. This kind of simulation is not as heavy as fluid-structure simulation and focuses on the source of vibrations.

At a given off-design operating zone some other phenomena such as flow separation on the impeller blades or cavitation influence the pressure fluctuations due to RSI. As a result, non-periodic pressure fluctuations with higher pressure amplitudes could be measured. To model and analyze these complex phenomena, numerical simulations of flow pattern in the off-design operating zone should be performed. It necessitates a higher accuracy of turbulence models.

In 3D URANS simulations hydroacoustic effects are neglected, which in the vibration cases become very important. In order to model more reliable phenomena, it is proposed to couple the hydroacoustic and Navier-stokes equations. This issue could be made by two-way coupling of CFD package with hydroacoustic modeling software.

In the present study mono-phase numerical simulation of precessing vortex rope in a draft tube is performed. To continue this work multi-phase simulation to model cavitation effects is proposed. The validated results of this kind of simulation could define the necessary parameters for the hydroacoustic modeling.



# Appendix



# Appendix A

## Signal Processing

### A.1 Pressure Fluctuations

Periodic time history of pressure,  $p$ , due to rotor-stator interaction or precessing vortex rope, might be divided to three components. Average pressure,  $\bar{p}$ , periodic fluctuating component,  $\tilde{p}$  and the perturbation component,  $p'$ , see Figure A.1.

$$p(t) = \bar{p}(t) + \tilde{p}(t) + p'(t) \quad (\text{A.1})$$

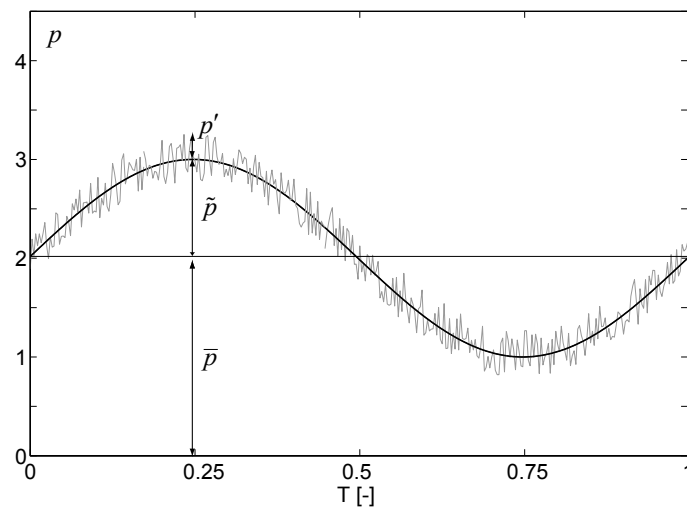


Figure A.1: Time history of pressure  $p$ , might be divided to three components. Average pressure,  $\bar{p}$ , Phase average signal,  $\tilde{p}$  and noise,  $p'$

### A.1.1 Average Pressure

The average pressure is defined as the average value of all samples in time, see Equation A.2. Where  $N$  is the total samples number,  $p(t_i)$  is pressure value at each sample. The values associated with time,  $t_i$ , is defined by accumulating time steps,  $\Delta t$  and  $t_0$  is the time reference.

$$\bar{p} = \frac{1}{N} \sum_{i=1}^N p(t_i) \quad t_i = t_0 + i\Delta t \quad (\text{A.2})$$

### A.1.2 Phase Average (Pressure Fluctuation)

Phase average is used in the case of periodic discrete signals. This method is based on the hypotheses that during each period of signal,  $T$ , the number of samples is constant,  $m$ . Thereby, phase average is the mean value of the  $j^{\text{th}}$  samples of all periods, where  $j$  is the sample number of a period. This issue is expressed by Equation A.3 where,  $x_i(t)$ , is signal sample in a period and  $\bar{x}_j(t)$  is the result of phase average for each sample.

$$\bar{x}_j(t) = \frac{1}{n} \sum_{i=0}^{n-1} p_i(t_j) \quad j = 0, 1, \dots, m - 1 \quad (\text{A.3})$$

The result of phase average gives the measurements pressure fluctuations. These results are used to compare with numerical pressure fluctuations.

## A.2 Spectral Analysis

### A.2.1 Fourier Series

Fourier series decomposition is applied over a periodic function into a sum of simple oscillating functions as sines and cosines. In the field of discrete signal processing Equation , is used to transform the data series,  $x(t)$ , into a frequency domain function of  $X(m)$ .

$$X(m) = \sum_{n=0}^{N-1} x(n) e^{-j2\pi mn/N} \quad (\text{A.4})$$

This equation could be written as a sum of sines and cosines fluctuations with the amplitude of  $a_k$  and  $b_k$ .

$$x(t) = \frac{a_0}{2} + \sum_{k=1}^{\infty} (a_k \cos 2\pi f_k t + b_k \sin 2\pi f_k t) \quad f_k = \frac{k}{T} \quad k = 1, 2, 3, \dots \quad (\text{A.5})$$

Inverse of Equation A.5 gives the amplitude values corresponding to each frequencies, Equation A.6 to Equation A.8 .

$$a_k = \frac{2}{T} \int_0^T x(t) \cos 2\pi f_k t dt \quad k = 0, 1, 2, \dots \quad (\text{A.6})$$

$$b_k = \frac{2}{T} \int_0^T x(t) \sin 2\pi f_k t dt \quad k = 1, 2, 3, \dots \quad (\text{A.7})$$

$$\frac{a_0}{2} = \frac{1}{T} \int_0^T x(t) dt \quad (\text{A.8})$$

### A.2.2 Fourier Transform

The goal of Fourier transform is to express a complex function as a simple linear combination. Fourier transform,  $X(f)$ , of a signal  $x(t)$  is a complex function of frequency  $f$  by the Equation A.10:

$$X(f) = \int_{-\infty}^{+\infty} x(t) e^{-j2\pi ft} dt \quad -\infty < f < +\infty \quad (\text{A.9})$$

$$X_T(f) = X(f, T) = \int_0^T x(t) e^{-j2\pi ft} dt \quad (\text{A.10})$$

with respect to periodicity assumption of continuous signal, fourier transform could be limited to one period,  $T$ .

$$X_T(f_k) = \Delta t \sum_0^{N-1} x_n e^{-j2\pi f_k n \Delta t} \quad (\text{A.11})$$

$X(f)$  is a complex signal that is expressed as Equation A.12:

$$X(f) = \text{Re}[X(f)] + j \text{Im}[X(f)] \quad (\text{A.12})$$

$$\text{Re}[X(f)] = \sum_{t=-\infty}^{+\infty} x(t) \cos 2\pi ft \quad (\text{A.13})$$

$$\text{Im}[X(f)] = - \sum_{t=-\infty}^{+\infty} x(t) \sin 2\pi ft \quad (\text{A.14})$$

Fourier transform could be expressed as Equation A.15, where  $|X(f)|$  is the amplitude of frequency  $f$  and the term  $\theta_{\text{arg}}$  is the corresponding phase angle.

$$X(f) = |X(f)| e^{-j\theta_{\text{arg}}} \quad (\text{A.15})$$

### A.2.3 2D Fourier Transform

If  $x(t, s)$  is a function of two discrete spatial variables such as time  $t$  and space,  $s$ , then the 2D analysis formula could be expressed as multiplication of two separate function in two dimensions, time  $t$  and space  $s$ .

$$X(f, g) = X(f) \cdot Y(g) = \int_{-\infty}^{+\infty} x(t)e^{-j2\pi ft} dt \cdot \int_{-\infty}^{+\infty} y(s)e^{-j2\pi gs} ds \quad (\text{A.16})$$

Thereby, 2D Fourier transform is written as a 1D analysis in  $t$  direction followed by a 1D analysis in the  $s$  direction.

$$X(f, g) = \int_{-\infty}^{+\infty} \left[ \int_{-\infty}^{+\infty} x(t, s)e^{-j2\pi ft} dt \right] e^{-j2\pi gs} ds \quad (\text{A.17})$$

$$X(f, g) = \int_{-\infty}^{+\infty} \int_{-\infty}^{+\infty} x(t, s)e^{-j2\pi(ft+gs)} dt ds \quad (\text{A.18})$$

Working with the Fourier transform usually involves the discrete Fourier transform (DFT). A discrete transform is a transform whose input and output values are discrete samples, making it convenient for computer manipulation. The DFT is usually defined for a discrete function that is nonzero only over the finite region. The two-dimensional M-by-N DFT and relationship is given by:

$$X(f, g) = \sum_{m=1}^M \sum_{n=1}^N x(t, s)e^{-j2\pi(\frac{mt}{M} + \frac{ns}{N})} \quad (\text{A.19})$$

$$x(t, s) = \frac{1}{MN} \sum_{t=1}^M \sum_{s=1}^N X(f, g)e^{j2\pi(\frac{mt}{M} + \frac{ns}{N})} \quad (\text{A.20})$$



# Bibliography

- [1] ADAMCZYK, J. Model equation for simulating flows in multistage turbomachinery. *ASME paper* (1985).
- [2] ADAMCZYK, J., CELESTINA, M., BEACH, T., AND BARNETT, M. Simulation of three-dimensional viscous flow within a multistage turbine. *ASME J. Turbomach.* 112 (July 1990), 370–376.
- [3] ADAMCZYK, J., MULAC, R., AND CELESTINA, M. A model for closing the inviscid form of the average-passage equation system. *ASME J. Turbomach.* 108 (Oct. 1986), 180–186.
- [4] ANGELICO, G., MUCIACCIA, F., AND ROSSI, G. Part load behaviour of a turbine : a study on a complete model of hydraulic power plant. In *Proceedings of the IAHR Symposium* (1986).
- [5] ARNDT, N., ACOSTA, A., BRENNEN, C., AND CAUGHEY, T. Experimental investigation of rotor-stator interaction in a centrifugal pump with several vaned diffuser. *ASME J. Turomach.* 112 (Jan. 1990), 98–108.
- [6] ARPE, J. *Analyse du champ de pression pariétale d'un diffuseur coudé de turbine Francis*. PhD thesis, EPFL, Lausanne, 2003.
- [7] ARPE, J., AND AVELLAN, F. Pressure wall measurements in the whole draft tube : Steady and unsteady analysis. In *21st IAHR Symposium* (2002), pp. 593–602.
- [8] AVELLAN, F. Flow investigation in a francis draft tube: The flindt project. In *20th IAHR Symposium* (2000).
- [9] BARTLE, A. The hydroad: Global prespective. In *All-ENERGY'07* (2007).
- [10] BENJAMIN, T. Theory of vortex breakdown phenomenon. *J. Fluid Mech.* 14 (1962), 593–629.
- [11] BERT, P., COMBES, J., AND KUENY, J. Unsteady flow calculation in a centrifugal pump using a finite element method. In *18th IAHR Symp.* (1996), pp. 737–747.
- [12] BHAN, S., CODRINGTON, J., AND MIELKE, H. Reduction of francis turbine draft tube surges. In *American Society of Mechanical Engineers, Fluids Engineering Division (Publication) FED* (1988), vol. 68, pp. 95–102.
- [13] BOLLETER, U. Blade passage tones of centrifugal pumps. *Vibrations* 4 (1988), 8–13.

- [14] BRAUN, O., AVELLAN, F., AND DUPONT, P. Unsteady numerical simulations of the flow related to the unstable energy-discharge characteristic of a medium specific speed double suction pump. In *FEDSM2007* (2007).
- [15] BRENNEN, C., AND DUTTWEILER, M. Surge instability on a cavitating propeller. *J. Fluid Mech.* 458 (2002).
- [16] BROWN, G., AND LOPEZ, J. Axisymmetric vortex breakdown. part 2. physical mechanisms. *J. Fluid Mech* 221 (1990), 553–576.
- [17] CADER, T., MASBERNAT, O., AND ROCO, M. C. Ldv measurements in a centrifugal slurry pump: Water and dilute slurry flows. *ASME J. Fluid Eng.* 114 (1992), 606.
- [18] CASSIDY, J., AND FALVEY, H. Observations of unsteady flow arising after vortex breakdown. *J. Fluid Mech.* 41 (1970), 727–736.
- [19] CFX-ANSYS CANADA LTD. *CFX-5.7: Solver Theory*. Canada, 2004.
- [20] CHU, S., DONG, R., AND KATZ, J. Relationship between unsteady flow, pressure fluctuations, and noise in a centrifugal pump part a: Use of pdv data to compute the pressure field. *ASME J. Fluids Eng.* 117 (March 1995), 24–29.
- [21] CIOCAN, G., AVELLAN, F., AND KUENY, J.-L. Optical measurement techniques for experimental analysis of hydraulic turbines rotor-stator interaction. *American Society of Mechanical Engineers, Fluids Engineering Division (Publication) FED* 253 (2000), 271–277.
- [22] CIOCAN, G., ILIESCU, M., VU, T., NENNEMANN, B., AND AVELLAN, F. Experimental study and numerical simulation of the flindt draft tube rotating vortex. *Journal of Fluids Engineering, Transactions of the ASME* 129 (2007), 146–158.
- [23] COUSTON, M., AND PHILIBERT, R. Francis turbines at part load; matrix simulating the gaseous rope. In *IAHR Symposium* (1998).
- [24] COUSTON, M., AND PHILIBERT, R. Partial load modelling of gaseous francis turbine rope. In *IAHR Symposium* (1998).
- [25] DOERFLER, P. On the role of phase resonance in vibrations caused by blade passage in radial hydraulic turbomachines. In *12th IAHR Symposium* (1984).
- [26] DONG, R., CHU, S., AND KATZ, J. Effect of modification to tongue and impeller geometry on unsteady flow, pressure fluctuations, and noise in a centrifugal pump. *ASME J. Turbomach.* 119 (1977), 506–515.
- [27] DORFLER, P. Francis turbine draft tube surges - a systems oriented approach. Braunschweig, Fed. Rep. Germany: Oct. 14–16, 1981, Dusseldorf, Fed. Rep. Germany, VDI-Verlag GmbH,.
- [28] DORFLER, P. System dynamics of the francis turbine half load surge. In *IAHR Symposium* (1982).

- [29] DORFLER, P. Enhancing the safe operation of surge tanks. *International Journal on Hydropower and Dams* 7 (2000), 43–46.
- [30] DRING, R. P., JOSLYN, H., HARDIN, L., AND WAGNER, J. H. Turbine rotor-stator interactions. *J. Eng. Power* 104 (Oct. 1982), 729–742.
- [31] ERDOS, J. I., ALZNER, E., AND MCNALLY, W. Numerical solution of periodic transonic flow through a fan stage. *AIAA Journal* 15 (1977), 1159–1568.
- [32] FARHAT, M., NATAL, S., AVELLAN, F., PAQUET, F., LOWYS, P., AND COUSTON, M. Onboard measurements of pressure and strain fluctuations in a model of low head francis turbine. part 1: Instrumentation. In *21st IAHR Symposium* (2002), pp. 865–872.
- [33] FISHER, J., SEIDEL, U., GROSSE, G., GFELLER, W., AND KLINGER, R. A case study in resonant hydroelastic vibration: The causes of runner cracks and the solutions implemented for the xiaolangdi hydroelectric project. In *XXIst IAHR Symposium* (2002).
- [34] FOX, R. *McDonald. Introduction to Fluid Mechanics*, vol. 651. John Wiley & Sons, 1995.
- [35] FRANC, J., AVELLAN, F., BELAHADJI, B., BILLARD, J., BRIANCON-MARJOLLET, L., FRECHOU, D., FRUMAN, D., KARIMI, A., KUENY, J., AND MICHEL, J. *La cavitation : Mecanismes physiques et aspects industriels*. 1995.
- [36] FRANKE, G., POWELL, C., SEIDEL, U., KOUTNIK, J., AND FISCHER, R. K. On pressure mode shapes arising from rotor/stator interactions. *Sound and Vibration* (2005), 12–18.
- [37] GIESING, J. Nonlinear two-dimensional unsteady potential flow with lift. *J. Aircraft* 5 (1968), 135–143.
- [38] GILES, M. B. Stator/rotor interaction in a transonic turbine. *AIAA Journal* 6 (1990), 621–627.
- [39] GONZALEZ, J., FERNANDEZ, J., BLANCO, E., AND SANTOLARIO, C. Numerical simulation of the dynamic effects due to impeller-volute interaction in a centrifugal pump. *ASME J. Fluids Eng.* 110 (June 2002), 348–355.
- [40] GUO, S., AND OKAMOTO, H. An experimental study on the fluid forces induced by rotor-stator interaction in a centrifugal pump. *Inter. J. Rotating Machinery* 9 (1992), 135–144.
- [41] GUO, Y., KATO, C., AND MIYAGAWA, K. Large-eddy simulation of non-cavitating and cavitating flows in an elbow draft tube. In *23th IAHR Symposium* (2006).
- [42] HABAN, V., KOUTNIK, J., AND POCHYLÝ, F. 1-d mathematical model of high-frequency pressure oscillations induced by rsi inducing an influence of fluid second viscosity. In *21st IAHR Symposium* (2002).

- [43] HARVEY, J. Some observations of the vortex breakdown phenomenon. *J. Fluid Mech.* 14 (1962), 585–592.
- [44] HE, L., AND DENTON, J. D. Three-dimensional time-marching inviscid and viscous solutions for unsteady flows around vibrating blades. *Journal of Turbomachinery* 116 (1994), 469–476.
- [45] HE, L., AND NING, W. Efficient approach for analysis of unsteady viscous flows in turbomachines. *AIAA J* 36, 11 (1998), 2005–2012.
- [46] HENRY, P. *Turbomachines hydrauliques*. Presses internationale Polytechnique Inc, 1992.
- [47] IEC-60193. Model acceptance tests to determinate the hydraulic performance of hydraulic turbines, storage pumps and pump-turbines. In *International Standard I.E.C.* (1993).
- [48] IINO, T., AND KASAI, K. An analysis of unsteady flow induced by interaction between a centrifugal impeller and a vaned diffuser. *Trans. Jpn. Soc. Mech. Eng.* 51, 471 (1985), 154–159.
- [49] ILIESCU, M., CIOCAN, G., AND AVELLAN, F. 2 phase piv measurements at the runner outlet in a francis turbine. *Proceedings, FEDSM' 03, 4th ASME/JSME Joint Fluids Engineering Conference* (2003).
- [50] INOUE, M., AND CUMPSTY, N. Experimental study of centrifugal impeller discharge flow in vaneless and vaned diffusers. *Journal of Engineering for Gas Turbines and Power* 106 (1984), 455–467.
- [51] INTERNATIONAL HYDROPOWER ASS., U., INTERNATIONAL COMMISSION ON LARGE DAMES, F., IMPLEMENTING AGREEMENT ON HYDROPOWER, F., AND CANADIAN HYDROPOWER ASS., C. Hydropower and the world's energy future. Tech. rep., IEAHYDRO, 2000.
- [52] JACOB, T., PRENAT, J. E., AND ANGELICO, G. Unstable part-load Operation of a Model Francis Turbine : Evaluation of Disturbance Magnitude. In *Proceedings of the 17th IAHR Symposium, Beijing, Chine* (1994), vol. 2, pp. 933–942.
- [53] JACOB, T., PRENAT, J. E., AND BUFFET, G. Improving the Stability of Operation of a 90 MW Francis Turbine. In *Proceedings of the international Conference on Hydropower into the next Century, Barcelona, Spain* (1995).
- [54] JAEGER, C. The theory of resonance in hydropower systems. discussion of incidents and accidents. occuring in pressure systems. *Trans. ASME, J. of Basic Engineering* 4 (1963), 631–640.
- [55] KOUTNIK, J., AND PULPITEL, L. Modeling of the francis turbine full-load surge. *Modeling, Testing and Monitoring for Hydro Power Plants* (1996).
- [56] KRAIN, H. Study on centrifugal impeller and diffuser flow. *Journal of engineering for power* 103, 4 (1981), 688–697.

- [57] KUBOTA, Y., SUZUKI, T., AND TOMITA, H. Vibration of rotating bladed disc excited by stationary distributor forces. *Bulletin of the JSME* 26 (1983), 1952–1957.
- [58] KUOUTNIK, J., AND POCHYLÝ, F. Parametric excited pressure oscillations in hydraulic systems. In *21th IAHR Symposium* (2001).
- [59] LAKSHMINARYANA, B., AND DAVINO, R. Mean velocity and decay characteristics of the guidevane and stator blade wake of an axial flow compressor. *J. Eng. Power* (Oct. 1980), 50–60.
- [60] LONGATTE, F., AND KUENY, J.-L. Analysis of rotor-stator-circuit interactions in a centrifugal pump. *FEDSM'99, San Francisco, California, USA* (1999).
- [61] LOPEZ, J. axisymmetric vortex breakdown part 1. confined swirling flow. *J. Fluid Mech.* 221 (1990), 533–552.
- [62] LOWYS, P., DOYON, J., COUSTON, M., AND VUILLEROD, G. Dynamic behaviour of low head francis turbines. In *10th IAHR Work Group*. (2001).
- [63] MAURI, S. Numerical simulation and flow analysis of an elbow diffuser. *EPFL thesis n 2527, Lausanne, 2002*.
- [64] MAURI, S., KUENY, J., AND AVELLAN, F. Numerical prediction of the flow in a turbine draft tube influence of the boundary conditions. *American Society of Mechanical Engineers, Fluids Engineering Division (Publication) FED 251* (2000), 701–704.
- [65] MAURI, S., KUENY, J., AND AVELLAN, F. Werle-legendre separation in a hydraulic machine draft tube. *Journal of Fluids Engineering, Transactions of the ASME* 126, 6 (2004), 976–980.
- [66] MAURI, S., KUENY, J.-L., AND AVELLAN, F. Werle-legendre separation in a hydraulic machine draft tube. In *American Society of Mechanical Engineers, Fluids Engineering Division (Publication) FED* (2002), vol. 257, pp. 885–892.
- [67] MAZZOUJI, F., SEGOUFIN, C., LOWYS, P. Y., AND DENIAU, J. L. Investigation of unsteadiness in hydraulic turbines. In *23rd IAHR Symposium* (2006).
- [68] MENTER, F. Two-equation eddy-viscosity turbulence models for engineering applications. *AIAA-Journal* 32, 8 (1994).
- [69] MENTER, F., AND KUNTZ, M. Re-visiting the turbulent scale equation. In *IUTAM Symposium* (2004).
- [70] MENTER, F., AND KUNTZ, M. Development and application of a zonal des turbulence model for cfx-5. Tech. rep., ANSYS-CFX Canada Ltd., CFX-Validation Report, CFX-VAL17/0503.
- [71] MENTER, F. R., AND EGOROV, Y. Scale-adaptative simulation model using two equations models. In *AIAA Symposium* (Reno, 2005).

- [72] MÜNCH, C. *Simulation des Grandes Echelles d'écoulements turbulents compressibles dans des conduits*. PhD thesis, INPG, 2005.
- [73] NENNEMANN, B., VU, T., AND FARHAT, M. Cfd prediction of unsteady wicket gate-runner interaction in francis turbines: Anew standard hydraulic design procedure. In *Waterpower XIV* (2005).
- [74] NENNEMANN, B., VU, T., AND FARHAT, M. Investigation of unsteadiness in hydraulic turbines. In *23rd IAHR Symposium* (2006).
- [75] NICOLET, C. *Hydroacoustic modelling and numerical simulation of unsteady operation of hydroelectric systems*. PhD thesis, Lausanne, 2007.
- [76] NICOLET, C., RUCHONNET, N., AND AVELLAN, F. One-dimensional modeling of rotor stator interaction in francis pump-turbine. In *ISROMAC-11* (2006).
- [77] NISHI, M., MATSUNAGA, S., KUBOTA, T., AND SENOO, Y. Flow regimes in an elbow-type draft tube. In *11th IAHR Symposium* (1982), vol. 2.
- [78] NISHI, M., MATSUNAGA, S., OKAMOTO, M., EGUCHI, K., KUBOTA, T., AND SENOO, Y. Influence of draft tube shape on the characteristics of pressure surge and flow regime. *Nippon Kikai Gakkai Ronbunshu, B Hen/Transactions of the Japan Society of Mechanical Engineers, Part B 52* (1986), 3237–3243.
- [79] NISHI, M., SHIGENORI, M., KUBOTA, T., AND SENOO, Y. Surging characteristics of conical and elbow-type draft tubes. In *12th Symp. of IAHR* (1984), pp. 272–283.
- [80] PEDERSON, N., AND JACOBSEN, C. Flow in a centrifugal pump impeller at design and off design conditions-part 1: particle image velocimetry (piv) and laser doppler velocimetry (ldv) measurements. *ASME J. Fluid Eng. 125* (Jan. 2003), 61–83.
- [81] PEREIRA, F., FARHAT, M., AND AVELLAN, F. Dynamic calibration of transient sensors by spark generated cavity. In *Proceedings of IUTAM Symposium on Bubble Dynamics and Interface Phenomena* (1993), p. Sept.
- [82] PERRIG, A. *Hydrodynamics of the free surface flow in Pelton turbine buckets*. PhD thesis, Lausanne, 2007.
- [83] PERRIG, A., AVELLAN, F., KUENY, J. L., FARHAT, M., AND PARKINSON, E. Flow in a pelton turbine bucket: numerical and experimental investigations. *ASME J. Fluids Eng. 128* (March 2006), 350–358.
- [84] RAI, M. M. Three-dimensional navier-stokes simulations of turbine rotor-stator interaction. part i - methodology. *AiAA Journal 5* (1989), 305–319.
- [85] RAJ, R., AND LAKSHMINARAYANA, B. Characteristics of the wake behind a cascade of airfoils. *J. Fluid Mechanics 61* (1973), 707–730.
- [86] RHEINGANS, W. Power swing in hydro power plants. *Trans. ASME 62* (1940).
- [87] RUPRECHT, A. Numerical prediction of vortex instabilities in turbomachinery. vol. 93, pp. 211–224.

- [88] RUPRECHT, A., HELMRICH, T., ASCHENBRENNER, T., AND SCHERER, T. Simulation of pressure surge in a hydro power plant caused by an elbow draft tube. In *10th International Meeting of the IAHR Working Group on the Behaviour of Hydraulic Machinery under Steady Oscillatory Conditions* (2001).
- [89] SICK, DOERFLER, P., SALLABERGER, M., LOHMBERG, A., AND CASEY, M. Cfd simulation of the draft tube vortex. In *Proceedings, XXI IAHR Symposium on Hydraulic Machinery and Systems* (2002).
- [90] SICK, M., MICHLER, W., DOERFLER, P., SALLABERGER, M., AND LOHMBERG, A. Investigation of the draft tube vortex in a pump-turbine. In *XXII IAHR Symposium* (2004).
- [91] SINHA, M., AND KATZ, J. Quantitative visualization of the flow in a centrifugal pump with diffuser vanes i: on flow structures and turbulence. *ASME J. Fluids Eng.* 122 (March 2000), 97–107.
- [92] SQUIRE, H. Analysis of the vortex breakdown phenomena part i. *Imperial College Aeronautics Department Report 102 102* (1960).
- [93] STEIN, P., SICK, M., DOERFLER, P., AND BRAUNE, A. Numerical simulation of the cavitating draft tube vortex in a francis turbine. In *23th IAHR Symposium* (2006).
- [94] SUSAN-RESIGA, R., CIOCAN, G., ANTON, I., AND AVELLAN, F. Analysis of the swirling flow downstream a francis turbine runner. *Journal of Fluids Engineering, Transactions of the ASME* 128, 1 (2006), 177–189.
- [95] SYRED, N. A review of oscillation mechanisms and the role of the precessing vortex core (pvc) in swirl combustion systems. *Progress in Energy and Combustion Science* 32, 2 (2006), 93–161.
- [96] TANAKA, H. Vibration behaviour and dynamic stress of runner of very high head reversible pump-turbine. In *15th IAHR Symp.* (1990).
- [97] VU, T., AND , NENNEMANN, B. Modern trend of cfd application for hydraulic design procedure. In *23rd IAHR Symposium* (2006).
- [98] WANG, Z., AND ZHOU, L. Simulations and measurements of pressure oscillations caused by vortex ropes. *Journal of Fluids Engineering, Transactions of the ASME* 128, 4 (2006), 649–655.
- [99] WILCOX, D. C. *Turbulence Model for CFD*. DCW Industries, 1988.
- [100] Y. TSUJIMOTO, Y., KAMIJO, K., AND YOSHIDA, Y. Theoretical analysis of rotating cavitation in inducers. *J. Fluid Eng.* 115 (1993), 135–141.
- [101] ZOBEIRI, A., KUENY, J.-L., FARHAT, M., AND AVELLAN, F. Pump-turbine rotor-stator interactions in generating mode: pressure fluctuation in distributor channel. In *23rd IAHR Symposium* (2006).

# Alireza ZOBEIRI

Date of Birth: 19. Feb. 1975, Iran  
E-mail: azobeiri@yahoo.com  
Mobile: +41 78 847 7336

## EDUCATIONS

---

- **Doctoral Science, Hydraulic Machines** 2001-2005  
EPFL , Laboratory for Hydraulic Machines (LMH), Lausanne, Switzerland
- **Master, Energy Conversion** 1999-2000  
Tehran Polytechnic, Tehran, Iran
- **Bachelor, Mechanical Engineering** 1993-1998  
University of Tehran, Tehran, Iran

## EXPERIENCES

---

- **EPFL, Laboratory for Hydraulic Machines** 2001-2008  
Researcher and Project liaison of HYDRODYNA and FLINDT Projects  
Industrial Partners, ALSTOM, EDF, GE, ANDRITZ, VOITH-SIMENS
- **FARAB, Main contractor of Hydro power plant-Iran** 1999-2001  
Hydraulic engineer of MASJED SOLEIMAN Hydropower plant project  
Industrial Partners, VOITH-SIMENS, HARBIN, LAMAYER

## COMPUTER SKILLS

---

- Operating system: Windows, MS-DOS, Unix (IBM-AIX).
- Program: C++, Fortran, Matlab
- CFD Tools: CFX, NUMECA, ANSYS-CFX, ICEM,
- CAD Tools: CATIA

## LANGUAGES

---

- Persian Mother Tongue
- English Well Known, B2
- French Well Known, B2